AN ABSTRACT OF THE THESIS OF

Jaeseok Heo for the degree of Doctor of Philosophy in Chemistry presented on April 9, 2014.

Title: New Multi-Functional Chalcogenides for Photovoltaic and Thermoelectric Materials.

Abstract approved: _____

Douglas A. Keszler

The subject of this PhD thesis is part of a research domain of great present interest in new semiconductor materials for photovoltaic and thermoelectric applications. This domain contains the elaboration and the study of both Cu-based chalcogenides bulk and thin-film samples, driven by materials design principles.

One of the most research semiconductor materials is the synthetic mineral tetrahedrite, typified by $Cu_{12}Sb_4S_{13}$. Optical, electrical, and thermal properties have been tuned via chemical substitutions, allowing optimization of performance toward the realizations of high-efficiency devices. Chapter 2 and 3 detail exploration of several tetrahedrite-derivatives for PV and TE applications, respectively. This work demonstrates that this exceptional multi-functionality is related to the unique structural building blocks of these materials. In the context of similar structural features, Cu_3-V-VI_4 (V = P, As, Sb; VI = S, Se) has been discovered as new absorbers in Chapter 4. Chapter 5 attempts to find the missing Co_2GeS_4 compound through $(Fe,Co)_2GeS_4$ and $(Co,Zn)_2GeS_4$ solid solutions by a systematic investigation between theoretical prediction and experimental results. More generally, this fundamental research creates a practical framework for future design principles based search and discovery of effective materials.

©Copyright by Jaeseok Heo

April 9, 2014

All Rights Reserved

New Multi-Functional Chalcogenides for Photovoltaic and Thermoelectric Materials

by

Jaeseok Heo

A THESIS

submitted to

Oregon State University

in partial fulfillment of

the requirements for the

degree of

Doctor of Philosophy

Presented on April 9, 2014

Commencement June, 2014

Doctor of Philosophy dissertation of Jaeseok Heo presented on April 9, 2014.

APPROVED:

Major Professor, representing Chemistry

Chair of the Department of Chemistry

Dean of the Graduate School

I understand that my thesis will become part of the permanent collection of Oregon State University libraries. My signature below authorizes release of my thesis to any reader upon request.

Jaeseok Heo, Author

ACKNOWLEDGEMENTS

It would not have been possible to write this doctoral thesis without the help and support of many people around me, to only some of whom it is possible to give particular mention here. First of all, I wish to express my gratitude to my supervisor, Prof. Douglas A. Keszler for his help, support and patience during my graduate level study and research, not to mention his advice and unsurpassed knowledge of solid-state chemistry. I also appreciate him giving me autonomy and fostering a creative environment in my research. He is now a wonderful role model for my future as a researcher. Deepest gratitude is also due to the members of the supervisory committee; Janet Tate, John F. Wager, Mas A. Subramanian, and Brady J. Gibbons. This study would not have been successful without their knowledge and assistance. Dr. Tate has taught me a lot about solid-state physics, and she encouraged me to pursue new ideas in many physical measurements. I would like to thank Dr. Wager for filling a void in device physics with many useful things in both fundamental and practical points of view. I appreciate Dr. Subramanian's instruction in solid-crystal structures and use of instruments in his laboratory. Guenter Schneider, Ethan Minot, Michael Lerner, and Paul Cheong have also made valuable contributions to my graduate work, and I especially want to thank them for their patience with all of my questions.

I have enjoyed studying and working with many other past and current members of the Keszler, Wager, Subramanian, and Tate research groups. Collaborations with many people of different departments have really helped to broaden my horizons. Amongst my collaborators, I will never forget the efforts made by Robert Kokenyesi in stimulating my academic achievements and in welcoming me socially. As a friend,

I wish him success on his starting company, Beets. Ram Ravichandran and I worked together applying solid-state chemistry to new materials development for solar absorbers, and I am grateful to him for many useful and interesting conversations. Every time I worked with Geneva Laurita-Plankis and Sean Muir on new thermoelectric materials, I benefited greatly from their tireless efforts to ensure that we get the best data possible. I appreciate Christophoer Reidy, Brian Pelatt and Greg Angelos for their contributions on the challenges of thin-film deposition with my samples. I would like to thank Vorranutch Jieratum for assistance with her experience on the execution of solid-state synthesis. Lev Zakharov helped and taught me a lot about X-ray analysis, and I want to thank for his assistance. Christopher Knutson was a good English teacher, even though his language was heavily laden with expletives. I would also like to convey thanks to other members including of Alan Telecky, Emmeline Altschul, Hidekel A. Moreno Luna, Wei Wang, Kristopher Olsen, Vasily Goulioukk, Jennie Amador, Shawn Decker, Yu Huang, Ryan Mansergh, Deok Hie Park, Ben Waters, John McGlone, Jason Francis, River Wiedle, Josh Flynn. They have made valuable contributions to my graduate work, both in the classroom and in the lab.

In addition to my work within Oregon State University (OSU), I have also appreciated opportunities to join the Center for Inverse Design through Energy Frontier Research Centers (EFRCs). I would like to acknowledge the academic and technical support of this center particularly that provided the necessary financial support for this research. All members including of its faculties, postdoctoral researchers, graduate students, and staffs have been indispensable. I particularly want to thank Xiuwen Zhang, a postdoctoral researcher in National Renewable Energy Laboratory (NREL),

for his contributions on my research, and he has taught me a lot about theoretical calculations on solid-state physics.

I am most grateful to Inpria staffs including of Andrew Grenville, Stephen T. Meyers, Jeremy Anderson, Ben Clark, and Kai Jiang. I would like to thank Andrew for providing me a chance to work with Doug, and it was particularly kind of him to help me settle down here. I appreciate the other members for their kindness, friendship, and support on my Corvallis' life. I would also like to thank my colleagues and friends in the previous college, Hanyang University, and in the previous work place, LG Display.

And finally, I could not have completed my graduate work without the help of my family. I would like to thank Sunju, my wife, for her personal support and great patience at all times. I want to thank my kids, Irang and Iji, for their patience with all of my situations. My parents have given me their unequivocal support throughout, as always, for which my mere expression of thanks likewise does not suffice. I will also take this opportunity of thanking Jeong-woo and Woo-jae, the best friends for everything.

TABLE OF CONTENTS

Page

TABLE OF CONTENTS (Continued)

Page

LIST OF FIGURES

Figures Page

LIST OF FIGURES (Continued)

Figures Page

LIST OF FIGURES (Continued)

Figures Page

LIST OF FIGURES (Continued)

Figures Page

Chapter 1

Introduction

In the context of renewable energy, photovoltaics (PV) and thermoelectrics (TE) are promising technologies for generating electricity from natural sunlight and waste heat, respectively. So far, however, no photovoltaic and thermoelectric devices have attained the necessary efficiency and performance levels to compete with conventional energy sources. For photovoltaic devices, band-gap optimization, as outlined by Schockley and Queisser (S-Q)[1], have been the main design principle for identifying and selecting new absorber materials that offer potential for efficiency improvements in PV. With this simple metric, PV industry and science communities have been largely focused on the usual suspects of Si, CdTe, $Cu(In,Ga)Se_2$ (CIGS), and Cu_2ZnSnS_4 (CZTS) as the path to a viable solar market. It is doubtful, however, that these materials can enable widespread implementation of solar energy at costs competitive with nonrenewable source, due to their poor optical absorption. Our group has, recently, enhanced the S-Q model by introducing a new metric, Spectroscopic Limited Maximum Efficiency (SLME), which incorporates the full absorption spectrum of the absorber. Applying this new metric, we have formulated new Cu-M-VI system (M = group III-V; IV = O, S, Se) as new potential high-performance solar absorbers.[2] These materials contain structural building blocks with a M atom isolated or including a M atom with a ns^2np^0 electron configuration. These structural features lead to enhance optical absorption with a rapid onset near the band-gap. Interestingly, these structural features also encompass materials design approaches for realizing low thermal conductivities, which play a primary role maximizing thermoelectric efficiency.[3] Here, this dissertation shows that synthetic forms of the mineral tetrahedrite, which contain the desired structural building blocks, exhibit both exceptionally high absorption and very low thermal conductivity. In addition, optical, electrical, and thermal properties can be tuned via selective chemical substitutions, allowing optimization of properties toward improved performance.

1.1 Current status of renewable energy

Our society currently relies heavily on fossil fuels, e.g., coal, oil, and natural gas, for its energy. Conventional electricity generation, based on the combustion of fossil fuels, is nonrenewable. The depletion of these natural sources and the effects on natural ecosystems are a particular concern. In contrast, renewable energy relies on natural processes that are constantly replenished, lowering environmental impacts. In this respect, producing sustainable and clean energy is a central issue of our times. Since its inception, worldwide renewable energy capacity has continued to grow rapidly at rates of 10 – 60 % annually, for many technologies. In 2011, renewables provided 19 % of global electricity generation.[4] It is projected that renewable energy's share will rise to 28 % by 2020 and 57 % by 2050 with renewables dominating electricity power generation.[4]

Among all renewable energy technologies, PV has been growing the fastest at a 60 % annual average rate.[4] Especially, thin-film solar cells (TFSCs) for large-scale energy generation drive a growing share of global renewable energy production, with rapid increases in PV manufacturing capacity and reduction in balance-of-system costs. These costs are driven in large part by the need to maximize light-to-electricity conversion efficiency; however, current advances are still limited to 18 % for CdTe[5] and 20.3 % for CIGS[6] solar cells in laboratory scale devices. Thus, crystalline silicon (c-Si) still accounts for 85 % of the market.[7] To expand the position of TFSCs, further dramatic cost-reduction is required, which can only be achieved through device conversion efficiency and the use of readily available materials. In this context, new earth-abundant and non-toxic solar cell materials remains at the very heart of further technological progress towards TFSCs to be a larger contributor of the overall net electricity generation.

The scavenging of waste heat with thermoelectric (TE) generator is another way to improve the sustainability of electricity generation. Since typical engines operate at 30 – 40 % efficiency, a large amount of energy is lost to the environment via automotive and industrial exhaust. TE devices could potentially convert this waste heat to useful electricity with no moving parts. Among applications, the most promising TE application is to recover the vehicle waste heat for improving fuel economy. Honda and BMW, for example, have improved overall engine efficiency by 10 % using TE modules.[8] Like PV devices, the usefulness of TE materials is limited solely by their conversion efficiency, which is often stated as the dimensionless figure of merit ZT.[9] Unfortunately, the efficiency of commercialized TE materials is currently only about 1/6 of the maximum Carnot efficiency. There is, however, no theoretical upper limit to ZT and its improvement will boost applications of TE materials.[8] In this context, a number of design strategies have been employed to identify the next generation of TE materials.

1.2 Solar cells: Operation principles and new materials developments

1.2.1 Basic principles

PV solar cells convert electromagnetic energy derived from the temperature difference between the surface of the sun (T = 6000 K) and the earth (T = 300 K) into usable electrical energy in the form of current and voltage. As a PV device is basically a semiconductor diode, the PV energy conversion takes place through the two basic steps of photogeneration of charged carriers and charge extraction.

Photogeneration. The semiconductor material (absorber layer) absorbs the incoming photons, which causes a transition from a ground state to an excited state. In this step, both the band gap, E_G, and the absorption coefficient of the semiconductor are defining how many charge carriers

are generated from solar photons. Ideally, the inter-band transition will not be possible unless $h\nu \geq E_G$. Therefore, all photons with energy $h\nu \geq E_G$ will contribute to photogenerated electron-hole pairs, which produce the short-circuit current density (J_{SC}) of a solar cell. However, reducing E_G minimizes the available energy per absorbed photon, the open-circuit voltage (V_{OC}), since the generated electron-hole pairs will thermalize to the band edges - the valence band maximum (VBM) and the conduction band minimum (CBM). Thus, the V_{OC} value is related to E_G regardless of the initial photon energy, $h\nu$. Under this simple consideration, Shockley-Queisser (S-Q) limit describes an optimum E_G (1.3 ~ 1.4 eV) for which a maximum energy conversion (η) takes place, corresponding to the spectral photon flux of sunlight,[1]

$$\eta = \frac{P_{max}}{P_{in}} = \frac{FFV_{OC}J_{SC}}{\int_{E_G}^{\infty} E\emptyset_{sun}(E)dE} \qquad (1.1)$$

where, P_{max} is the maximum output power, P_{in} is the incident power, FF, called as the fill factor, is a measure of the squareness of the J-V characteristic at the maximum power point, and $\emptyset_{sun}$ is the incoming photon flux of the sun.

Charge extraction. In this transport step, the generated charge carriers, electrons and holes through the absorber layer to opposite contacts and produce a net photocurrent. With nothing to impede their motion, electrons and holes in semiconductors are subject to two classical transport processes, drift and diffusion, depending on the diode structure of the solar cell and the physical properties of the absorber material. Drift is a charged particle's response to the internal electric field created by the built-in asymmetry of a PV device. Diffusion is the result of thermal motion like the Brownian motion of gas molecules. Charged particles diffuse from regions of high concentration to regions of low concentration because of the driving force to even charge distribu-

tion within a semiconductor layer. Thus, total hole and electron currents are the sum of their drift and diffusion components, *cf.* Equation 1.2.

$$\vec{J} = \vec{J}_{drift} + \vec{J}_{diffusion} = -qn\mu_n\nabla\phi - qp\mu_p\nabla\phi + qD_n\nabla n - qD_p\nabla p \qquad (1.2)$$

where, μ_n and μ_p are the carrier mobilities, ϕ are the electronic potential, and D_n and D_p are the diffusion coefficients for carriers.

1.2.2 From the ideal to real PV devices

Assessment of efficiency limits of a solar absorber material are based on simple thermodynamic considerations, outlined by Shockley and Queisser, that rely on idealized assumptions. The first assumption is the probability of the light absorption generation an electron-hole pairs set to unity for $h\nu \geq E_G$ and zero for $h\nu < E_G$. That is, the absorption coefficient (α) is infinite at the band edge like a step function. However, the absorption of real semiconductor materials is continuously increasing from nearly zero below the band edge to over 10^5 cm^{-1}. The absorption coefficient can be described by two primary principles: the nature of band gap and Fermi's golden rule.[10] The band gap of semiconductors is always one of two types: a direct or an indirect band gap. An optical transition in direct semiconductors occurs at the same wave vector of electrons, while an absorption process in indirect semiconductors must involve a change in the electron wave vector. Due to the conservation of momentum, an indirect transition therefore is facilitated by an additional momentum - a phonon - leading to lower probability of photon absorption. This is one of the reasons why crystalline silicon with an indirect band gap requires a thick wafer (~ 100 μm)[11] to absorb all useful incident photons. Direct band gap semiconductors are better absorbers, e.g., CIGS (~ 2 μm)[12], CdTe (2 ~ 5 μm)[13].

The absorption coefficient can be expressed by the transition probability ($T_{i\to f}$) of an electron from the ground (initial) state to the excited (final) state, which is called as Fermi's golden rule,

$$T_{i\to f} = \frac{1}{h}|\langle f|H'|i\rangle|^2\, JDOS \qquad (1.3)$$

where, h is Planck constant, $\langle f|H'|i\rangle$ is the matrix element of the perturbation H' (solar photons) between the final and initial states, and JDOS is the joint density of states.[10] The matrix element describes the effect of external solar photons on the electrons in solids, which is practically determined by the possibility of the electric-dipole allowed transition, e.g., *s* → *p*, *d* → *p*.[14] The JDOS, describing the distribution of the available energy states within the bands, likely play a role in setting the magnitude of the absorption as well, since the density of atoms in a solid is huge. Thus, the absorption coefficient will approach to ideal step-like function when materials have a direct band gap and form a high JDOS with the character of the electric-dipole allowed transition near the band edge.

Second, assumed energy loss in the S-Q model is possible only by the thermalization to the band edges and by radiative recombination of electron-hole pairs. Unfortunately, real-world devices show considerably lower V_{OC} than the radiative limit[15], which implies presence of non-radiative recombination, such as Shockley-Read-Hall recombination[16,17]. This non-radiative recombination is usually relevant to defect states in the forbidden gap, where defects are commonly originated from impurities, dangling bonds, and disorder.[18] Thus, the recombination rate (R) is not directly the *np*-product, but according to Shockley-Read-Hall statistics,

$$\mathrm{R} = \frac{np - n_i^2}{(n+p)\tau} \qquad (1.4)$$

where, τ is the lifetime of the charge carrier, which is inversely proportional to concentration of midgap defect states in a material.[18] It is important to note that the reduction of the carrier life-

time or the increase of defect states leads to decrease of both V_{OC} and J_{SC} since the carrier life-time has effects on charge extraction as well. However, typical thin-film solar cells are far from defect-free and commonly have a trap density of 10^{14} cm^{-3} (τ = 1 ns).

Finally, the probability for the charge collection at short-circuit is unity. Figure 1.1 represents the simple schematic and the corresponding band diagrams of two common devices: *p*-*n* and *p*-*i*-*n* junctions. Both devices show the band bending and the band offsets due to the difference in the conductivity type and the band gap of the layers. Most devices are based on a *p*-type absorber layer since the mobility of electrons, minority carriers in *p*-type materials, is typically higher than that of holes. In a *p*-*n* junction, the band bending dominantly induces an asymmetry that helps to extract oppositely charged carriers at their respective contacts. The bands are steep and flat, leading to diffusion-based solar cells. In a diffusion-based solar cell, carrier mobilities and lifetimes must be large for efficient photovoltaic conversion.[6] For best performance of these devices radiative recombination is required.[18] Additionally, the band bending near the junction serves as a barrier for carriers, e.g. reflecting electrons to front contact and *vice versa*.

In order to solve the problems above, *p*-*i*-*n* junction solar cells can be considered as another option, where a relatively thick absorber layer is sandwiched between the *p*- and *n*-type layers. In this case, the built-in asymmetry in devices is mainly formed due to band offsets at the hetero-junction between two materials with different band gaps, not due to simply band bending. Thus, the *p*-*i*-*n* device configuration can induce drift of charge carriers by a built-in electric field and reduce the recombination at the interfaces. However, most current solar cell technologies adopting the *p*-*i*-*n* configuration rely primarily on diffusion rather than drift for photogenerated carrier extraction. Therefore, this assumption is rigorously valid in an ideal system requiring either sufficiently high carrier mobilities and lifetime, or strong absorption.

1.2.3 Current PV materials and their challenges

Today crystalline silicon (c-Si) cells are the most common in PV industry, benefiting from decades of well-developed technologies by the integrated circuit (IC) industry. The majority of silicon solar cells are fabricated from silicon wafers (~ 300 μm), which may be either single- or poly-crystalline. A single-crystal Si has a uniform molecular structure, leading to the long minority carrier lifetime (> 1 ms) and the highest energy conversion efficiency. There is a major limitation, however, in that the high-purity wafer is so expensive to process. Compared to the single-crystal Si, the poly-crystal Si has slightly lower wafer cost and less strict growth conditions. However, its lower manufacturing cost is offset by the lower energy conversion efficiency due to the grain boundaries. Reducing the cost of process is still being pursued through a number of avenues including improvement of the Si feedstock, production of kerfless wafers, and development of ultrathin Si wafer (5 – 50 μm).[19] Nevertheless the current efforts to diminish the manufacturing cost, the stagnant record efficiency of c-Si solar cells over the past decade due to low optical absorption has led many experts to believe that alternative thin-film PV cells will eventually dominate the marketplace one day and realize the goals of PV – a low price and reliable source of energy supply.[20]

The first report of CdTe PV devices appeared in the 1960s[21]; however, it was a flurry of improvement as a form of thin-films in 1990s[22]. CdTe crystallizes in either cubic sphalerite[23] or hexagonal wurtzite structure[24], where both Cd^{2+} and Te^{2-} are tetrahedrally coordinated as Si atoms in diamond structure. Thus, it is not surprising that the similar (covalent) bonding characters induce comparable transporting properties. CdTe has more intrinsic advantages as a light absorber than Si. It has a direct band-gap of 1.45 eV, which is well positioned to harness solar radiation.

Thus, 2 - 5 μm-thick CdTe thin-films are sufficient for making PV cells,[13] lowering the total material and manufacturing costs. And, the high thermodynamic stability together with its congruent sublimation enables CdTe to be deposited by various simple evaporation methods.[25] However, lots of intrinsic defects as both acceptors and donors limit practical doping (hole concentrations ~ 10^{15} cm^{-3}) by the self-compensation effect[26], as well as the V_{OC} degradation of PV cells[27]. Thus, at present, the issue of extending carrier lifetime is partially addressed by chemical passivation, such as the introduction of O_2 during CdTe growth, post-deposition $CdCl_2$ treatment, and controlled diffusion of Cu from back contact[19]. Final fundamental concerns are cadmium toxicity and tellurium availability.

The copper chalcopyrite has also been researched as a PV absorber since Kazmerski and coworkers introduced $CuInSe_2$ or CIS.[20] CIS has a direct band-gap of 1 eV. However, the band-gap has been continuously tuned over a very broad range (1 – 2.5 eV) by substituting either Ga for In or S for Se. The abbreviation CIGS is now used to describe this material, as current manifestations often involve either four or all five elements. CIGS crystallize in the chalcopyrite structure, which is the isoelectric analog of a binary sphalerite CdTe. It is formed by stacking two sphalerite unit cells together and replacing the Cd^{2+} with Cu^{+}, In^{3+}, or Ga^{3+}, and Te^{2-} with Se^{2-} or S^{2-} as shown in Figure 1.2. Because of the contribution of Cu *d* bands near VBM, CIGS has a higher optical absorption, resulting in a more efficient PV cell. It is, however, more complex to process since binary or ternary phases can be concomitant during or after the growth of the copper chalcopyrite.[28] This complexity leads that the comparable efficiency to c-Si has only been realized in the laboratory. Also, based on known mineral reserves and extraction costs, Indium does not have good long term potential for the sort of large scale deployment required to meet projected world electrical energy needs.

The final class of materials includes earth-abundant metal oxides and sulfides that have band-gaps in the range of 1 – 2 eV. Notable examples include cuprous oxide[29] and fool's gold (pyrite)[30], but the most successful system to date has been CZTS pioneered by Katagiri[31]. CZTS shares great similarities with CIGS, including similar device structures and fabrication techniques for the formation of the absorber layer. The similarities may have accelerated CZTS solar cells' initial success, but these same similarities may become limitations in the long run.

Despite the advantages on the manufacturing costs, no current thin-film PV devices have realized the necessary efficiency to compete with conventional energy sources as well as c-Si. Therefore, there is clearly need for even more improvement on the energy conversion efficiency.

1.2.4 Materials design principles for high efficient PV materials

Our strategy for high efficiency PV devices is to design new materials with strong optical absorption so that they can be employed in a drift-based thin-film solar cell, where carrier mobility and lifetime requirement are significantly relaxed since the presence of an internal electric field aids carrier extraction. For an efficient drift-based thin-film solar cell, the absorber layer requires very strong absorption with an abrupt onset near the band gap, such that thickness can be reduced to less than 1 μm.

As described previously, thermodynamic considerations are commonly used to assess the efficiency limits of a solar absorber material. Recently, a new and improved analysis methodology, the spectroscopic limited maximum efficiency (SLME), was proposed by Yu and Zunger.[2] Building on the original Shockley-Queisser approach in which photovoltaic absorber candidates are selected solely on the basis of their band gap, SLME incorporates absorption, emission, and

recombination considerations to account for a spread of different efficiencies for materials with the same band gap.

Chemical insight along with SLME can be effectively used to identify material candidates for high-efficiency photovoltaic absorbers. Recently, our group has extended the SLME framework to identify new design principles for absorbers, such as Cu_3SbS_4 and $CuSbS_2$, in the Cu-M-VI family (M = group 13-15; VI = S, Se).[3] Two design rules were proposed: i) choosing a cation stoichiometry Cu/M > 1 leading to isolated M atoms, or ii) including a M element with a ns^2 electronic configuration can provide a high JDOS, resulting in a strong absorption coefficient. For example, Famantine (Cu_3SbS_4) has a tetragonal crystal structure (space group *I-42m*)[32] and contains a cation stoichiometry of Cu/Sb > 1 with high-valence Sb^{5+} atoms isolated within the structure (Figure 1.2b). This results in narrow Sb-derived *s* bands, translating into a high DOS near CBM. In contrast, chalcostibite ($CuSbS_2$, space group *Pnma*)[33] has low-valence Sb^{3+} atoms, which exhibit stereochemical activity of lone pair electrons, leading to a distorted crystal structure (Figure 1.2b).[34] The $CuSbS_2$ structure is composed of edge-shared square pyramidal SbS_5 units separated by CuS_4 tetrahedra, which forms a layered structure within the space separating SbS_5 units. In this distorted environment, low-valence Sb^{3+} atoms result in a narrow dispersion for Sb *s*-orbital and *p*-orbital derived bands, presenting a higher DOS near the VBM and the CBM, respectively.[2] Consistent with the computed assessment, both materials have a stronger absorption, when compared to conventional thin-film absorber materials such as $CuInSe_2$ and CdTe.[35] In this contribution, the combination of these two design principles can lead to develop new inorganic materials exhibiting higher absorption coefficients than previous solar absorbers.

1.3 Thermoelectrics: Basic principles and new materials developments

1.3.1 Basic principles

The TE effect is the direct conversion of a thermal gradient to an electric potential and *vice-versa*. A typical TE device for electricity generation is shown in Figure 1.3, where *n*-type and *p*-type TE materials are interconnected on the cold and the hot sides. An applied temperature difference causes charged carriers (electrons and holes) in the materials to diffuse from the hot side to the cold side in parallel. The conversion efficiency of a TE material is often stated as the dimensionless figure of merit, ZT, where T is the absolute temperature and Z is related to material properties.[9] Attempts to maximize ZT must meet two materials-design challenge of simultaneously achieving i) large power factor (PF = $S^2\sigma$) to generate high electrical voltage and current, and ii) low thermal conductivity (κ) to keep the temperature gradient exploited for generating the electrical energy, *cf.* Equation (1.5).

$$\mathrm{ZT} = \frac{S^2\sigma}{\kappa}T \qquad (1.5)$$

where σ is electrical conductivity and S is thermopower. However, the heat conduction and the electrical resistance are parasitic; in other words, the electrical conductivity is strongly related with the thermal conductivity. And, an inverse correlation between the electrical conductivity and the thermopower is common for many carrier-doped semiconductors. Thus, κ, σ, and S are commonly correlated properties. High electrical conductivity, for example, is often associated with low thermopower and/or high thermal conductivity, and such correlations depress ZT. As a result, the ZT of commercial TE materials has remained near 1 in the face of contradicting inter-related properties.

1.3.2 Strategies for high efficient thermoelectric materials

1.3.2.1 Increasing the power factor

The power factor, PF= $S^2\sigma$, is typically optimized as a function of carrier concentration, through doping, in order to increase the electrical conductivity, $\sigma = nq\mu$, where n is the carrier concentration, q is the electric charge, and μ is the carrier mobility.[9] However, high carrier concentration results in low thermopower due to the inverse relationship between thermopower and carrier concentration,

$$S = \frac{8\pi^2\kappa_B^2}{3eh^2} m_d^* T \left(\frac{\pi}{3n}\right)^{2/3} \qquad (1.6)$$

where κ_B is the Boltzmann constant and m_d* is the density-of-state (DOS) effective mass of the carrier from parabolic band with energy-independent scattering approximation.[36] The interrelationship between carrier concentration, electrical conductivity, and thermopower in common TE materials must reach a compromise to maximize PF and then ZT.[37] This balance generally occurs at carrier concentration between 10^{19} and 10^{20} cm^{-3}, which complies with that of heavily doped semiconductors. And, TE materials should have only a single type of carrier to ensure high thermopower since mixed *n*- and *p*-type carriers will cancel out the induced TE voltage by moving oppositely.

The effective mass of the charge carrier provides another challenge. Large effective mass leads to high thermopower (refer Equation (1.6)), but it produces low carrier mobility and decreases electrical conductivity, $\mu = e\tau/m_i^*$, where τ is the mean scattering time between collisions for the carriers and m_i* is inertial or band effective mass. Here, we need to distinguish two different terminologies for effective mass. A large DOS effective mass can be achieved by either flat bands or a large number of bands, but inertial effective mass solely depends on each band

unless there is significant inter-valley scattering.[36,38] As a result, forming multiple bands with a low inertial effective mass near E_F is expected to enhance both electrical conductivity and thermopower (a large DOS effective mass), and produce a large power factor.[38]

From the above discussion, band-tuning is an important strategy to improve thermopower without depressing electrical conductivity. Here are other current approaches to boost the power factor through the band-tuning (see details in recent reviews ref. 38 &39): by electronic resonance states, increasing the band gap for depressing bipolar effect, electron energy barrier filtering, and highly mismatched isoelectric doping.

1.3.2.2 Increasing Low thermal conductivity

Additional materials-design conflicts come from the necessity for low thermal conductivity, even though we can overcome the aforementioned challenges between thermopower and electrical conductivity. The thermal conductivity contains two components: electronic, κ_{el}, arising from electrons or holes transporting heat and lattice, κ_L, arising from phonons travelling through the lattice. Thus, the electrical conductivity makes another conflict with the thermal conductivity through the electronic contribution according to the Wiedeman-Franz (WF) law, $\kappa_{el} = L\sigma T$, where L is the Lorenz number, 2.4×10^{-8} $J^2K^{-2}C^{-2}$ for free electron. [36] On the other hand lattice thermal conductivity varies with material structure, which is largely independent of electronic transport properties. Indeed, the TE efficiency has greatly enhanced by minimizing κ_L from various scattering sources to block phonon propagation.[36–39]

The classical kinetic theory of a gas provides a good approximation for the lattice thermal conductivity,

$$\kappa_L = {}^1/_3\, C_v l v_s \qquad (1.7)$$

where, C_v is the specific heat per unit volume, l is the mean free path of phonon, and the v_s is the average velocity of sound.[40] At high temperature (T ≥ 300 K), the lattice thermal conductivity depends primarily on l, which is determined by phonon-phonon scattering since the C_v approaches the classical value, 3R, according to the Dulong-Petit law.[41] This indicates that the minimum lattice thermal conductivity, $\kappa_{L,min}$, can be achieved when all the phonons have a mean free path equal to the interatomic distance between constituent atoms.[36,37] Glasses exhibit the lowest lattice thermal conductivity, $\kappa_L \sim 0.25$ $Wm^{-1}K^{-1}$, comparable to this minimum, $\kappa_{L,min}$, and this result leads to the concept for reducing the lattice thermal conductivity. That is, one effective way to decrease κ is to incorporate a glass-like unit in materials.

In the phonon-phonon scattering dominant region, the Keyes's expression provides more practical guidelines to depress the lattice thermal conductivity,

$$\kappa_L T = \frac{R^{3/2}}{3\gamma^2 \varepsilon^2 N_0^{1/3}} \frac{T_m^{3/2} \rho^{3/2}}{A^{7/6}} \qquad (1.8)$$

where, T_m is the melting point, A is the mean atomic weight, γ is the Grüneisen parameter, ε is the fractional amplitude of interatomic thermal vibration, R is the ideal gas constant, N_0 is Avogadro's constant, and ρ is the density.[36] It can be seen that κ_L decrease with temperature at high temperature, a low melting point, large interatomic distance, and high atomic mass.

1.3.3 Current TE materials and their challenges

Numerous thermoelectric materials have been researched to realize high ZT. As described previously, it is possible to design new promising TE materials with two approaches: either the power factor is maximized and/or the thermal conductivity is minimized. The latter of two has guided a more effective way because the thermal conductivity is the only parameter not deter-

mined by the electronic structure, offsetting interrelated physical properties. Especially, reducing of κ_L is key to achieve high performance thermoelectrics since κ_L is largely independent of electronic transport properties.

Early works by alloying the binary tellurides of Bi_2Te_3, Sb_2Te_3, and GeTe, greatly reduced thermal conductivity, $\kappa_L > 0.75$ $Wm^{-1}K^{-1}$ and Bi_2Te_3 alloys produced the long-standing ZT ~ 1, through disorder within the unit cell.[42] It is well known that such disorder leads to phonon scattering and reduced thermal conductivity.[43] Bi_2Te_3 crystallizes in the rhomobohedral structure (space group *R-3m*), forming 2-*D* plats stacked by week van der Waals interactions along the *c*-axis. This structural feature enables Bi_2Te_3 alloys to enhance thermoelectric performance in the form of the artificially constructed superlattice, in which the extraordinarily small κ_L of 0.24 and high ZT of 2.4 were claimed.[44] There is a major limitation, however, in that fabricating such tailed nanostructures is difficult and their phases are thermodynamically unstable at high temperature.[45] Therefore, this disorder state-of-the-art has actively researched in the single-phase materials to induce phonon scattering through interstitial sites, partial occupancies, or rattling atoms, as well as compounds with low dimensionality.

Rare-earth chalcogenides, e.g., $La_{3-x}Te_4$, with the Th_3P_4 structure form the large number of random vacancies (x in $La_{3-x}Te_4$), resulting in phonon scattering and reduction of κ_L (0.4 $Wm^{-1}K^{-1}$).[46] This concept has extended in the crystals containing "rattler" atoms, e.g., clathrates and skutterudites.[47–49] Clathrates such as $Ba_8Ga_{16}Ge_{30}$, contain corner-sharing tetrahedral frameworks, made up of Group 13 or 14, derived from the sphalerite. Cavities in the framework are occupied by large electropositive atoms of Group 1 or 2. Likewise, in skutterudites, corner-sharing $CoSb_6$ octahedra forms framworks as a distorted variant of the ReO_3 structure, containing rattering atoms such as La or Ce. In both compounds, frameworks form electrically conduc-

tive pathways, while rattlers within the frameworks are presumed to enhance phonon scattering and lower lattice thermal conductivity. Indeed, complex clathrate and skutterudite compositions have been reported to exhibit ZT > 1, along with low κ_L < 1 $Wm^{-1}K^{-1}$.[49] Materials with asymmetrically coordinated atoms can also induce atomic disorder within the unit cell to generate strong phonon scattering, translating to a reduction in κ_L. Such anharmonicity has, for example, been invoked to account for the large lattice thermal resistance in solids containing cations with ns^2 electron configuration, e.g., Cu_3SbSe_3.[50]

Low thermal conductivity can be achieved in crystal with the complex structure, e.g., $CsBi_4Te_6$[51], Zn_4Sb_3[52,53] and Zintle ($Yb_{14}MnSb_{11}$)[36] compounds. $CsBi_4Te_6$ is a complex variant of Bi_2Te_3. This compound exhibits a somewhat lower lattice thermal conductivity than Bi_2Te_3 that has been ascribed to the added complexity of the Cs layers and the few Bi-Bi bonds in $CsBi_4Te_6$ not found in Bi_2Te_3. As many of these materials have low lattice thermal conductivities, but to date the best ZT < 0.8 due to doping limit to appropriate carrier concentrations. Zn_4Sb_3 is another promising candidate, displaying exceptionally low thermal conductivity. In this compound, about 20 % of the Zn atoms occupy interstitial sites, resulting in significant local lattice distortions and glass-like phonon scattering. For example, the ZT value of Cd-doped Zn_4Sb_3 reached 1.3 at 670 K.[53] Complex Zintle compounds have recently emerged as a promising intermetallic TE material for very high temperature applications (> 1000 K). This compound crystalize in complex cubic structure, containing a valence-balanced combination of both ionic (Yb-Sb) and covalent (Mn-Sb, Sb-Sb) bonds. The combination of the bonding types leads to the complex structure having multiple sub-structural units within the unit cell, resulting in low lattice thermal conductivity κ_L ~ 0.4 $Wm^{-1}K^{-1}$. Due to the stability at high temperature, NASA has actively developed these compounds as the future TE generators.

The development of new materials and complex composites over last decade has greatly increased ZT values. Today, the latest generation of bulk materials reached ZT ~ 1.7 at 700 ~ 800 K, mainly guided by the reduction of the lattice thermal conductivity. However, the low thermal conductivity was usually achieved with heavy and sometimes toxic elements, which limits practical applications of TE materials. In this context, the environment friendly materials with the light-weight components will support of sustainable society.

1.4 Summary

Two approaches, photovoltaic and thermoelectric, to meet the needs for renewable energy are discussed in this dissertation. To achieve this ambitious goal, the discovery of new promising materials requires a combination of keen chemical intuition, theoretical guidance, synthetic chemistry expertise, materials processing, and good measurement skills. The work presented in here was performed by this powerful combination to both offer materials design principles and identify promising candidates.

Chapter 2, 3, and 4 detail an exploration of new multi-functional tetrahedrites as photovoltaic and thermoelectric materials. The tetrahedrite, typified by $Cu_{12}Sb_4S_{13}$, contains unique structural building blocks with Sb or Te atoms having ns^2np^0 electron configuration. This configuration leads to enhanced optical absorption with a rapid onset near the band gap. Interestingly, this structural feature also encompasses materials design approaches for realizing low thermal conductivities, which play a primary role in maximizing thermoelectric efficiency. In addition, optical, electrical, and thermal properties can be tuned via selective chemical substitutions, allowing optimization of properties toward improved performance. Chapter 5 describes materials in the system Cu_3-V-VI_4 (V = P, As, Sb; VI = S, Se) as absorber candidates. This work demonstrates

that the band gaps of this family via mixed composition can be tuned between 0.6 and 2.4 eV with attendant hole mobilities up to 15 $cm^2V^{-1}s^{-1}$. These properties coupled with relatively low synthesis temperatures ($T < 450\ ^oC$) makes members of this family especially attractive as candidates for new polycrystalline thin film solar cells in a tandem configuration. Chapter 6 attempts to find the missing Co_2GeS_4 compound through $(Fe,Co)_2GeS_4$ and $(Co,Zn)_2GeS_4$ solid solutions by a systematic investigation between theoretical prediction and experimental results. More generally, this fundamental research creates a practical framework for future design principle based search and discovery of effective materials.

References

[1] W. Shockley, H. J. Queisser, *J. Appl. Phys.* **1961**, *32*, 510.

[2] L. Yu, A. Zunger, *Phys. Rev. Lett.* **2012**, *108*, 068701.

[3] L. Yu, R. S. Kokenyesi, D. a. Keszler, A. Zunger, *Adv. Energy Mater.* **2013**, *3*, 43.

[4] International Energy Agency, "Tracking Clean Energy Progress 2013," can be found under http://www.iea.org./etp/tracking/, **2013**.

[5] M. A. Green, K. Emery, Y. Hishikawa, W. Warta, E. D. Dunlop, *Prog. Photovoltaics Res. Appl.* **2012**, *20*, 12.

[6] P. Jackson, D. Hariskos, E. Lotter, S. Paetel, R. Wuerz, R. Menner, W. Wiltraud, M. Powalla, *Prog. Photovoltaics Res. Appl.* **2011**, *19*, 894.

[7] Solar Energy Industries Association, "Solar Market Insight Report 2013 Q2," can be found under http://www.seia.org/research-resources/solar-market-insight-report-2013-q2/, **2013**.

[8] T. M. Tritt, *Recent Trends in Thermoelectric Materials Research*, Academic, **2001**.

[9] C. B. Vining, *Nat. Mater.* **2009**, *8*, 83.

[10] M. Fox, *Optical Properties of Solids*, Oxford University Press, New York, **2010**.

[11] A. Shah, P. Torres, R. Rscharner, N. Wyrsch, H. Keppner, *Science* **1999**, *285*, 692.

[12] I. Repins, S. Glynn, J. Duenow, T. J. Coutts, W. Metzger, M. A. Contreras, San Diego, **2009**, p. 7409.

[13] R. Scheer, H.-W. Schock, *Chalcogenide Photovoltaics: Physics, Technologies, and Thin Film Devices*, Wiley-VCH, Wienheim, **2011**.

[14] D. J. Griffiths, *Introduction to Quantum Mechanics*, Printice Hall, New Jersey, **1995**.

[15] U. Rau, J. H. Werner, *Appl. Phys. Lett.* **2004**, *84*, 3735.

[16] W. Shockley, W. T. J. Read, *Phys. Rev.* **1952**, *87*, 835.

[17] R. N. Hall, *Phys. Rev.* **1952**, *87*, 387.

[18] D. Abou-Ras, T. Kirchartz, U. Rau, *Advanced Characterization Techniques for Thin Film Solar Cells*, Wiley-VCH, Germany, **2011**.

[19] A. Luque, S. Hegedus, *Handbook of Photovoltaic Science and Engineering*, Wiley, Chichester, **2011**.

[20] NREL, *Research Cell Efficiency Records*, **2013**.

[21] D. A. Cusano, *Solid State Electron.* **1963**, *6*, 217.

[22] J. Britt, C. Ferekides, *Appl. Phys. Lett.* **1993**, *62*, 2851.

[23] M. L. Cohen, T. K. Bergstresser, *Phys. Rev.* **1966**, *141*, 789.

[24] S.-H. Wei, S. B. Zhang, *Phys. Rev. B* **2000**, *62*, 6944.

[25] B. McCandless, MRS, **2001**.

[26] M. Burgelman, *Thin Film Solar Cells*, Wiley-VCH, Weinheim, **2006**.

[27] C. S. Ferekides, D. L. Morel, *NREL* **2011**.

[28] S. B. Zhang, S. Wei, A. Zunger, **1998**, *57*, 9642.

[29] A. O. Musa, T. Akomolafe, M. J. Carter, *Sol. Energy Mater. Sol. Cells* **1998**, *51*, 305.

[30] L. Yu, S. Lany, R. Kykyneshi, V. Jieratum, R. Ravichandran, B. Pelatt, E. Altschul, H. a. S. Platt, J. F. Wager, D. a. Keszler, A. Zunger, *Adv. Energy Mater.* **2011**, *1*, 748.

[31] H. Katagiri, *Thin Solid Films* **2005**, *480-481*, 426.

[32] J. Garin, E. Parthé, *Acta Crystallogr. Sect. B Struct. Crystallogr. Cryst. Chem.* **1972**, *28*, 3672.

[33] M. F. Razmara, C. M. B. Henderson, R. A. D. Pattrick, J. M. Charnock, *Mineral. Mag.* **1997**, *61*, 79.

[34] A. Walsh, D. J. Payne, R. G. Egdell, G. W. Watson, *Chem. Soc. Rev.* **2011**, *40*, 4455.

[35] J. Heo, R. Ravichandran, C. F. Reidy, J. Tate, J. F. Wager, D. A. Keszler, *Adv. Energy Mater.* **n.d.**, Submitted.

[36] J. R. Sootsman, D. Y. Chung, M. G. Kanatzidis, *Angew. Chemie Int. Ed.* **2009**, *48*, 8616.

[37] G. J. Snyder, E. S. Toberer, *Nat. Mater.* **2008**, *7*, 105.

[38] Y. Pei, H. Wang, G. J. Snyder, *Adv. Mater.* **2012**, *24*, 6125.

[39] J. P. Heremans, B. Wiendlocha, A. M. Chamoire, *Energy Environ. Sci.* **2012**, *5*, 5510.

[40] N. W. Ashcroft, N. D. Mermin, *Solid State Physics*, Belmont, **1976**.

[41] A.-T. Petit, P.-L. Dulong, *Ann. Chim. Phys.* **1819**, *10*, 395.

[42] P. F. P. Poudeu, J. D. Angelo, H. Kong, A. Downey, J. L. Short, R. Pcionek, T. P. Hogan, C. Uher, M. G. Kanatzidis, *J. Am. Chem. Soc.* **2006**, *9*, 14347.

[43] R. Venkatasubramanian, E. Siivola, T. Colpitts, B. O'Quinn, *Nature* **2001**, *413*, 597.

[44] O. Delaire, J. Ma, K. Marty, a F. May, M. a McGuire, M.-H. Du, D. J. Singh, a Podlesnyak, G. Ehlers, M. D. Lumsden, B. C. Sales, *Nat. Mater.* **2011**, *10*, 614.

[45] C. Wood, *Reports Prog. Phys.* **1988**, *51*, 459.

[46] G. S. Nolas, J. Poon, M. Kanatzidis, *MRS Bull.* **2006**, *31*, 199.

[47] N. P. Blake, S. Latturner, J. D. Bryan, G. D. Stucky, H. Metiu, *J. Chem. Phys.* **2001**, *115*, 8060.

[48] X. Shi, J. Yang, J. R. Salvador, M. Chi, J. Y. Cho, H. Wang, S. Bai, J. Yang, W. Zhang, L. Chen, *J. Am. Chem. Soc.* **2011**, 7837.

[49] E. J. Skoug, D. T. Morelli, *Phys. Rev. Lett.* **2011**, *107*, 235901.

[50] Y. Zhang, E. Skoug, J. Cain, V. Ozoliņš, D. Morelli, C. Wolverton, *Phys. Rev. B Condens. Matter* **2012**, *85*, 054306.

[51] D.-Y. Chung, T. Hogan, P. Brazis, M. Rocci-Lane, C. Kannewurf, M. Bastea, C. Uher, M. G. Kanatzidis, *Science (80-.).* **2000**, *287*, 1024.

[52] H. W. Mayer, I. Mikhail, K. Schubert, *J. Less Common Met.* **1978**, *59*, 43.

[53] V. . Kuznetsov, D. . Rowe, *J. Alloys Compd.* **2004**, *372*, 103.

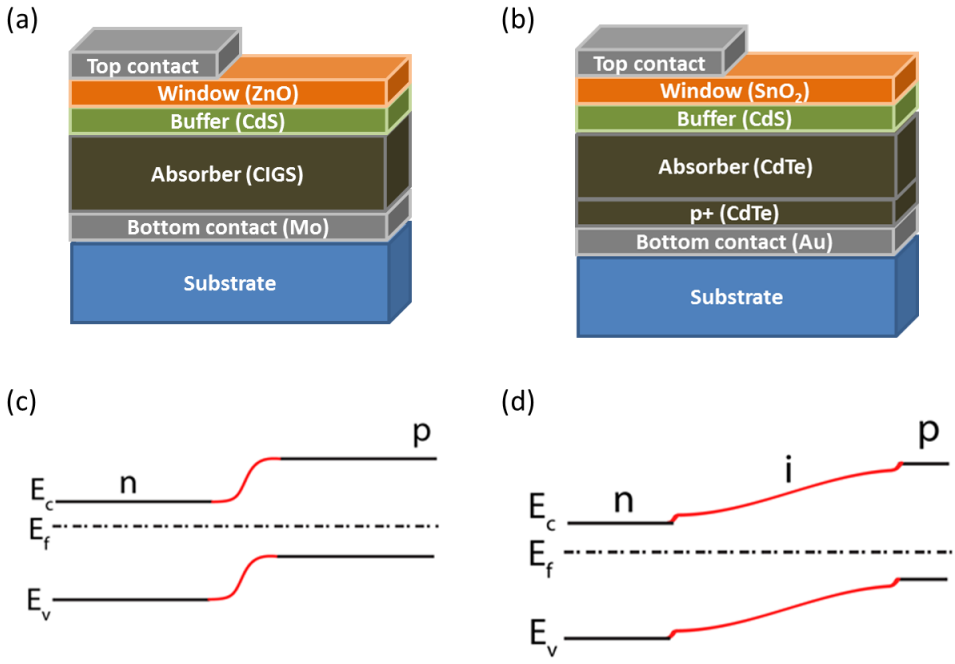

Figure 1.1. Schematic cross-section of typical (a) Cu(In,Ga)S_2 (*p*-*n*) and (b) CdTe (*p*-*i*-*n*) solar cells. (c) and (d) represent the corresponding band diagrams of (a) and (b), respectively.

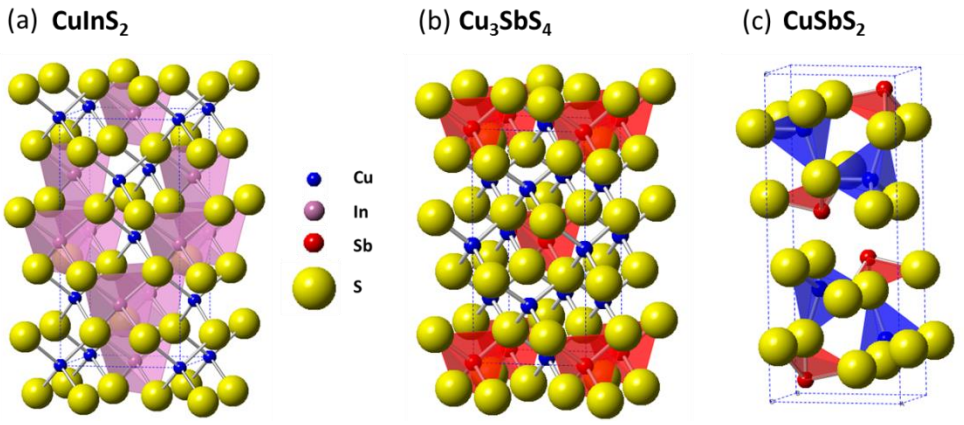

Figure 1.2. Crystal structures of (a) $CuInS_2$, (b) Cu_3SbS_4, and (c) $CuSbS_2$. All directions are slightly off plane (100).

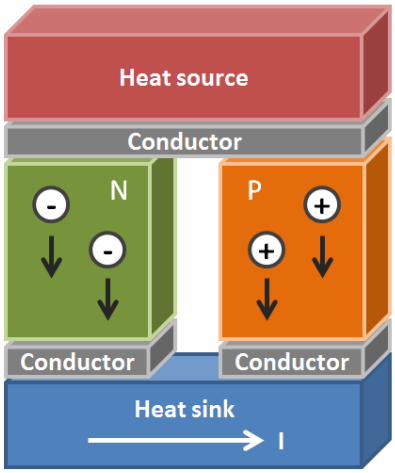

Figure 1.3. A schematic of thermoelectric modul showing the direction of charge flow on both cooling and power generation.

Chapter 2

Design Meets Nature: New Tetrahedrite Solar Absorbers

Jaeseok Heo[1], Ram Ravichandran[2], John F. Wager[2], and Douglas A. Keszler[1]

[1]Department of Chemistry, Oregon State University, Corvallis, Oregon 97331-4003 USA

[2]School of Electrical Engineering and Computer Science, Oregon State University, Corvallis, Oregon 97331-5501 USA

Submitted for publication in *Advanced Energy Materials*.

2.1 Introduction

With rapid increases in photovoltaic manufacturing and as balance-of-system costs decrease, harnessing solar energy for large-scale energy generation constitutes a growing share of global renewable energy production. These costs are driven in large part by the need to maximize light-to-electricity efficiency. Technical advances have resulted in single-junction crystalline silicon (c-Si) solar cells with a record efficiency of 28.3 %[1] and efficiencies as high as 43.5 % in GaAs multi-junction tandem cells[2]. Thin-film solar cells (TFSCs) offer reduced materials utilization along with the ability for possibility of flexible substrate integration. Laboratory scale efficiencies of 18 % for CdTe[1] and 20.3 % for $Cu(In,Ga)Se_2$ (CIGS)[3] solar cells have been achieved. However, toxicity and/or relative abundance considerations with respect to constituent elements could limit the large-scale deployment of CdTe- and CIGS-based TFSCs. As a result, for TFSCs to be a larger contributor of the overall net electricity generation, new earth-abundant and environmentally benign solar cell materials have to be developed.

Our focus in this contribution is to design new materials with strong optical absorption so that they can be employed in a drift-based TFSC. Most current solar cell technologies, e.g., c-Si, GaAs, and CIGS, rely primarily on diffusion rather than drift for photogenerated carrier extraction. Carrier mobilities and lifetimes must be large for efficient photovoltaic conversion in a diffusion-based solar cell.[4] In contrast, carrier mobility and lifetime requirements are significantly relaxed in a drift-based solar cell, such as amorphous silicon, since the presence of an internal electric field aids carrier extraction. For an efficient drift-based TFSC, the absorber layer requires very strong absorption with an abrupt onset near the band-gap, such that the thickness can be reduced to less than 1 μm.

Thermodynamic considerations, outlined by Shockley and Queisser,[5] are commonly used to assess the efficiency limits of a solar absorber material. Recently a new and improved analysis methodology, the spectroscopic limited maximum efficiency (SLME), was proposed by Yu and Zunger.[6] Building on the original Shockley-Queisser approach in which photovoltaic absorber candidates are selected solely on the basis of their band gap, SLME incorporates absorption, emission, and recombination considerations to account for a spread of different efficiencies for materials with the same band gap.[6]

Chemical insight along with SLME can be effectively used to identify material candidates for high-efficiency photovoltaic absorbers. Recently, our group used the SLME framework to identify new design paradigms for absorbers such as Cu_3SbS_4 in the Cu-M-VI family (M = group III - V; VI= S, Se).[7] Two design rules were proposed: i) choosing a cation stoichiometry Cu/M > 1 leading to isolated M atoms, or ii) including a M element with a s^2p^0 low valence electronic configuration can provide a high joint density of states (JDOS), resulting in a strong absorption coefficient. In this contribution, these two design principles are merged by combining the effect of isolation and low valence to develop new inorganic materials exhibiting higher absorption coefficients than previous solar absorbers. It is shown that the tetrahedrite family validates our M atom isolation and low valence design rules. Moreover, the electrical and optical properties of tetrahedrites may be tuned for photovoltaic applications by cation (Mn, Zn, In) and/or anion (Se) substitutions.

2.2 Tetrahedrite as a Unique Material

Among ternary and multinary copper chalcogenides, tetrahedrites have attracted limited interest[8–11] despite being known for several decades[12]. Compounds of the tetrahedrite family crystal-

lize in a cubic structure (space group *I-43m*)[13] shown in Figure 2.1a. The aforementtioned chemical formula can be rationalized from a crystal structral point of view as $Cu_6Cu_6[SbS_3]_4S$, wherein half of the Cu atoms occupy four-coordinate, distorted tetrahedrial sites and half occupy three-coordinate triangular sites. The CuS_4 units are condensed via vertex sharing into a highly defective framework are occupied by the isolated structural unit of CuS_3 and SbS_3 groups shown in Figure 2.1b. This description is important because it clearly illustrates two features relevant to absorber performance of tetrahedrite. First, the outer framework, formed by the (largely) covalent bonding between cation (Cu) and the anion (S), plays a vital role in establishing electronic transport properties. Second, structural localization due to the isolated cavity polyhedron is key to achieving strong absorption. Thus, tetrahedrites have attractive electro-optical properties, since the inner cavity facilitates strong optical absorption, while the outer framework provides an efficient conduction pathway.

2.2.1 Can Tetrahedrite Compounds Show High Absorption?

We start by considering the relationship between the crystal structure shown in Figure 2.1, the electronic density of states (DOS) given in Figure 2.2a, and experimental absorption coefficients indicated in Figure 2.2b for the Cu-Sb-S system in order to assess whether tetrahedrite compounds meet our design-paradigm criteria. Famantine (Cu_3SbS_4) has a tetragonal crystal structure (space group *I-42m*)[14] and contains a cation stoichiometry of Cu/Sb > 1 with high-valence Sb^{5+} atoms isolated within the structure (refer to Figure 2.1d). This results in narrow Sb-derived s bands, translating into a high DOS near the conduction band minima (CBM). In contrast, both chalcostibite ($CuSbS_2$, space group *Pnma*)[15] and tetrahedrite ($Cu_{12}Sb_4S_{13}$) have low-valence Sb^{3+} atoms, which exhibit stereochemical activity due to the effect of lone pair electrons, leading to a distorted crystal

structure.[16] The $CuSbS_2$ structure is composed of edge-shared square pyramidal SbS_5 units separated by CuS_4 tetrahedra, which forms a layered structure within the space separating SbS_5 units (Figure 2.1e). In this distorted environment, low-valence Sb^{3+} atoms result in a narrow dispersion for Sb s-orbital and p-orbital derived bands, presenting a higher DOS near the valence band maxima (VBM) and the CBM, respectively.[7] Since in both Cu_3SbS_4 and $CuSbS_2$, these flat-band characteristics near the VBM and/or the CBM lead to a high JDOS, the same considerations apply to $Cu_{12}Sb_4S_{13}$, where low-valence Sb^{3+} atoms form a large cavity polyhedron within the structure.

Figure 2.2a shows the electronic density of states near the CBM for $CuInSe_2$, Cu_3SbS_4, $CuSbS_2$, and $Cu_{12}Sb_4S_{13}$ as obtained from density-functional theory (DFT) calculations. While $CuSbS_2$ and $Cu_{12}Sb_4S_{13}$ both contain low-valence Sb atoms, and similar band character (Sb p-derived orbitals at CBM), $Cu_{12}Sb_4S_{13}$ exhibits considerably narrower Sb s- and p-like bands, pushing the VBM down and/or the CBM up, thereby increasing the band gap compared to $CuSbS_2$. These flat-band characteristics near both the VBM and CBM should contribute to a large JDOS, resulting in an increased absorption coefficient. In addition, electric dipole allowed Cu d → Sb p, S p and Sb s → Sb p transitions will enhance the transition matrix element for $Cu_{12}Sb_4S_{13}$. The calculated total density of states is shown in Figure S2.3. Consistent with the computed assessment, $Cu_{12}Sb_4S_{13}$ thin-films have an extremely strong absorption (refer Figure 2.2b) with an abrupt onset at the band gap, when compared to conventional thin-film absorber materials such as $CuInSe_2$ and CdTe. In addition, the absorption strength for $Cu_{12}Sb_4S_{13}$ is higher than Cu_3SbS_4 and $CuSbS_2$ as shown in Figure 2.2b, indicating that strong absorption in $Cu_{12}Sb_4S_{13}$ thin-films arises from the cavity polyhedron in addition to low valence and isolated Sb atoms in the structure.

2.2.2 $Cu_{12}Sb_4S_{13}$: An Intrinsic Degenerate *p*-type Semiconductor

The absorption coefficient of $Cu_{12}Sb_4S_{13}$ is shown in Figure 2.3. It is evident that $Cu_{12}Sb_4S_{13}$ thin-films exhibit significant sub-band gap absorption ($\alpha \sim 3\times10^4$ cm^{-1}). To probe the origin of this sub-band gap absorption, we need to take into account the oxidation states of the Cu atoms. The triangular planar CuS_3 sites are characterized only by d^{10} Cu^{1+}, while the tetrahedral CuS_4 sites are formally occupied by a mixture of Cu^{1+} and Cu^{2+}.[17] Similar to the mixed valence case of Fe_3O_4,[18] charge transfer along the CuS_4 framework due to this mixed valency is one possible explanation for the relatively low resistivity of 0.001 - 0.004 Ω cm measured in $Cu_{12}Sb_4S_{13}$ thin-films and powders (listed in Table 2.1). This unique feature results in a carrier concentration greater than 10^{20} cm^{-3}, making $Cu_{12}Sb_4S_{13}$ an intrinsic degenerate semiconductor, with thin-films exhibiting high sub-band gap absorption and low resistivity. A degenerate *p*-type semiconductor is not desirable as an absorber material. However, $Cu_{12}Sb_4S_{13}$ may be useful as a as a p+ contact in a drift-based heterojunction TFSC.

2.3 Converting $Cu_{12}Sb_4S_{13}$ to a non-degenerate semiconductor

To reduce the carrier concentration in $Cu_{12}Sb_4S_{13}$, we substitute Mn^{2+}, Zn^{2+}, or In^{3+} into the base tetrahedrite composition. The crystal structure of synthesized powders and thin-films are confirmed by analysis of high-resolution XRD patterns (Figure S2.1-S2.4). The substituted Mn, Zn, and In atoms are likely to occupy the tetrahedral CuS_4 sites, since it has been demonstrated in previous work that Fe, Zn, and Hg atoms selectively replace these Cu atoms.[11,19,20] The Zn derivative $Cu_{10}Zn_2Sb_4S_{13}$, for example, exhibits a resistvity very much higher than that of $Cu_{12}Sb_4S_{13}$. Zn substitution represents an isovalent replacement of Zn^{2+} for Cu^{2+}, but Zn^{2+} has a d^{10} electron configuration rather than the d^9 configuration of Cu^{2+}. In principle, these additional electrons from Zn^{2+} lead to a filled valence band and the larger observed resistivity (5.5 – 10 Ω cm, Table 2.1)

generally associated with the intrinsic nature of a semiconductor. For example, the absorption coefficient for a $Cu_{10}Zn_2Sb_4S_{13}$ thin-film as shown in Figure 3a exhibits a strong reduction in sub-band gap absorption. In addition, both bulk powders and thin-films of $Cu_{10}Zn_2Sb_4S_{13}$ have an increased resistivity in comparison to $Cu_{12}Sb_4S_{13}$ as shown in Table 2.1. We have also fabricated $Cu_{11}In^{3+}Sb_4S_{13}$ in both pellets and thin-films, and similar to their Zn substituted counterpart, the In- substituted samples exhibit similar trends of reduced sub-band gap absorption (Figure 2.3a) and increased resistivity (Table 2.1) compared to $Cu_{12}Sb_4S_{13}$. Interestingly, the absorption coefficients of all three samples with and without substitutions display similar band gaps ($E_G \sim 1.8$ eV) and absorption onset characteristics, implying that substitution of Zn, or In does not affect the DOS near the VBM or CBM. While the carrier concentration is reduced in substituted tetrahedrites, the band gap is still larger than optimal (1.1 - 1.5 eV)[21] for single-junction TFSCs. However, this higher band gap may be of interest for development of a tandem solar cell.

2.4 Tuning the Band-gap of $Cu_{10}Zn_2Sb_4S_{13}$

We now turn to an alternate approach to tune the band gap of a tetrahedrite. By substituting Se into X and Y anion sites, we synthesize a new tetrahedrite compound $Cu_{10}Zn_2Sb_4Se_{13}$ in both powder and thin-film form, as confirmed via high-resolution XRD patterns (Figure S2.1-S2.4). The absorption coefficient of a $Cu_{10}Zn_2Sb_4Se_{13}$ thin-film is shown in Figure 2.3 and exhibits a similar strong onset property as the corresponding sulfide-based compound, $Cu_{10}Zn_2Sb_4S_{13}$. However the band gap is shifted to a lower energy of $E_G \sim 1.36$ eV, within the desired range of a solar absorber. The nature of the band gap for $Cu_{10}Zn_2Sb_4Se_{13}$ has to be considered, i.e., whether it is direct or indirect. The density-functional theory (DFT) calculation shows that the energy difference between direct and indirect gap is small ($\Delta = 0.18$ eV, Figure S2.10), which is consistent with a plot

of α vs. $E^{1/2}$ (direct) and α vs. E^2 (indirect) for a $Cu_{10}Zn_2Sb_4Se_{13}$ thin-film (Δ = 0.02 eV Figure S2.5). This small difference implies that the absorption coefficient begins to rise rapidly at an energy near the band gap, dominanted by the direct gap, even though the optical band gap is indirect. Further DFT calculations are required to confirm the band gap type in tetrahedrite compounds. Note that the absorption coefficient for the $Cu_{10}Zn_2Sb_4Se_{13}$ thin-film shown in Figure 2.3 exhibits a high sub-band gap absorption ($\alpha \sim 2 \times 10^4$ cm^{-1}) due to a non-optimized process deposition. Alternative deposition techniques are currently being pursued to reduce the level of sub-band gap absorption.

2.5 Simulations of Tetrahedrites as an Absorber layer

To demonstrate that tetrahedrite compounds can provide for a high-efficiency TFSC, device simulations were carried out via SCAPS[22] using measured properties of $Cu_{10}Zn_2Sb_4Se_{13}$ from Table 2.1 and Figure 2.3 as inputs to the model. The device configuration, shown in the inset of Figure 2.4a, is an n-p-p^+ heterojunction TFSC, where the tetrahedrite layer forms the p-type absorber with a carrier concentration of $N_A = 2 \times 10^{16}$ cm^{-3}. An n-p-p^+ heterojunction is a drift cell configuration,[23] since the n and the p^+ layers provide a strong built-in electric field across the absorber layer, sweeping photogenerated carriers towards their respective contacts. A 100 nm p^+ layer is included beneath the absorber to create an electron reflector via a small (0.2 eV) conduction band offset at the p-p^+ interface, providing a barrier and preventing electrons from recombining at the back surface. The properties of the p^+ layer are assumed to be identical to the absorber layer, with an increased carrier concentration to 2×10^{18} cm^{-3}. The n-type layer is comprised of a 25 nm CdS layer below a 500 nm SnO_2 layer, similar to a CdTe-based TFSC configuration. The strong

onset of absorption in $Cu_{10}Zn_2Sb_4Se_{13}$ along with the absorption coefficient reaching a maximum value of 3 x 10^5 cm^{-1} at E_G + 0.6 eV suggests that the thickness of the absorber layer can be reduced to < 1 μm without significant loss in performance.

To understand the minimum thickness required for a $Cu_{10}Zn_2Sb_4Se_{13}$-based TFSC, the simulated variation in device efficiency as a function of absorber layer thickness is shown in Figure 2.4a. Efficiencies greater than 20% can be achieved even when the absorber layer thickness is reduced to 300 nm, confirming that a material exhibiting a strong onset coupled with high absorption can provide for an ultra-thin high efficiency TFSC. For thicknesses greater than 500 nm, the efficiency reduces slightly before saturating, since the absorber thickness is greater than an absorption length. As a result, carriers have to diffuse to the edge of the space charge region before getting swept by the drift field, increasing recombination and resulting in a decreased device efficiency. This thickness requirement for $Cu_{10}Zn_2Sb_4Se_{13}$ is considerably lower than that for c-Si (20 ~ 260 μm)[24,25], CIGS (2 μm)[26] or a CdTe (2 ~ 5 μm)[27,28] based solar cell, and is similar to an amorphous silicon-based TFSC, however, with improved electrical and optical properties.

The minority carrier lifetime (τ) is inversely proportional to concentration of midgap defect states in a material[4,29] and can limit the photoconversion efficiency in a TFSC. Figure 2.4b shows the variation in device efficiency as a function of midgap defect density for a 300-nm thick $Cu_{10}Zn_2Sb_4Se_{13}$ absorber layer in a TFSC. Efficiencies greater than 20 % can be achieved with a trap density of 10^{14} cm^{-3} (τ = 1 ns), while a large trap density of 10^{16} cm^{-3} (τ = 0.01 ns) still provides for a 13 % efficient TFSC. This indicates that the $Cu_{10}Zn_2Sb_4Se_{13}$ absorber layer need not require intensive process optimization in order to provide a high quality, defect-free material. In other words, the drift cell configuration employed means that the $Cu_{10}Zn_2Sb_4Se_{13}$ absorber layer is relatively defect tolerant. The simulated current-voltage characteristics of a 300 nm $Cu_{10}Zn_2Sb_4Se_{13}$-

based TFSC is shown in Figure S2.8. A plot of the simulated quantum efficiency, which approaches 90 % between 530–780 nm is shown in Figure S2.9, validating $Cu_{10}Zn_2Sb_4Se_{13}$ as a high-performance TFSC absorber material.

2.6 Experimental Section

Powder synthesis: polycrystalline tetrahedrite samples were synthesized by a standard solid-state reaction. The starting materials were commercial reagent grade Mn, Cu, Zn, In, Sb, S, and Se having purity > 99.95 % from Alfa Aesar. Stoichiometric quantities of reactants were mixed and heated at 450 ^oC for 3 weeks in evacuated sealed fused-silica tubes, and subsequently cooled to room temperature after switching off the furnace. Additional regrinding and reheating were carried to produce single-phase samples. The resulting polycrystalline powders were crushed and molded into pellets of diameter ~ 0.5 in. These were sintered at 450 ^oC for 24 hrs to maximize the density of pellets (~ 85 %), for analysis of physical properties.

Thin-film deposition: thin-films of the sulfide-based tetrahedrites were fabricated using electron-beam (EB) evaporation of the constituent layers (transition metal sulfide/Cu/Sb_2S_3) at room temperature onto a fused silica substrate and were subsequently annealed in a CS_2 environment in a tube furnace at 295 ^oC for 30 mins. $Cu_{10}Zn_2Sb_4Se_{13}$ thin films were similarly fabricated by using EB evaporation of the constituent layers having an additional Se layer (ZnSe/Cu/Se/Sb_2Se_3). The sample was subsequently annealed in an evacuated sealed fused-silica tube at 295 ^oC for 30 mins.

X-ray characterization: the crystal phase of tetrahedrite samples in the annealed powders and deposited thin films as characterized with a Rigaku Ultima IV diffractometer with a 0.02 rad slit Cu Kα radiation (λ = 1.5418 Å). Data were collected between 10 and 100^o at a step size of 0.02^o

and a dwell time of 1 s at each step. X-ray diffraction patterns were compared with ICSD[30] and ICDD-PDF[31] files by using PDXL software suite[32].

Optical and electrical characterization: optical transmission and reflection measurements were performed by using a spectrometer equipped with an Ocean Optics HR4000 UV-Vis detector and a balanced deuterium/tungsten halogen source (DH-2000-BAL). For diffuse reflectance measurements, MgO power (99.95 %, Cerac) was used as a white reference. Room temperature resistivity and Hall mobility were collected in the van der Pauw geometry with a LakeShore 7504 measurement system. Majority carrier type was determined from Seebeck measurements on a custom-built system by applying a 3 K temperature gradient to the sample.

Theoretical calculation: The first principles calculation of $Cu_{12}Sb_4S_{13}$ presented here was carried out by using Wien2K suite[33] with VASP code[34] and PAW potentials[35]. The electronic degree of freedom are described within DFT by the generalized gradient approximation (GGA) with the value of the Hubbard U parameters (for Cu, U = 6 eV; for others, U = 0 eV), and the atomic positions are fully relaxed by HSE06 while lattice parameters were kept fixed to our experimental data. For the exchange-correlation functional, the PW91 parametrization[36] for accurate total energy calculations was used with a Γ-centered 3×3×3 *k*-point grid.

Device simulation: The device configuration used in SCAPS is similar to a CdTe-based TFSC and is comprised of the following layers: back contact/ p^+-$Cu_{10}Zn_2Sb_4Se_{13}$/ p-$Cu_{10}Zn_2Sb_4Se_{13}$/ n-Cds/ n-ZnO/ front contact. The p-$Cu_{10}Zn_2Sb_4Se_{13}$ absorber layer is assumed to have a carrier concentration of $2x10^{16}$ cm^{-3}, while the p^+ layer has a carrier concentration of $2x10^{18}$ cm^{-3} and otherwise the same properties as the absorber layer. The work function values of the front and back contact are 4.1 and 5.0 eV, respectively. The electron/hole mobility value of the $Cu_{10}Zn_2Sb_4Se_{13}$ layers is assumed to be 50/14 $cm^2V^{-1}s^{-1}$ and trap mediated (Shockley-Read-Hall)

recombination is assumed to be the dominant recombination mechanism. The current-voltage characteristic is simulated between 0 and 1 V and the quantum efficiency is simulated between 300 and 1200 nm.

2.7 Conclusions

In conclusion, we have successfully designed new artificial mineral tetrahedrites exhibiting strong and abrupt absorption based on the following design paradigm: isolated Sb in a s^2p^0 low valence electronic configuration can provide for narrower bands near the CBM and VBM. These narrow bands enhance the JDOS giving rise to a material with a strong absorption coefficient and a rapid onset of absorption. One tetrahedrite material in particular, $Cu_{10}Zn_2Sb_4Se_{13}$ has a band gap of E_G = 1.36 eV, shows a maximum absorption coefficient value of 3 x 10^5 cm^{-1} at E_G + 0.6 eV and is predicted to exhibit high photoconversion efficiencies (> 20 %) in a TFSC with a thickness of only 300 nm. This inherent strong absorption property coupled with tunable band gaps and fabrication temperatures less than 300 °C makes the tetrahedrite family of materials especially attractive for photovoltaic absorbers. $Cu_{10}Zn_2Sb_4Se_{13}$ is only one example of a large class of possible tetrahedrite compounds. Exploring related materials may provide further opportunities to develop a new generation of single-junction and tandem TFSCs with ultra-thin absorber layers.

References

[1] M. A. Green, K. Emery, Y. Hishikawa, W. Warta, E. D. Dunlop, *Prog. Photovoltaics Res. Appl.* **2012**, *20*, 12.

[2] H. Yuen, in *Opt. Sol. Energy*, Austin, **2011**.

[3] P. Jackson, D. Hariskos, E. Lotter, S. Paetel, R. Wuerz, R. Menner, W. Wiltraud, M. Powalla, *Prog. Photovoltaics Res. Appl.* **2011**, *19*, 894.

[4] S. M. Sze, K. K. Ng, *Physics of Semiconductor Devices*, Wiley, Chichester, **2007**.

[5] W. Shockley, H. J. Queisser, *J. Appl. Phys.* **1961**, *32*, 510.

[6] L. Yu, A. Zunger, *Phys. Rev. Lett.* **2012**, *108*, 068701.

[7] L. Yu, R. S. Kokenyesi, D. a. Keszler, A. Zunger, *Adv. Energy Mater.* **2013**, *3*, 43.

[8] Maria Telkes, *Am. Mineral.* **1950**, *35*, 536.

[9] X. Lu, D. T. Morelli, Y. Xia, F. Zhou, V. Ozolins, H. Chi, X. Zhou, C. Uher, *Adv. Energy Mater.* **2013**, *3*, 342.

[10] J. Heo, G. Laurita, S. Muir, M. a. Subramanian, D. a. Keszler, *Chem. Mater.* **2014**, *26*, 2047.

[11] K. Suekuni, K. Tsuruta, M. Kunii, H. Nishiate, E. Nishibori, S. Maki, M. Ohta, A. Yamamoto, M. Koyano, *J. Appl. Phys.* **2013**, *113*, 043712.

[12] F. Machatschki, *Nor. Geol. Tidsskr.* **1928**, *10*, 23.

[13] Bernhardt J. Wuensch, *Zeitschrift fur Krist.* **1964**, *119*, 437.

[14] J. Garin, E. Parthé, *Acta Crystallogr. Sect. B Struct. Crystallogr. Cryst. Chem.* **1972**, *28*, 3672.

[15] M. F. Razmara, C. M. B. Henderson, R. A. D. Pattrick, J. M. Charnock, *Mineral. Mag.* **1997**, *61*, 79.

[16] A. Walsh, D. J. Payne, R. G. Egdell, G. W. Watson, *Chem. Soc. Rev.* **2011**, *40*, 4455.

[17] A. Pfitzner, M. Evain, V. Petricek, *Acta Crystallogr. Sect. B Struct. Sci.* **1997**, *53*, 337.

[18] E. J. W. Verwey, H. P. W., *Physica* **1941**, *8*, 979.

[19] R. A. D. Pattrick, *Mineral. Mag.* **1983**, *47*, 441.

[20] N. E. Johnson, J. R. Craig, J. D. Rimstidt, *Am. Mineral.* **1988**, *73*, 389.

[21] A. Luque, S. Hegedus, *Handbook of Photovoltaic Science and Engineering*, Wiley, USA, **2011**.

[22] M. Burgelman, P. Nollet, S. Degrave, *Thin Solid Films* **2000**, *361-362*, 527.

[23] J. a. Spies, R. Schafer, J. F. Wager, P. Hersh, H. a. S. Platt, D. a. Keszler, G. Schneider, R. Kykyneshi, J. Tate, X. Liu, a. D. Compaan, W. N. Shafarman, *Sol. Energy Mater. Sol. Cells* **2009**, *93*, 1296.

[24] T. Tiedje, E. Yablonovitch, G. D. Cody, B. G. Brooks, *IEEE Trans. Electron Devices* **1984**, *31*, 711.

[25] J. Zhao, A. Wang, M. A. Green, F. Ferrazza, *Appl. Phys. Lett.* **1998**, *73*, 1991.

[26] I. Repins, S. Glynn, J. Duenow, T. J. Coutts, W. Metzger, M. A. Contreras, San Diego, **2009**, p. 7409.

[27] X. Wu, *Sol. Energy* **2004**, *77*, 803.

[28] R. Scheer, H.-W. Schock, *Chalcogenide Photovoltaics: Physics, Technologies, and Thin Film Devices*, Wiley-VCH, Wienheim, **2011**.

[29] A. L. Fahrenbruch, R. H. Bube, *Fundamentals of Solar Cells: Photovoltaic Solar Energy Conversion*, Academic, UK, **1983**.

[30] F. H. Allen, G. Bergerhoff, I. Brown, **2013**.

[31] International Centre for Diffraction Data, **2013**.

[32] Rigakuo, **2010**.

[33] P. Blaha, K. Schwarz, G. K. H. Madsen, D. Kvasnicka, J. Luitz, **2001**.

[34] P. E. Blöchl, *Phys. Rev. B* **1994**, *50*, 17953.

[35] G. Kresse, J. Furthmüller, *Phys. Rev. B* **1996**, *54*, 11169.

[36] J. P. Perdew, J. A. Chevary, S. H. Vosoko, K. A. Jackson, M. R. Pederson, D. J. Singh, F. Carlos, *Phys. Rev. B* **1992**, *46*, 6671.

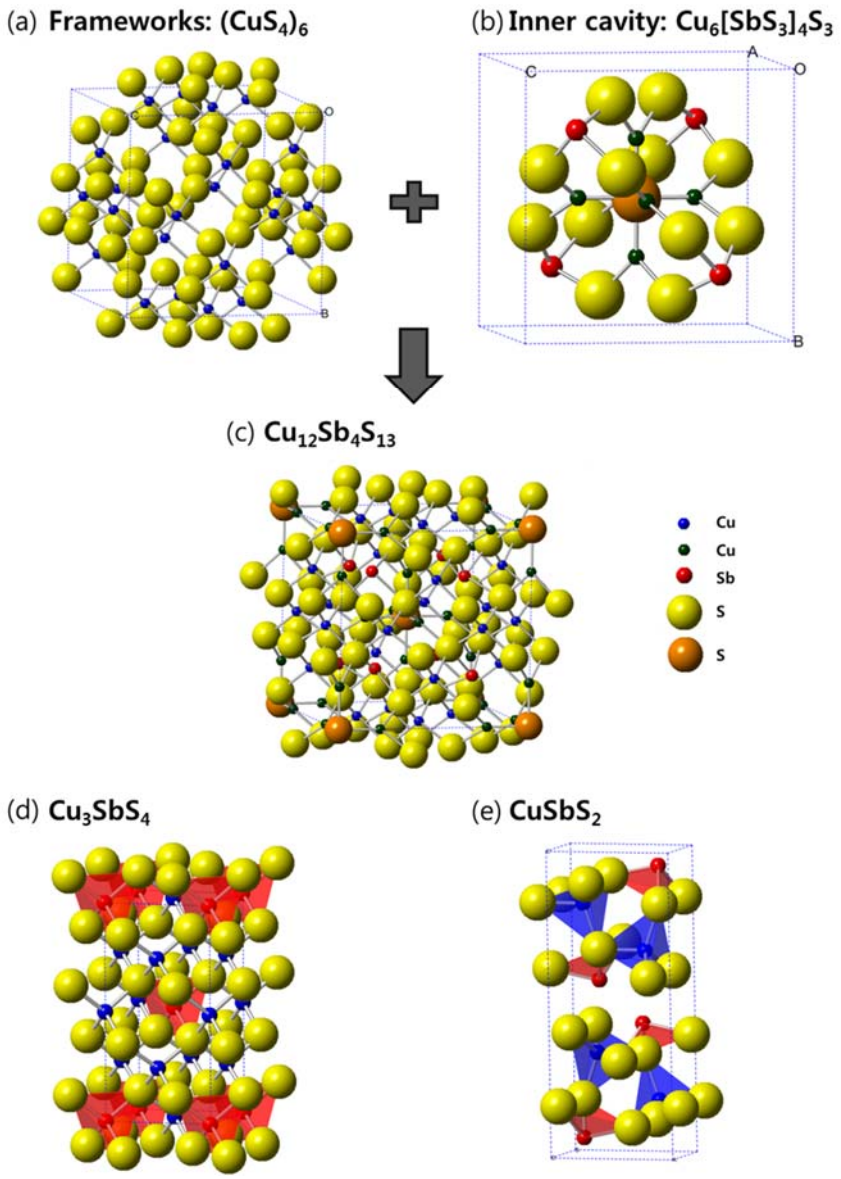

Figure 2.1 (a) Crystal structure of a) CuS_4 (normal tetrahedral) corner-connected tetrahedral framework, (b) a cavity polyhedron composed of CuS_3 (trigonal planar) and SbS_3 (trigonal pyramid), and (c) the unit cell of the tetrahedrite, $Cu_{12}Sb_4S_{13}$. Crystal structures of (d) Cu_3SbS_4 and (e) $CuSbS_2$. All directions are slightly off plane (100).

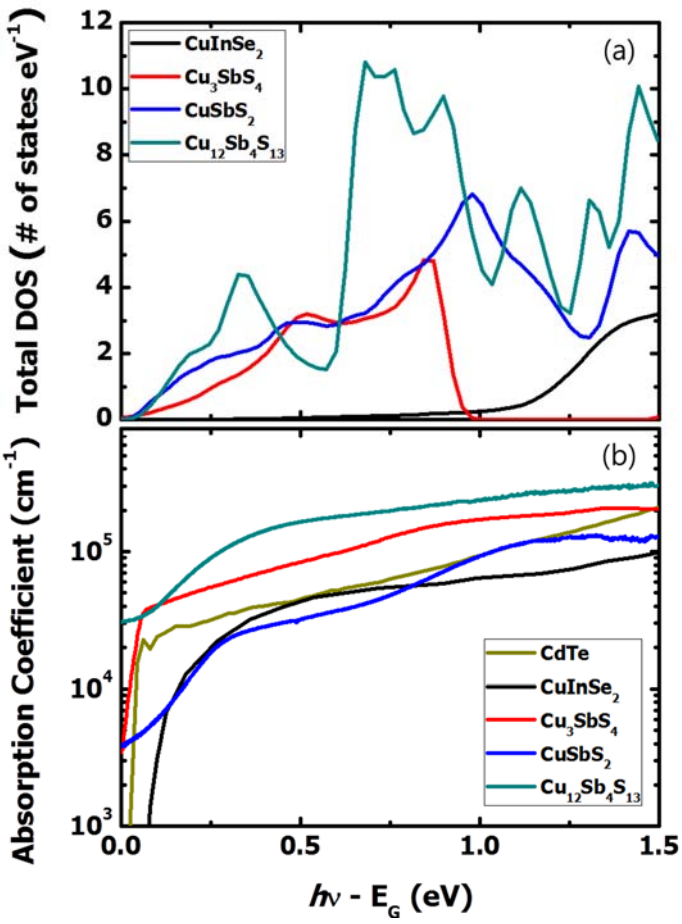

Figure 2.2 (a) The estimated density of states (DOS) of $CuInSe_2$, Cu_3SbS_4, $CuSbS_2$, and $Cu_{12}Sb_4S_{13}$ from density-functional theory (DFT) calculations, which are comparable with previous publications. [7,17] (b) Optical absorption spectra for Cu_3SbS_4, $CuSbS_2$, $Cu_{12}Sb_4S_{13}$, $CuInSe_2$, and CdTe. Minimum band gaps (E_G) are aligned at E = 0 in order to show the absorption onset properties near E_G.

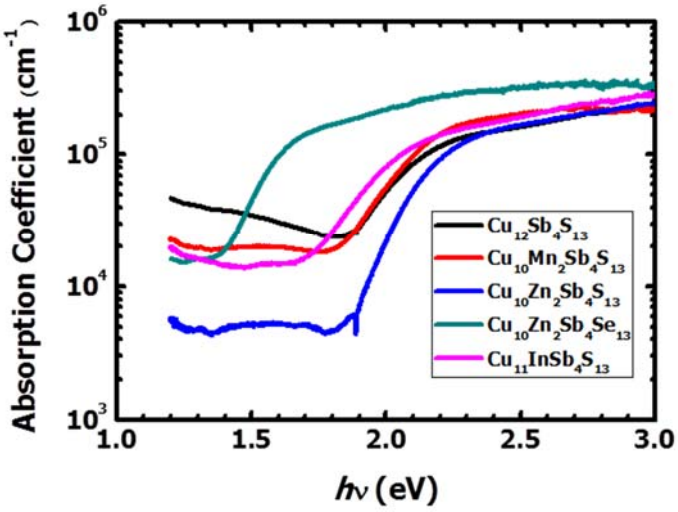

Figure 2.3 Experimental absorption coefficients for ~ 200 nm thick $Cu_{12}Sb_4S_{13}$, $Cu_{10}Mn_2Sb_4S_{13}$, $Cu_{10}Zn_2Sb_4S_{13}$, $Cu_{11}InSb_4S_{13}$, and $Cu_{10}Zn_2Sb_4Se_{13}$ thin-films. The optical band gaps extracted from our experiments are 1.83, 1.83, 1.82, 1.70, and 1.40 eV, respectively.

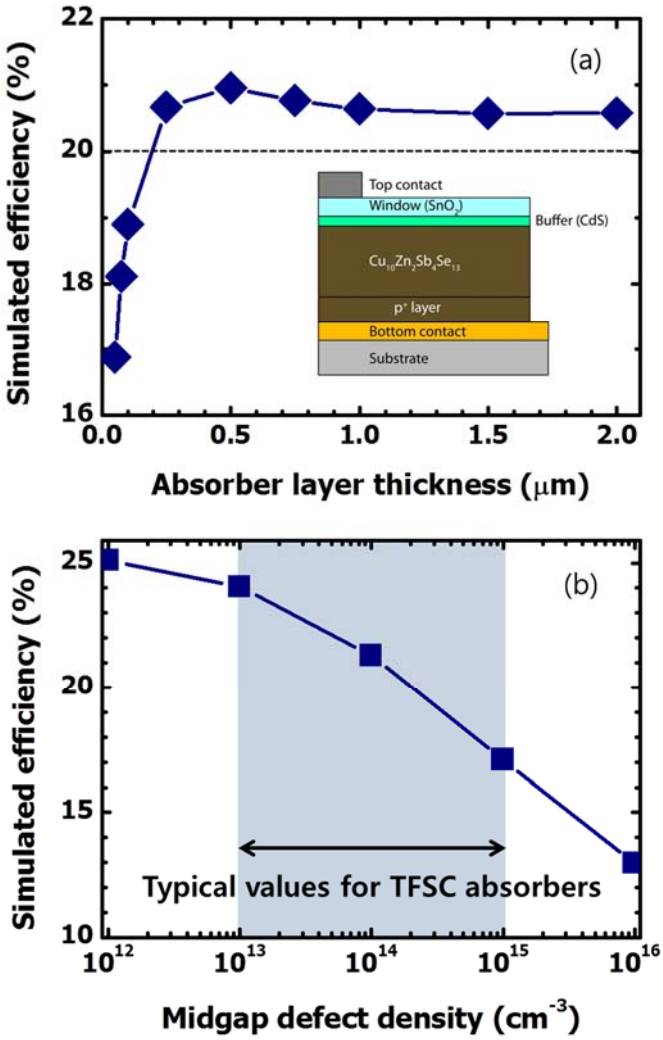

Figure 2.4 Variation of the efficiency of the TFSC as a function of (a) absorber layer thickness and (b) defect density for a $Cu_{10}Zn_2Sb_4Se_{13}$ based TFSC. Efficiencies greater than 20 % can be achieved with the absorber layer thickness reduced to 300 nm, while efficiencies of 13% can be obtained even when the defect density is as high as 10^{16} cm^{-3}. The inset in (a) is the device configuration used in the simulations.

Table 2.1 Optical and electrical properties of select tetrahedrite compounds from experimental measurements.

Composition		Band Gap E_G [eV]	Resistivity ρ [Ω cm]	Seebeck coefficient S [μV/K]
$Cu_{12}Sb_4S_{13}$	Powder	-	0.004	75
	Thin film	1.83	0.001	60
$Cu_{10}Mn_2Sb_4S_{13}$	Powder	1.81	0.46	250
	Thin film	1.83	9.5	180
$Cu_{10}Zn_2Sb_4S_{13}$	Powder	1.80	5.5	312
	Thin film	1.82	10.0	180
$Cu_{11}In_1Sb_4S_{13}$	Powder	1.65	8.5	330
	Thin film	1.70	4.0	120
$Cu_{10}Zn_2Sb_4Se_{13}$	Powder	1.36	12.0	300
	Thin film	1.36	10.0	280

Supporting Information for

Design Meets Nature: New Tetrahedrite Solar Absorbers

Jaeseok Heo[1], Ram Ravichandran[2], John F. Wager[2], and Douglas A. Keszler[1]

[1]Department of Chemistry, Oregon State University, Corvallis, Oregon 97331-4003 USA

[2]School of Electrical Engineering and Computer Science, Oregon State University, Corvallis, Oregon 97331-5501 USA

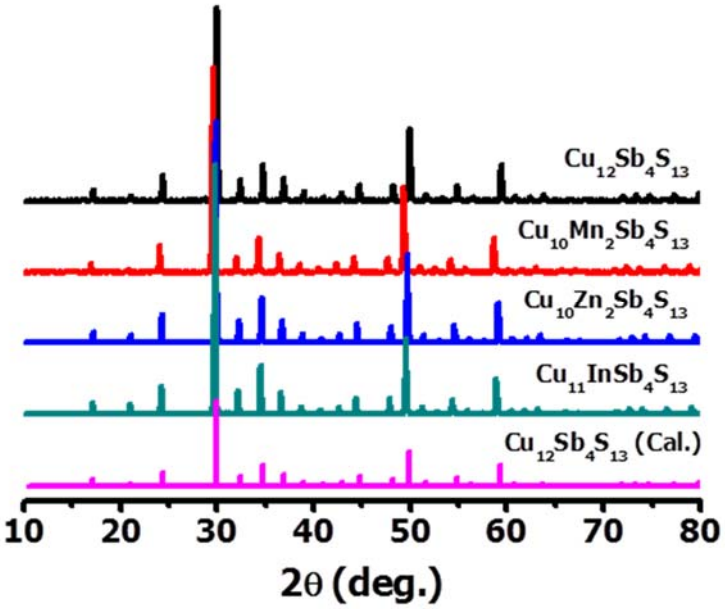

Figure S2.1 X-ray spectra of synthetic tetrahedrite powder samples $Cu_{12}Sb_4S_{13}$, $Cu_{10}Mn_2Sb_4S_{13}$, $Cu_{10}Zn_2Sb_4S_{13}$, and $Cu_{11}InSb_4S_{13}$. X-ray diffraction patterns were compared with simulated X-ray patterns of PDF card no. 00-024-1318 for $Cu_{12}Sb_4S_{13}$.

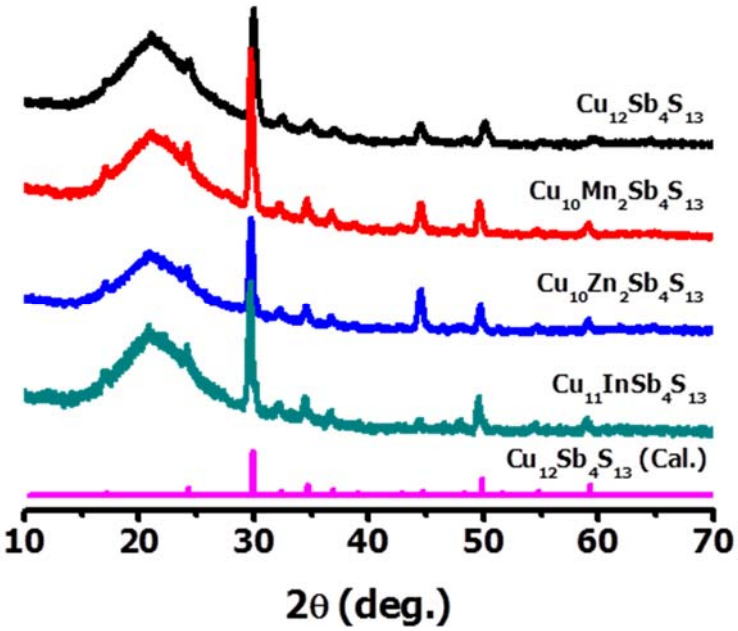

Figure S2.2 X-ray spectra of tetrahedrite thin films $Cu_{12}Sb_4S_{13}$, $Cu_{10}Mn_2Sb_4S_{13}$, $Cu_{10}Zn_2Sb_4S_{13}$, and $Cu_{11}InSb_4S_{13}$. X-ray diffraction patterns were compared with simulated X-ray patterns of PDF card no. 00-024-1318 for $Cu_{12}Sb_4S_{13}$.

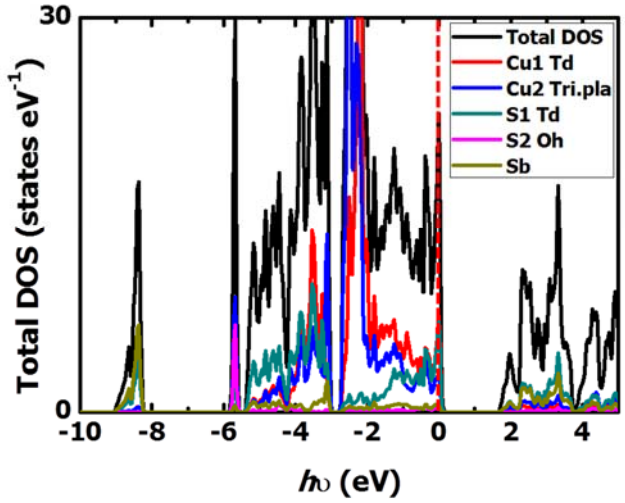

Figure S2.3 Calculated total density of states for $Cu_{12}Sb_4S_{13}$. The position of the Fermi level is denoted by a red dashed line and cuts the valence band.

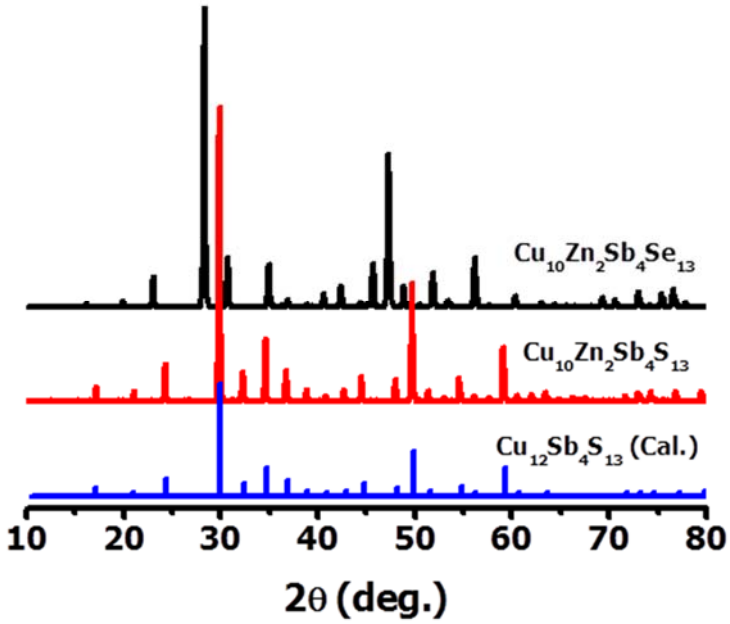

Figure S2.4 X-ray spectra of synthetic tetrahedrite powder samples $Cu_{10}Zn_2Sb_4S_{13}$ and $Cu_{10}Zn_2Sb_4Se_{13}$. X-ray diffraction patterns were compared with simulated X-ray patterns of PDF card no. 00-024-1318 for $Cu_{12}Sb_4S_{13}$.

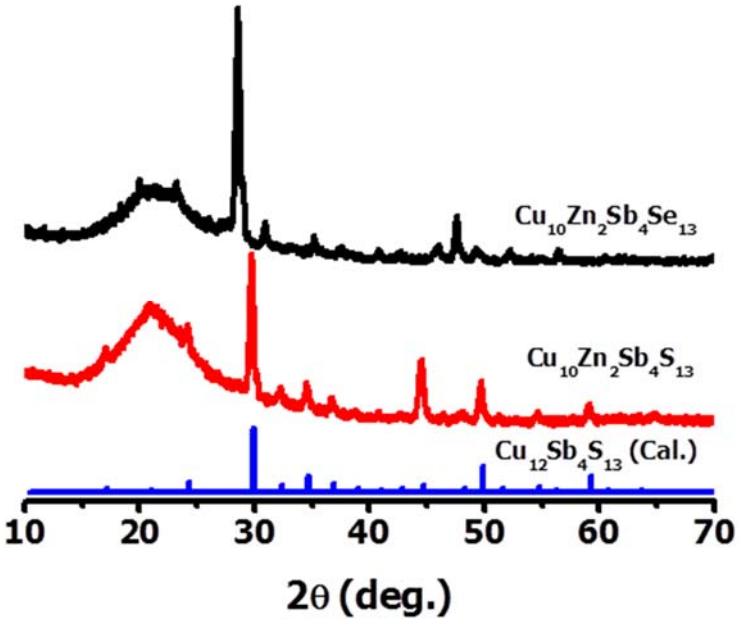

Figure S2.5 X-ray spectra of tetrahedrite thin films $Cu_{10}Zn_2Sb_4S_{13}$ and $Cu_{10}Zn_2Sb_4Se_{13}$. X-ray diffraction patterns were compared with simulated X-ray patterns of PDF card no. 00-024-1318 for $Cu_{12}Sb_4S_{13}$.

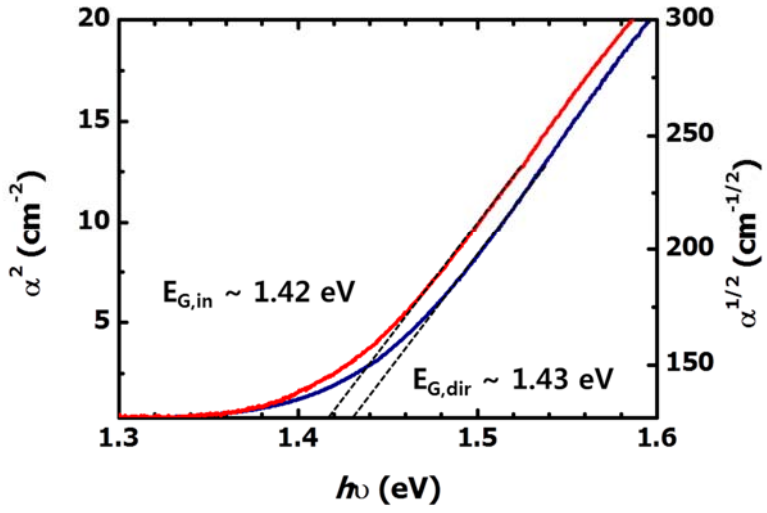

Figure S2.6 The plots of $\alpha^{1/2}$ vs. E (indirect) and α^2 vs. E (direct) of a $Cu_{10}Zn_2Sb_4Se_{13}$ thin film. It is seen that the energy difference between direct and indirect gap is very small (< 0.02 eV).

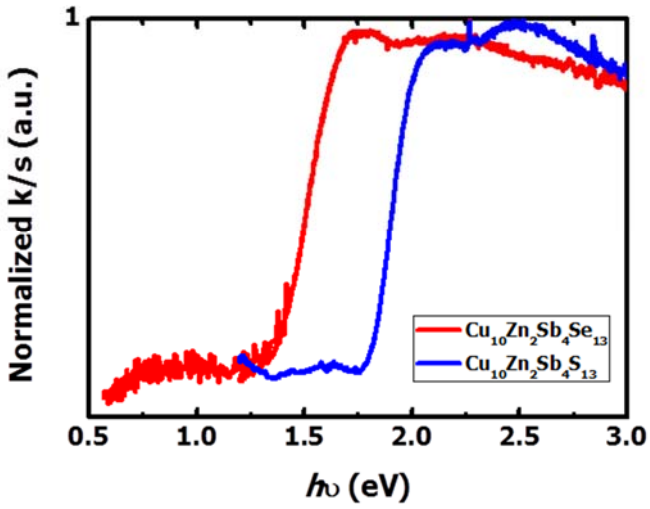

Figure S2.7 Measured diffuse reflectance of bulk $Cu_{10}Zn_2Sb_4Se_{13}$ and $Cu_{10}Zn_2Sb_4S_{13}$, indicating a band gap of 1.36 and 1.8 eV, respectively.

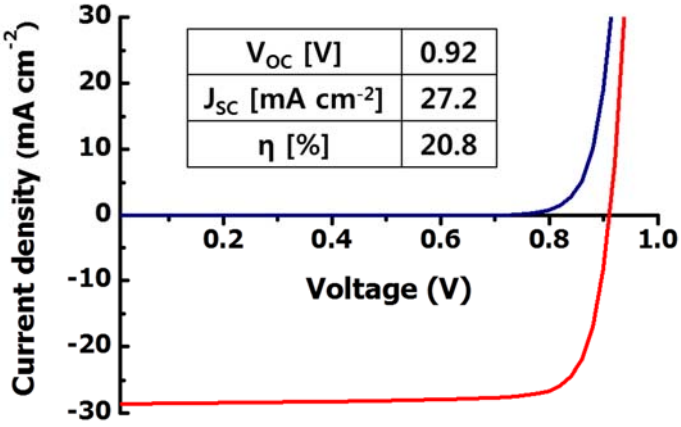

Figure S2.8 Current-voltage characteristics of a TFSC with a 300 nm thick $Cu_{10}Zn_2Sb_4Se_{13}$ absorber layer and a minority carrier lifetime of 1 ns. The V_{oc} is 0.92 V, J_{sc} is 27.2 mA/cm^2 providing for a 20.8 % efficient TFSC.

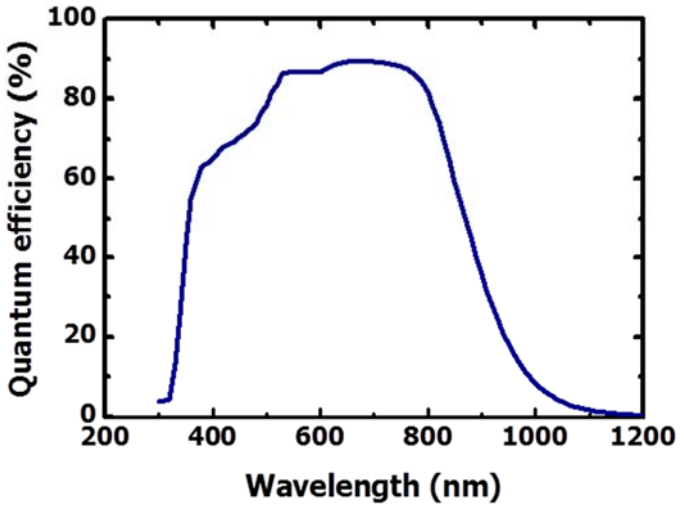

Figure S2.9 Quantum efficiency (QE) characteristics of a TFSC with a 300 nm thick $Cu_{10}Zn_2Sb_4Se_{13}$ absorber layer. The QE approaches 90% between 530 – 780 nm.

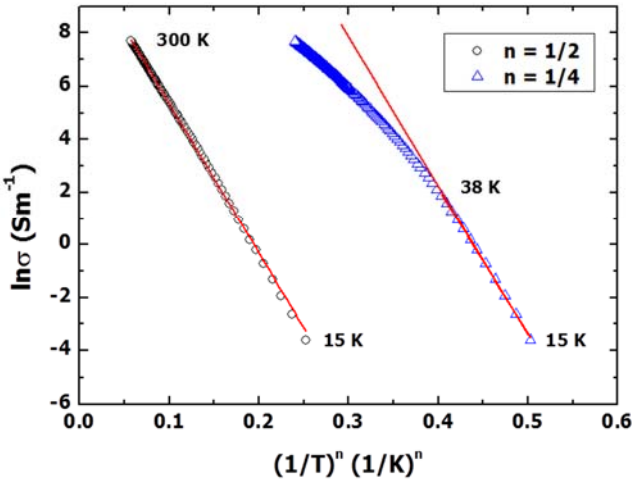

Figure S2.10 ln(σ) versus $(1/T)^n$ for $Cu_{10}Mn_2Sb_4S_{13}$ shows the straight-line fit by Equation (2) for $n = 1/2$ ($R^2 = 0.999$), but fit with $n = 1/4$ ($R^2 = 0.982$) deviated from the linearity after 38 K.

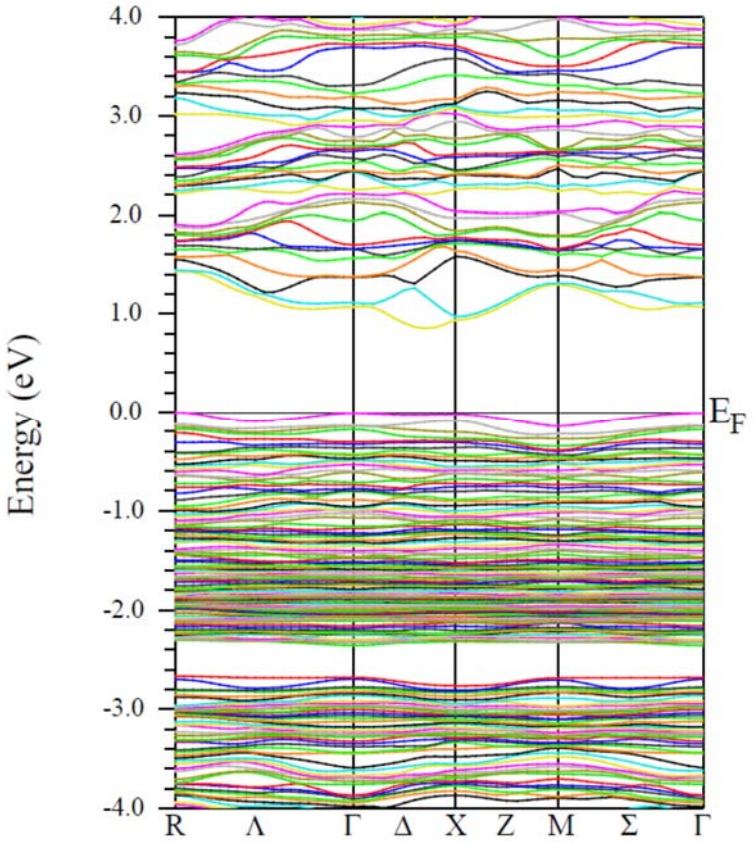

Figure S2.11 (a) Band structure and (b) DOS of $Cu_{10}Zn_2Sb_4Se_{13}$. A small difference, $\Delta = 0.18$ eV, exists between the indirect gap and the dipole-allowed direct gap. This small difference implies that the absorption coefficient begins to rise rapidly at an energy near the band gap, dominanted by the direct gap, even though the optical band gap is indirect.

Chapter 3

Enhanced Thermoelectric Performance of Synthetic Tetrahedrites

Jaeseok Heo, Geneva Laurita, Sean Muir, Mas A. Subramanian, and Douglas A. Keszler

Department of Chemistry, Oregon State University, Corvallis, Oregon 97331-4003 USA

Published in *Chemistry of Materials* **2014**, *26*, 2047

3.1 Introduction

The thermoelectric (TE) effect is the direct conversion of a thermal gradient to an electric potential and vice-versa. Materials exhibiting this effect have many commercial, industrial, and military applications, as they can be used to build electric generators or heating and cooling systems with no moving parts. The usefulness of TE materials and devices is primarily limited by their efficiencies. The conversion efficiency is often stated as the dimensionless figure of merit, ZT, where T is the absolute temperature and Z is related to material properties.[1–7] Attempts to maximize ZT must meet the materials-design challenge of simultaneously achieving low thermal conductivity (κ), high electrical conductivity (σ), and high thermopower (S), *cf.*, Equation (3.1).

$$ZT = (S^2\sigma T)/\kappa \qquad (3.1)$$

κ, σ, and S are commonly correlated properties. High electrical conductivity, for example, is often associated with low thermopower and/or high thermal conductivity. Such correlations depress ZT. As a result, the ZT of commercial TE materials has remained near 1. There is, however, no theoretical upper limit to ZT, which has encouraged the formulation of a number of design strategies for realizing enhanced performance.

One intriguing approach to uncoupling κ, σ, and S correlations and depressing κ is to identify materials where thermal properties are modulated by the presence of electronically isolated structural features. In this way, materials can simultaneously exhibit the high electronic conductivity of a crystalline framework and the low thermal conductivity of a glass-like substance. This concept has been examined in disordered alloys, materials containing nanoscale inhomogeneities, and crystals with complex structures containing "rattler" atoms, e.g., clathrates and skutterudites.[8–10] Clathrate and skutterudite frameworks form electrically conductive pathways, while rattlers within the frameworks are presumed to enhance phonon scattering and lower lat-

tice thermal conductivity. For example, complex skutterudite compositions have been reported to exhibit ZT > 1.[10]

The tetrahedrite structure, typified by $Cu_{12}Sb_4S_{13}$, captures these features.[11] The compounds of this family crystallize in a cubic structure (space group *I-43m*)[12] (Figure 3.1a). The chemical formula can be rationalized from a crystal-structure point of view as $Cu_6Cu_6[SbS_3]_4S$, wherein half of the Cu atoms occupy four-coordinate, distorted tetrahedral sites and half occupy three-coordinate triangular sites. The CuS_4 units are condensed via vertex sharing into a highly defective framework derived from sphalerite. Cavities in the framework are occupied by the large structural unit of CuS_3 and SbS_3 groups shown in Figure 3.1b. This description is important because it clearly illustrates two features relevant to thermoelectric performance of tetrahedrite. The sphalerite-like framework of CuS_4 groups plays a major role in affecting electrical properties,[13] i.e., the power factor ($PF = S^2\sigma$), while the isolated structure of Figure 1b, containing the asymmetrically coordinated Cu and Sb atoms, is a key for realizing small κ. In recent studies,[6,14–16] it has been demonstrated that tetrahedrite derivatives containing Fe, Ni, and Zn exhibit thermoelectric performance (maximum ZT = 0.95 at 700 K) comparable to conventional materials. To expand on these findings, we report results on additional members of the tetrahedrite family, demonstrating that ZT > 1 can be achieved at modest temperatures.

3.2 Experimental Section

Powder Synthesis. Polycrystalline samples were synthesized by standard solid-state reaction of appropriate combinations of the elements Mn, Fe, Co, Ni, Cu, Zn, Sb, and S (purity > 99.95 %; Alfa Aesar). Stoichiometric mixtures were ground and then heated at 450 ℃ for 3 weeks in evacuated, sealed fused-silica tubes. The samples were intermittently ground to produce single-

phase samples. For analysis of physical properties, the resulting polycrystalline powders were molded into pellets of ~ 0.5-in diameter and then were sintered at 450 ℃ under 10 MPa pressure to produce sample densities ≥ 85 % of theoretical values.

X-ray Characterization. X-ray data were collected on a Rigaku Ultima IV diffractometer with a 0.02 rad slit and Cu Kα radiation (λ = 1.5418 Å). Scans were made between 10 and 100 ^{o} 2θ at a step size of 0.02 ^{o} 2θ and a dwell time of 1 s at each step. The resulting diffractions patterns were compared to ICSD and ICDD-PDF files to verify formation of the desired compound (Figure S3.1).

Thermal and Electrical Characterization. Electrical and thermal properties (S, σ, and κ) were measured from 325 to 575 K. The S and σ data were collected on an ULVAC-RIKO ZEM-3 under a helium atmosphere (instrumental error = 5 %). Thermal diffusivity (α) was measured on a Netzsch LFA 457 Micro Flash under flowing N_2 (instrumental error = 10 %, Figure S3.2). Upon cooling, the properties were measured again at 325 K to ensure the samples did not degrade or display hysteresis. Specific heat capacity (C_p) was measured for $Cu_{12}Sb_4S_{13}$ and $Cu_{10}Mn_2Sb_4S_{13}$ with a Netzsch DSC-200PC differential scanning calorimeter (Figure S3.3). C_p = 0.45 J g^{-1} K^{-1} was found for each sample. This value was used for all samples to calculate κ from the relationship $\kappa = C_p \times \alpha \times d$, where *d* is the sample bulk density.

Low Temperature Magnetism and Electrical Conductivity. Low-temperature magnetic and electrical measurements (Figure S4) were made by using a Quantum Design Physical Properties Measurement System (PPMS). Magnetic susceptibility data were obtained by using a 0.5-Tesla field and warming the sample from 5 to 300 K. Variable-temperature (5 - 300 K) electrical-conductivity data were collected by using the four-point probe method (Figure S3.5 – S3.9).

Optical Characterization. Diffuse reflectance measurements were made by using a spectrometer equipped with an Ocean Optics HR400 UV-Vis/IR detector and a balanced deuterium/tungsten halogen source (DH-2000-BAL) (Figure S10 & S11). MgO powder (99.95 %, Cerac) was used as a white reflectance standard.

3.3 Results and discussion

Electrical Properties. The variation of PF, σ, and S over the temperature range 300 – 600 K is illustrated for $Cu_{12}Sb_4S_{13}$ and $Cu_{10}TM_2Sb_4S_{13}$ (TM = Mn, Fe, Co, Ni, Zn) in Figure 2. Electrical conductivities (σ) vary by approximately four orders of magnitude, while thermopowers (S) differ by a factor of six. As a result of its high σ relative to those of $Cu_{10}TM_2Sb_4S_{13}$, $Cu_{12}Sb_4S_{13}$ has the highest PF, i.e., > 2x of the TM derivatives. To consider the origin of the elevated conductivity and PF in $Cu_{12}Sb_4S_{13}$, we need to account for the oxidation states of the Cu atoms. The triangular planar CuS_3 sites are characterized only by d^{10} Cu^{1+}, while the tetrahedral CuS_4 sites are formally occupied by a mixture of Cu^{1+} and Cu^{2+}.[13,17] This mixed valency produces a high hole concentration in the CuS_4 framework, accounting for the relatively high *p*-type conductivity of $Cu_{12}Sb_4S_{13}$. This model is consistent with the results of density-functional theory (DFT) calculations.[13] Interestingly, we have confirmed that $Cu_{12}Sb_4S_{13}$ undergoes a metal-semiconductor transition upon cooling to approximately 90 K (Figure S5).[14] Low-temperature structural characterization is needed to determine if this resistivity change is accompanied by a significant structural distortion.

The Zn derivative $Cu_{10}Zn_2Sb_4S_{13}$ exhibits conductivity much lower than that of $Cu_{12}Sb_4S_{13}$. Zn substitution represents an isovalent replacement of Zn^{2+} for Cu^{2+}, but Zn^{2+} has a d^{10} electron configuration rather than the d^9 configuration of Cu^{2+}. In principle, the additional electrons from

Zn^{2+} should lead to a filled valence band, converting $Cu_{12}Sb_4S_{13}$ to an instrinsic semiconductor with a smaller conductivity. We note, however, that the temperature dependence of the conductivity in $Cu_{10}Zn_2Sb_4S_{13}$ (Figure S3.7) can be linearly fit to Equation (2)

$$\ln \sigma \propto (1/T)^n \quad (1/4 \leq n \leq 1) \qquad (3.2)$$

with n = 1/2 over the entire temperature range (15 – 300 K). This result indicates that impurity ion scattering and Anderson localization[18–21] likely play roles in setting the magnitude of σ. Additionally, the fit with n= 1/2 is commonly associated with electron-electron interactions contributing to the temperature dependence of the conductivity.[20,21] Fe substitution produces a similar level of σ. It has been reported that Fe at the stoichiometry $Cu_{10}Fe_2Sb_4S_{13}$ is formally 2+.[22] Fe^{2+} also replaces Cu^{2+} in an isolvalent manner, but it is contributing six d electrons through its d^6 configuration. Unlike Zn^{2+} substitution, there is no band filling. Hence, the low σ must be related to impurity-induced localization and the propensity of Fe^{2+} toward oxidation and hole trapping. The Mn, Co, and Ni derivatives exhibit intermediate conductivities. Values are likely reduced relative to $Cu_{12}Sb_4S_{13}$ via impurity scattering, but they are less oxidizing and have a lower hole-trapping potential relative to Fe.

The thermopowers (S), shown in Figure 3.2c, are positive over the entire temperature range, indicating majority carriers are holes. S, ~ 74 μV K^{-1}, of $Cu_{12}Sb_4S_{13}$ is very small at 325 K. With Zn substitution, it increases by a factor > 3x to 253 μV K^{-1} at the same temperature. The increase in S is expected for conversion of a degenerate to intrinsic semiconductor through band filling. At 575 K, the order in S from lowest to highest comprises the derivatives Cu, (Fe, Ni), Mn, (Zn, Co), while the order in σ (Figure 3.2b) from lowest to highest is (Fe, Zn), Co, (Mn, Ni), and Cu. The two series are not cleanly inverted one relative to the other, rather the values vary with the

TM. This behavior is likely related to varying orbital composition near the band edges, band filling near E_F, and the propensity for impurity scattering.[23]

The electrical conductivity and the thermopower were used to calculate the power factor, which in all cases monotonically increases with temperature. Among the substituted tetrahedrites, the Mn derivative exhibits the highest PF, i.e., 2.28 μW cm^{-1} K^{-2} at 575 K. On substitution in the tetrahedrite structure, Mn adopts a high-spin, d^5 configuration, as confirmed by a low-temperature magnetic susceptibility measurement (μ_{eff} = 5.50 μ_B, Figure S3.4). From diffuse reflectance measurements, we find that this derivative exhibits a band gap near 1.8 eV, which is similar to that of the Zn analog (Figure S3.10). Gaps of comparable magnitude were not observed for any of materials containing Fe, Co, or Ni (Figure S3.11). Because wide band gaps limit thermal excitation of minority carriers across the gap, thermoelectric efficiency can be enhanced in wide-gap *vs.* narrow-gap semiconductors at elevated temperatures.[24] Hence, as expected, the Mn derivative exhibits an increase in S and PF as a function of temperature. These increases are aided by a relatively high electrical conductivity (Figure 3.2). In contrast, the small σ of $Cu_{10}Zn_2Sb_4S_{13}$ suppresses the temperature dependence of PF.

Thermal conductivity. As shown in Figure 3.3a, the thermal conductivity of $Cu_{12}Sb_4S_{13}$ is ~ 1.1 W m^{-1} K^{-1}, which is comparable to those of conventional thermoelectric materials, *cf.*, > 0.8 W m^{-1} K^{-1} for Bi_2Te_3 and PbTe.[4] The conductivity drops sharply on substitution of Cu with transition metals, leading to values < 0.3 W m^{-1} K^{-1} over the entire temperature range 325 – 575 K (Figure 3). These small conductivities are especially unusual for materials with light-mass elements such as copper and sulfur. They agree well with those of X. Lu and co-workers (Table S1),[13] and they are only slightly lower than those reported by K. Suekuni and co-workers (Table S1).[14,15] Thermal conductivity values can vary significantly, depending on sample preparation

and measurement technique.[24] For example, thermal-diffusivity values, derived from the laser-flash method, vary with sample density, unlike those from a conventional steady-state measurement.[3] The samples produced for this study should yield a reliable qualitative comparison of the series, since sample densities vary by < 3 %.

Thermal conductivity is determined by two factors: κ_{el} (electronic conductivity) arising from electrons or holes transporting heat and κ_L (lattice conductivity) arising from phonons carrying the energy. As seen from comparison of Figures 3a and 3b, κ_L is the main contributor to the total thermal conductivity. The TM substitutions severely depress σ (Figure 3.2), making κ_{el} an inconsequential contribution to κ. The origin of low κ in $Cu_{12}Sb_4S_{13}$ is most likely associated with its complex crystal structure and asymmetric coordination of Cu in triangular planar coordination and Sb in distorted trigonal pyramids. It is well known that atoms with asymmetric coordination lead to strong lattice anharmonicity[25] and phonon scattering. Such asymmetry has, for example, been invoked to account for the large lattice thermal resistance in solids containing cations with ns^2 electron configuration, e.g., Cu_3SbSe_3.[25,26] Also, from DFT calculations, X. Lu and coworkers have demonstrated that the cavity structural unit $Cu_6Sb_4S_{13}$ (Figure 3.1b) induces highly anharmonic behavior from random freezing of unstable phonons, resulting in strong intrinsic phonon scattering.[13] The measured heat capacity, 0.45 J g^{-1} K^{-1}, of the tetrahedrites is much smaller than the value, 1.3 J g^{-1} K^{-1}, that is calculated on the basis of the Dulong-Petit law,[27] which assumes solely harmonic oscillations. This difference may well be related to the vibrational anharmonicity in the tetrahedrites. In the TM-substituted materials, the thermal conductivity decreases by a factor of about three, covering a narrow range of 0.2 - 0.3 W m^{-1} K^{-1}. This reduction in κ_L is likely associated with additional phonon scattering derived from the random distribution of the TMs in the materials.

Figures of merit. The temperature dependence of ZT of each of the materials $Cu_{12}Sb_4S_{13}$ and $Cu_{10}TM_2Sb_4S_{13}$ is summarized in Figure 3.3c. ZT is flat for the Zn and Fe derivatives, while it rises significantly for the Mn- and Co-substituted samples on heating. κ is also flat for all of the TM materials across the measured temperature range, hence ZT primarily tracks with the temperature variation of PF (Figure 3.2a). The Mn derivative exhibits the highest ZT. This value derives from an intermediate value of S (Figure 3.2c) in combination with a relatively high electrical conductivity (Figure 3.2a).

Because Mn substitution produced the highest, we have examined in greater detail the effects of adjusting the Mn concentration in the series $Cu_{12-x}Mn_xSb_4S_{13}$; x = 0, 0.5, 1, 1.5, 2. A ZT = 1.13 (Table S3.2) was achieved at a modest temperature (575 K) by tuning x to 1 (Figure 3.4a). The ZT value of $Cu_{11}MnSb_4S_{13}$ at 575 K is approximately 2x higher than those previously reported for other substituted tetrahedrites, e.g., $Cu_{1.6}Zn_{0.4}Sb_4S_{13}$ (ZT = 0.55)[13] and $Cu_{10.5}Ni_{1.5}Sb_4S_{13}$ (ZT = 0.5)[14]. As ZT commonly rises with temperature, even higher ZT values could well be realized.[14,15]

In the Fe-substituted materials $Cu_{12-x}Fe_xSb_4S_{13}$, the maximum ZT (0.95 at 700 K) has been reported to occur at x = 0.5. The Fe and Mn materials exhibit two key differences: (i) at equivalent levels of substitution, the Mn compounds exhibit the higher ZT, and (ii) for x = 1.5 – 2, ZT for the Fe materials drops more significantly than the Mn compositions. These observations can be attributed to the aforementioned change of the ratio Fe^{3+}/Fe^{2+} with increasing Fe concentration, which contrasts with the persistent 2+ oxidation state of Mn at all levels of substitution.

Optimization of ZT involves maximizing the ratio PF/κ. As shown in Figures 3.4b and 3.4c, κ for the Mn compounds at 575 K falls dramatically from x = 0 to x = 0.5, while at the same time, PF increases due to the increase of S. For x > 0.5, σ drops and S escalates, while κ remains nearly

constant. (See Figures S3.12 and S3.13 for temperature dependence of PF and κ.) The resulting dependence of ZT on Mn concentration somewhat mirrors the classical variation of ZT with carrier concentration (*n*), where *n* is proportional to σ and $S^{2/3}$.[5,28] A more comprehensive treatment, however, is required here, as contributions from impurity scattering and band-edge orbital compositions affect the observed behavior.[24]

3.4 Conclusion

The synthetic tetrahedrite $Cu_{12}Sb_4S_{13}$ exhibits a modest thermal conductivity that can be uniformly depressed by a factor of three or more by substituting the transition metals Mn, Fe, Co, Ni, or Zn for Cu. In contrast, electrical transport properties are found to be highly sensitive to the identity of the transition metal. In the case of Mn, PF can be tuned to realize an enhanced ZT = 1.13 at 575 K, reaching levels competitive with those of conventional thermoelectric materials such as Bi_2Te_3 and PbTe. While the current ZT is now the highest among reported tetrahedrites, still higher values should be realized at temperatures above 575 K. $Cu_{11}MnSb_4S_{13}$ is only one example within a large class of possible tetrahedrite compositions. Examination of these materials in greater detail should afford additional insights about the contributions of electronic and thermal properties to their TE performance, while also potentially enabling opportunities for development of high-efficiency thermoelectric devices.

References

[1] C. B. Vining, *Nat. Mater.* **2009**, *8*, 83.

[2] R. R. Heikes, R. W. Ure, *Thermoelectricity: Science and Engineering*, Interscience, New York, **1961**.

[3] H. J. Goldsmid, *Introduction to Thermoelectricity*, Springer, **2010**.

[4] D. M. Rowe, *CRC Handbook of Thermoelectrics*, CRC Press, **1995**.

[5] G. J. Snyder, E. S. Toberer, *Nat. Mater.* **2008**, *7*, 105.

[6] T. M. Tritt, *Recent Trends in Thermoelectric Materials Research*, Academic, **2001**.

[7] T. M. Tritt, M. A. Subramanian, *MRS Bull.* **2006**, *31*, 188.

[8] G. S. Nolas, J. Poon, M. Kanatzidis, *MRS Bull.* **2006**, *31*, 199.

[9] N. P. Blake, S. Latturner, J. D. Bryan, G. D. Stucky, H. Metiu, *J. Chem. Phys.* **2001**, *115*, 8060.

[10] X. Shi, J. Yang, J. R. Salvador, M. Chi, J. Y. Cho, H. Wang, S. Bai, J. Yang, W. Zhang, L. Chen, *J. Am. Chem. Soc.* **2011**, 7837.

[11] M. Telkes, *Am. Mineral.* **1950**, *35*, 536.

[12] Bernhardt J. Wuensch, *Zeitschrift fur Krist.* **1964**, *119*, 437.

[13] X. Lu, D. T. Morelli, Y. Xia, F. Zhou, V. Ozolins, H. Chi, X. Zhou, C. Uher, *Adv. Energy Mater.* **2013**, *3*, 342.

[14] K. Suekuni, K. Tsuruta, T. Ariga, M. Koyano, *Appl. Phys. Express* **2012**, *5*, 051201.

[15] K. Suekuni, K. Tsuruta, M. Kunii, H. Nishiate, E. Nishibori, S. Maki, M. Ohta, A. Yamamoto, M. Koyano, *J. Appl. Phys.* **2013**, *113*, 043712.

[16] C. H. L. Goodman, *J. Phys. Chem. Solids* **1958**, *6*, 305.

[17] A. Pfitzner, M. Evain, V. Petricek, *Acta Crystallogr. Sect. B Struct. Sci.* **1997**, *53*, 337.

[18] G. Mahan, B. Sales, J. Sharp, *Phys. Today* **1997**, *50*, 42.

[19] F. J. Di Salvo, J. A. Wilson, J. V. Waszczak, *Phys. Rev. Lett.* **1976**, *36*, 885.

[20] N. Mott, M. Pepper, S. Pollitt, R. H. Wallis, C. J. Adkins, *Proc. R. Soc. A Mathmatical Phys. Eng. Sci.* **1975**, *345*, 169.

[21] P. W. Anderson, *Phys. Rev.* **1958**, *109*, 1492.

[22] E. Mackovicky, K. Forcher, W. Lottermoser, G. Amthauer, *Miner. Pet.* **1990**, *43*, 73.

[23] I. M. Tsidil'kovskiĭ, *Sov. Phys. Uspekhi* **1992**, *35*, 85.

[24] Y. Pei, H. Wang, G. J. Snyder, *Adv. Mater.* **2012**, *24*, 6125.

[25] E. J. Skoug, D. T. Morelli, *Phys. Rev. Lett.* **2011**, *107*, 235901.

[26] Y. Zhang, E. Skoug, J. Cain, V. Ozoliņš, D. Morelli, C. Wolverton, *Phys. Rev. B Condens. Matter* **2012**, *85*, 054306.

[27] A.-T. Petit, P.-L. Dulong, *Ann. Chim. Phys.* **1819**, *10*, 395.

[28] M. Cutler, J. F. Leavy, R. L. Fitzpatrick, *Phys. Rev.* **1964**, *133*, A1143.

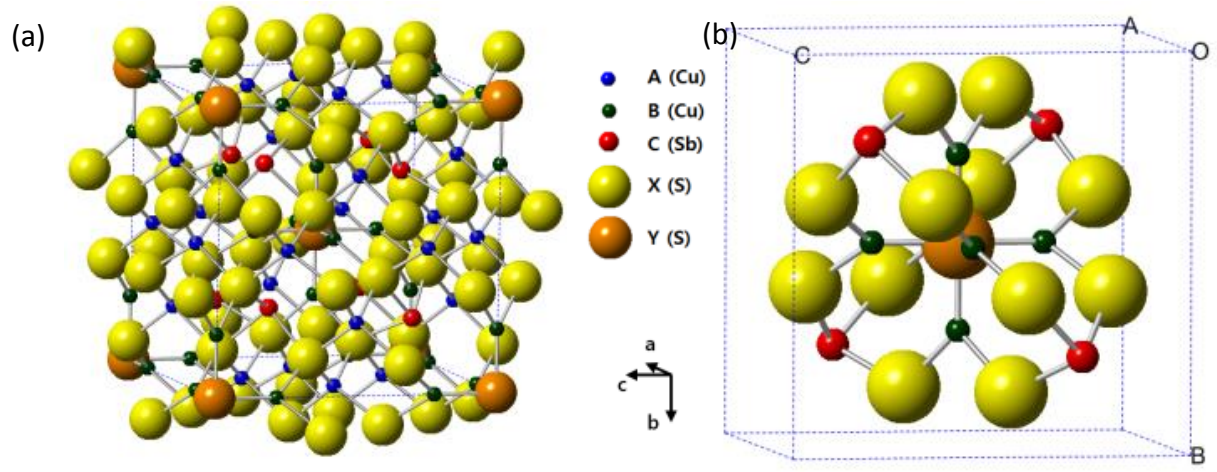

Figure 3.1 (a) Crystal structure of the tetrahedrite, $Cu_{12}Sb_4S_{13}$ and (b) a cavity polyhedron composed of CuS_3 and SbS_3 groups.

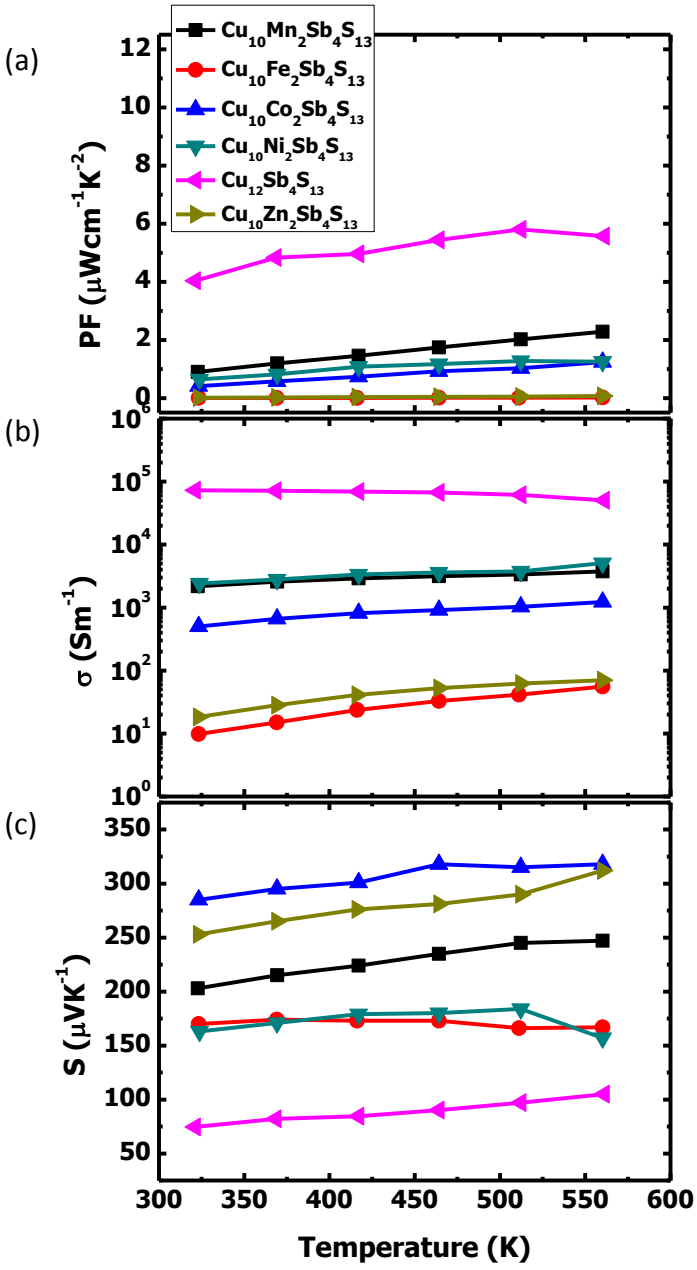

Figure 3.2 Temperature dependences of (a) power factor (PF), (b) electrical conductivity (σ), and (c) thermopower (S) for $Cu_{10}TM_2Sb_4S_{13}$ (TM = Mn, Fe, Co, Ni, Cu, Zn).

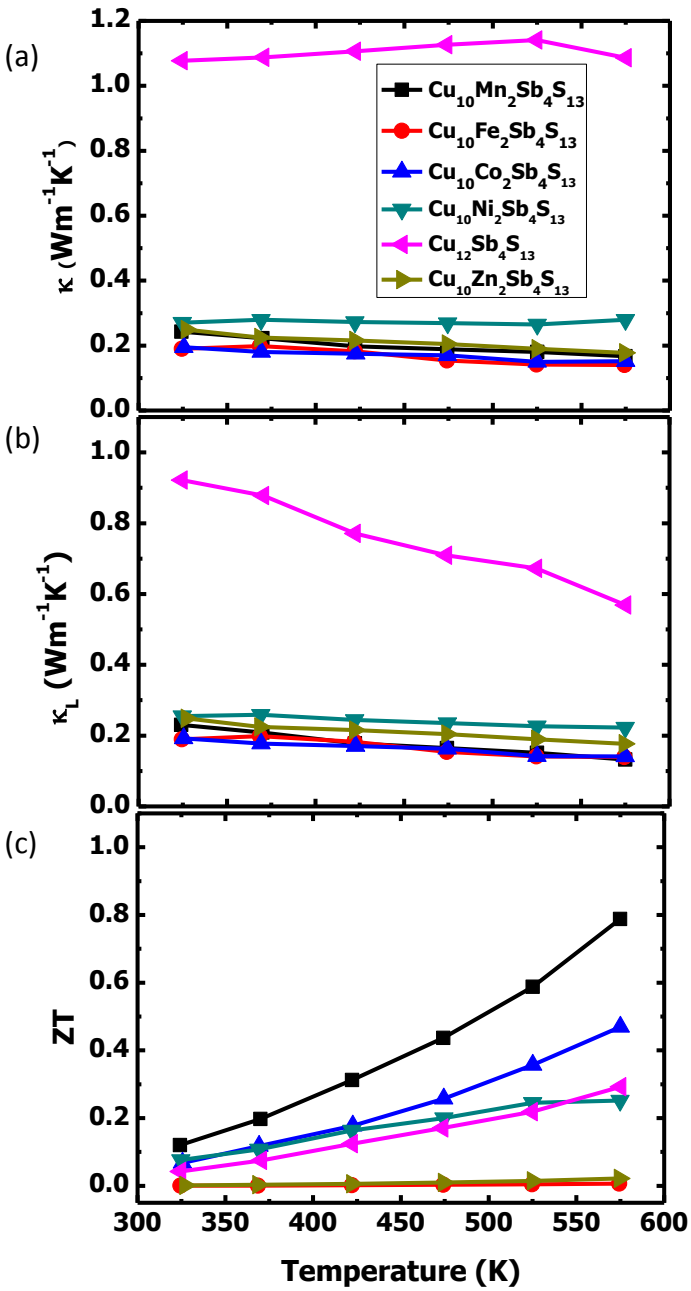

Figure 3.3 Variation with temperature of (a) total thermal conductivity (κ), (b) lattice thermal conductivity (κ_L), and (c) thermoelectric figure of merit ZT for $Cu_{10}TM_2Sb_4S_{13}$ (TM = Mn, Fe, Co, Ni, Cu, Zn).

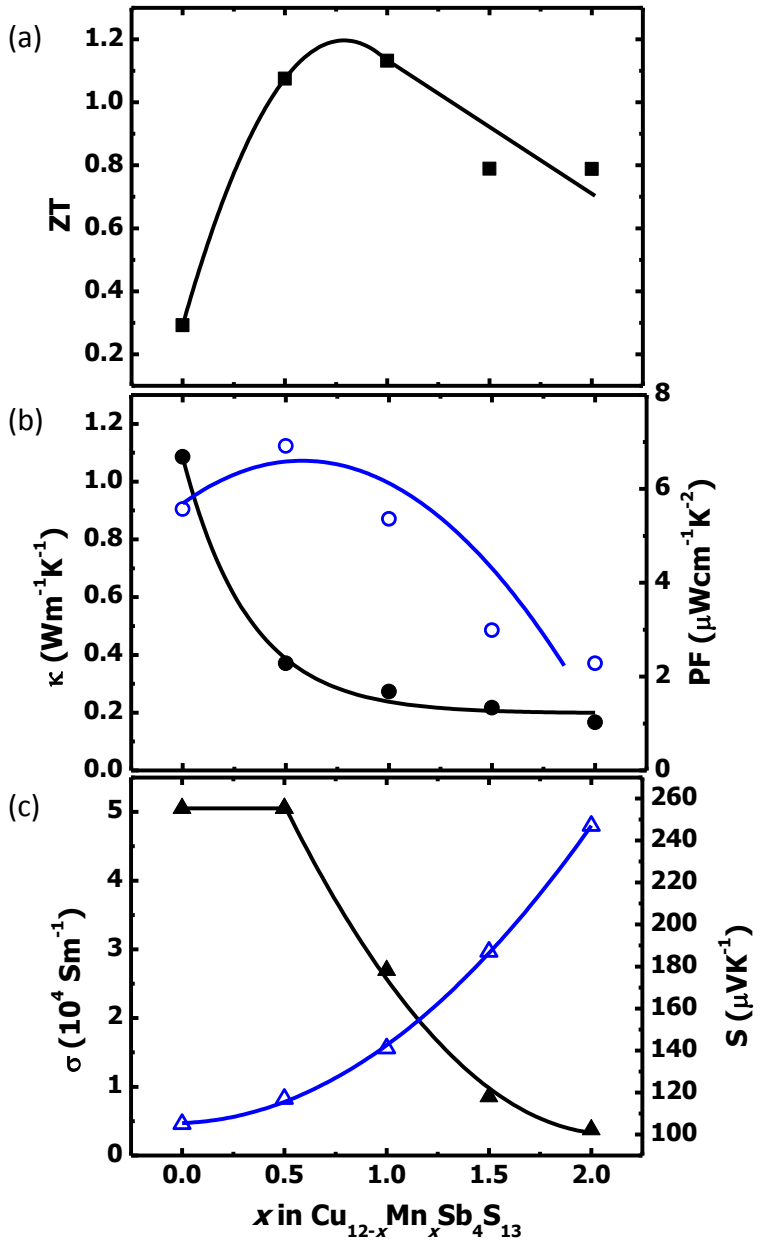

Figure 3.4 (a) Thermoelectric figure of merit ZT (filled square), (b) thermal conductivity (κ, filled circle), power factor (PF, open circle), (c) electrical conductivity electrical conductivity (σ, filled triangle), and thermopower (S, open triangle) as a function of Mn concentration in $Cu_{12-x}Mn_xSb_4S_{13}$ ($0 \leq x \leq 2$) at 575 K.

Supporting Information for

Enhanced Thermoelectric Performance of Synthetic Tetrahedrites

Jaeseok Heo, Geneva Laurita, Sean Muir, Mas A. Subramanian, and Douglas A. Keszler

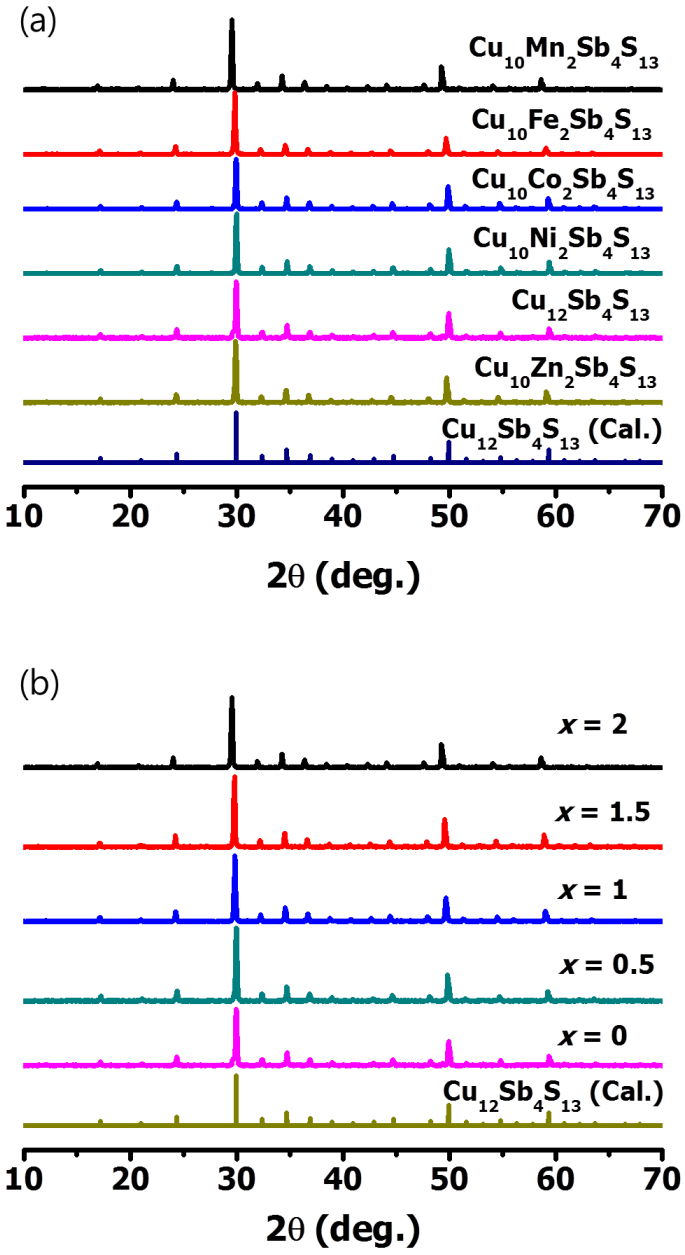

Figure S3.1 X-ray spectra of synthetic tetrahedrite powder samples (a) $Cu_{12}Sb_4S_{13}$ and $Cu_{10}TM_2Sb_4S_{13}$ (TM = Mn, Fe, Co, Ni, Zn), and (b) $Cu_{12-x}Mn_xSb_4S_{13}$ ($0 \leq x \leq 2$). X-ray diffraction pattern were compared with simulated X-ray patterns of PDF card no. 00-024-1318.

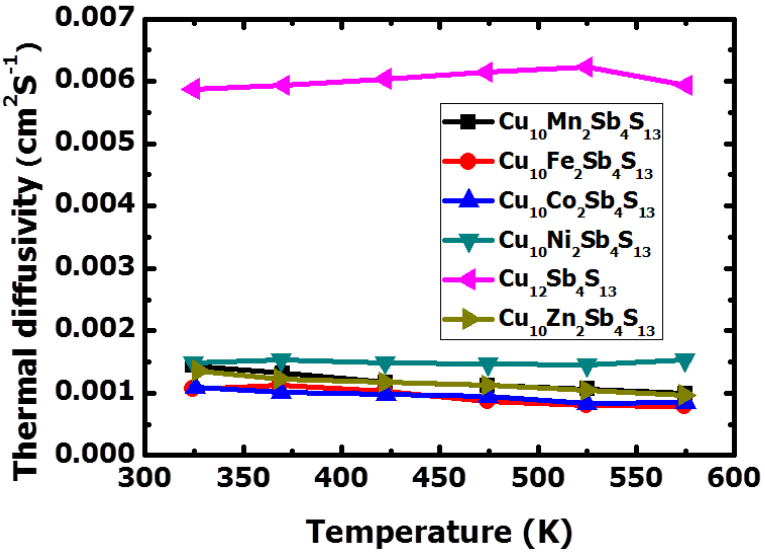

Figure S3.2 Thermal diffusivity of synthetic tetrahedrite powder samples $Cu_{12}Sb_4S_{13}$ and $Cu_{10}TM_2Sb_4S_{13}$ (TM = Mn, Fe, Co, Ni, Zn).

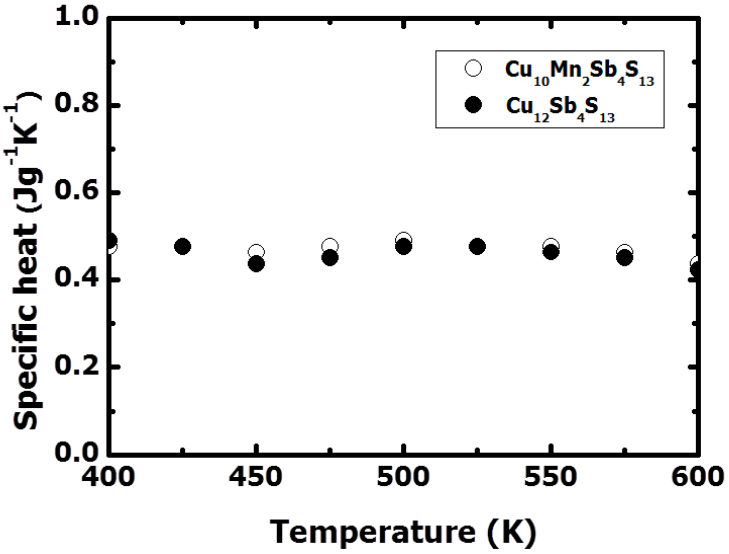

Figure S3.3 Specific heat capacity (C_p) of synthetic tetrahedrite powder samples $Cu_{12}Sb_4S_{13}$ (filled) and $Cu_{10}Mn_2Sb_4S_{13}$ (open). Both samples showed difference of no more than 1 %, and the average value, 0.45 $Jg^{-2}K^{-1}$, was applied for calculation of κ in other tetrahedrite compounds.

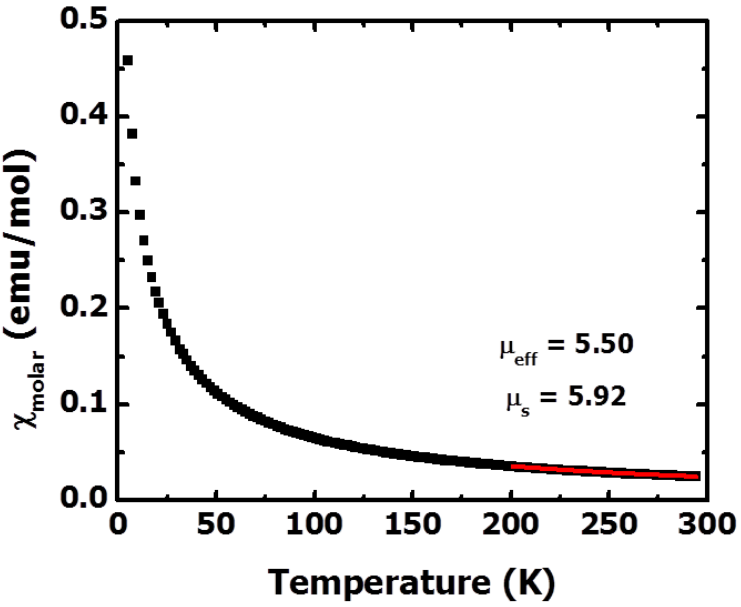

Figure S3.4 Zero field cooled molar (ZFC) molar magnetic susceptibility of synthetic tetrahedrite powder sample $Cu_{10}Mn_2Sb_4S_{13}$. The paramagnetic effective magnetic moment and fitting parameters for the Curie-Weiss equation ($\chi_{molar} = C/(T-\Theta)$) are shown inset.

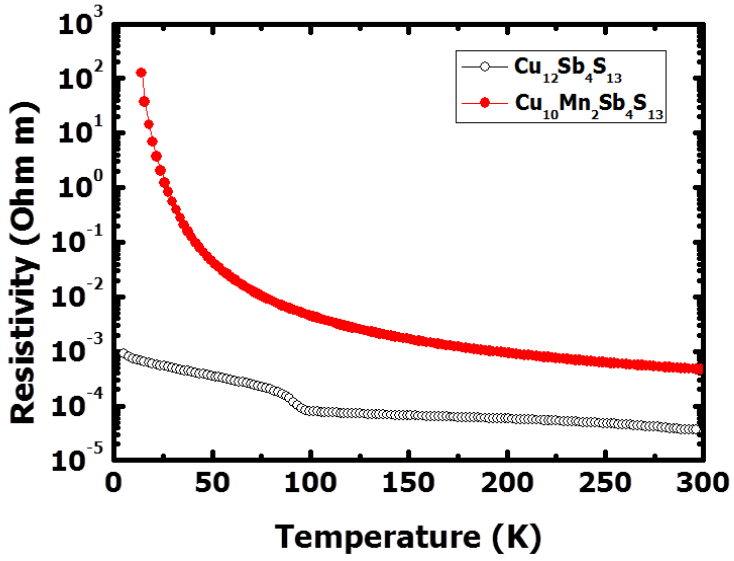

Figure S3.1 Low temperature resistivity of synthetic tetrahedrite powder samples $Cu_{12}Sb_4S_{13}$ (open) and $Cu_{10}Mn_2Sb_4S_{13}$ (filled). At 90 K $Cu_{12}Sb_4S_{13}$ undergoes a sudden change in resistivity while $Cu_{10}Mn_2Sb_4S_{13}$ behaves as a conventional non-degenerate semiconductor.

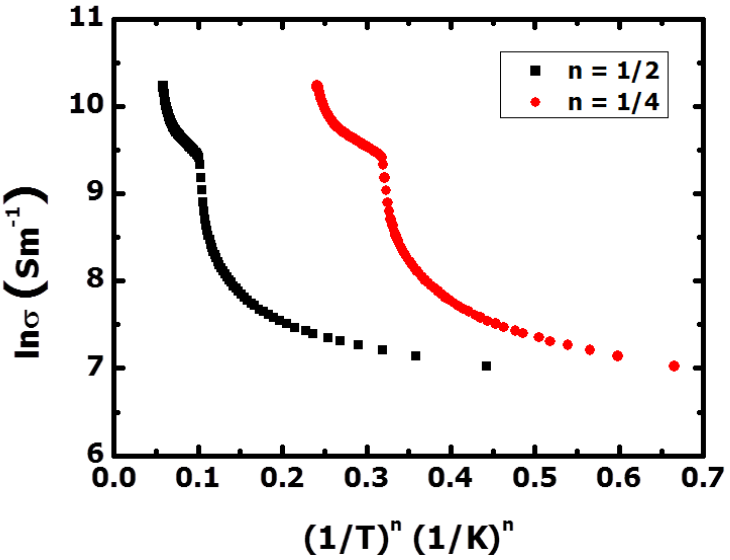

Figure S3.6 ln(σ) versus $(1/T)^n$ for $Cu_{12}Sb_4S_{13}$ does not show the straight-line fit by Equation (3.2) for both n = 1/2 and 1/4.

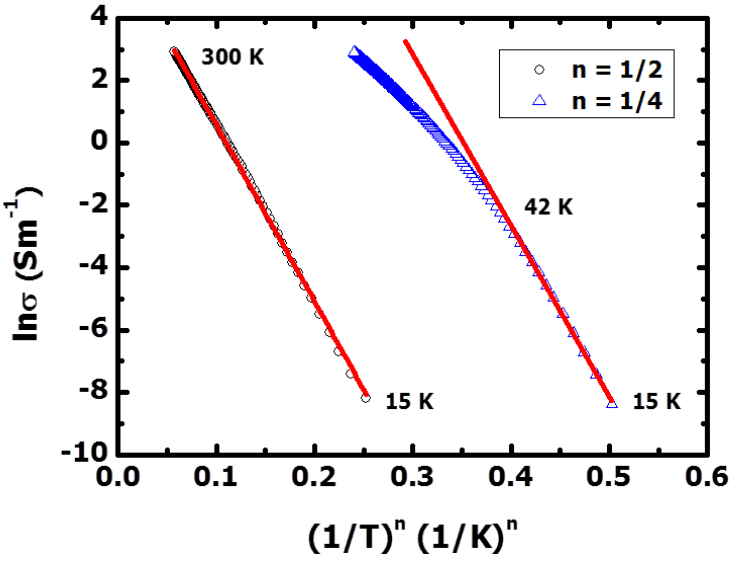

Figure S3.7 ln(σ) versus (1/T)n for $Cu_{10}Zn_2Sb_4S_{13}$ shows the straight-line fit by Equation (3.2) for n = 1/2 (R^2 = 0.999), but fit with n = 1/4 (R^2 = 0.982) deviated from the linearity after 42 K.

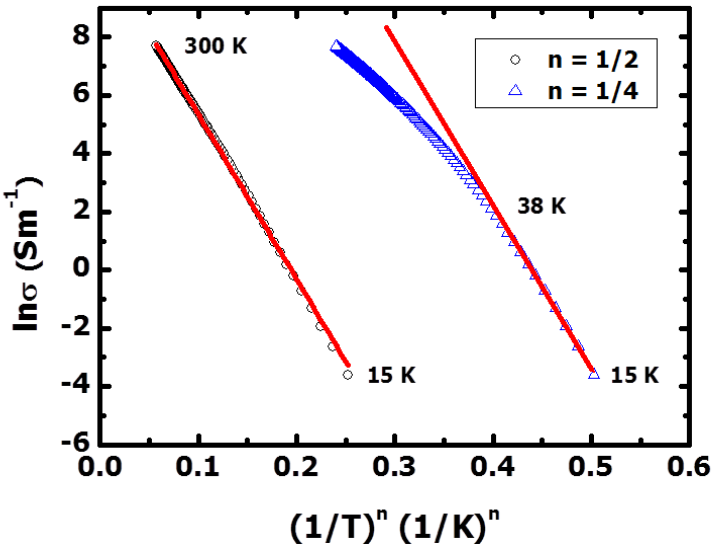

Figure S3.8 ln(σ) versus $(1/T)^n$ for $Cu_{10}Mn_2Sb_4S_{13}$ shows the straight-line fit by Equation (3.2) for $n = 1/2$ ($R^2 = 0.999$), but fit with $n = 1/4$ ($R^2 = 0.982$) deviated from the linearity after 38 K.

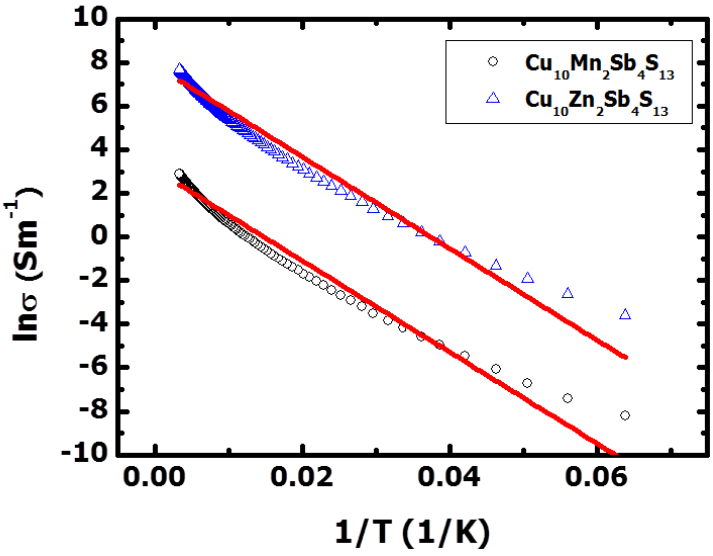

Figure S3.2 ln(σ) versus 1/T for $Cu_{10}Mn_2Sb_4S_{13}$ and $Cu_{10}Mn_2Sb_4S_{13}$ does not fit by normal behavior of carrier doped semiconductors. They show deviation from straight-line beyond 23 K ($R^2 = 0.970$) for $Cu_{10}Mn_2Sb_4S_{13}$ and 35 K ($R^2 = 0.970$) for $Cu_{10}Zn_2Sb_4S_{13}$.

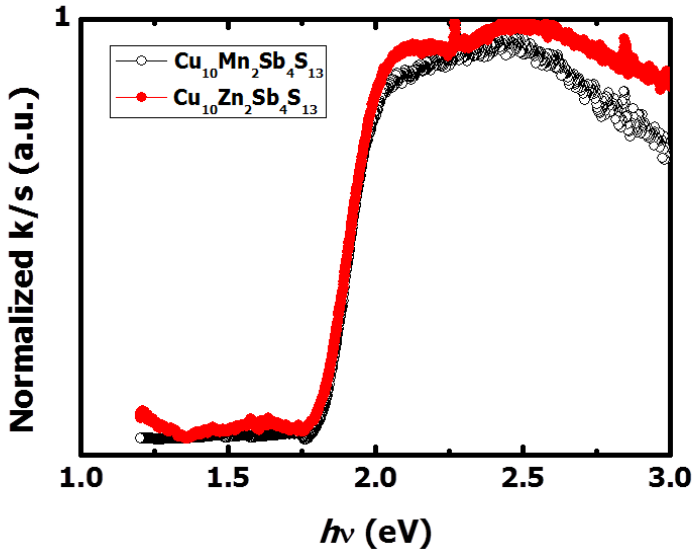

Figure S3.10 Diffuse reflectance of synthetic tetrahedrite powder samples $Cu_{10}Mn_2Sb_4S_{13}$ (open) and $Cu_{10}Zn_2Sb_4S_{13}$ (filled). Both samples exhibit a wide E_G ~ 1.8 eV, unlike other tetrahedrites, which shows a low semi-metallic behavior of the E_G below 0.5 eV.

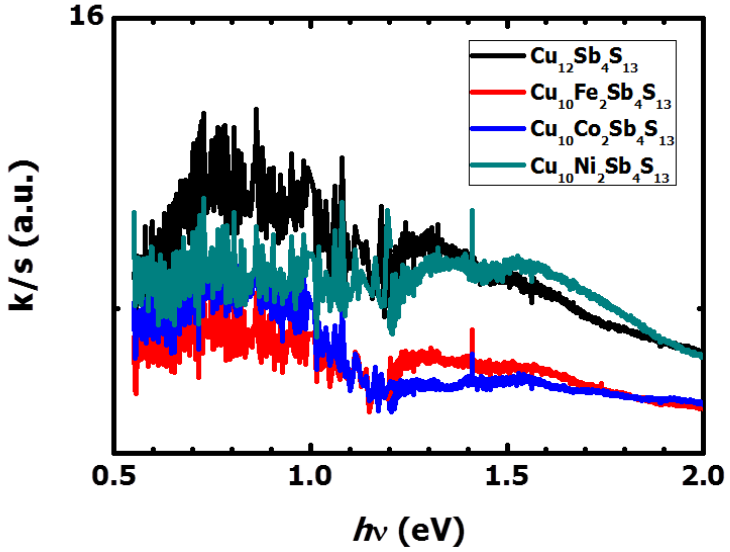

Figure S3.3 Diffuse reflectance of synthetic tetrahedrite powder samples $Cu_{12}Sb_4S_{13}$, $Cu_{10}Fe_2Sb_4S_{13}$, $Cu_{10}Mn_2Sb_4S_{13}$ and $Cu_{10}Zn_2Sb_4S_{13}$. All samples exhibit strong absorption in the range of IR and UV-Vis.

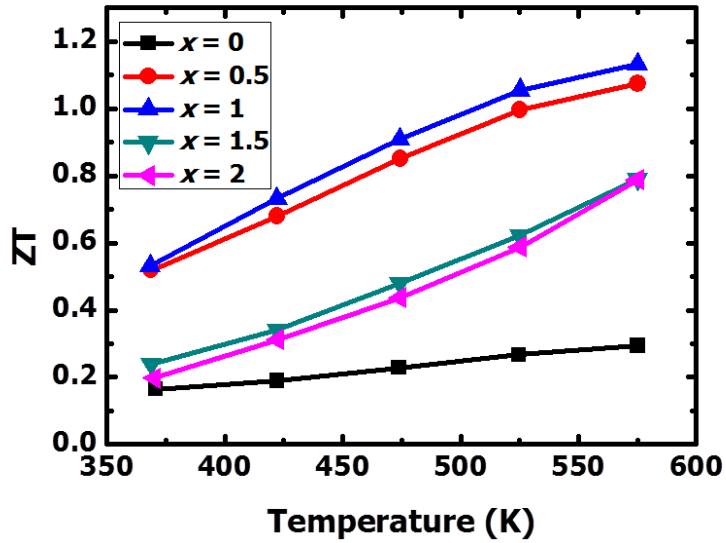

Figure S3.12 Temperature dependence of power factor (PF) for $Cu_{12-x}Mn_xSb4S_{13}$ ($0 \leq x \leq 2$).

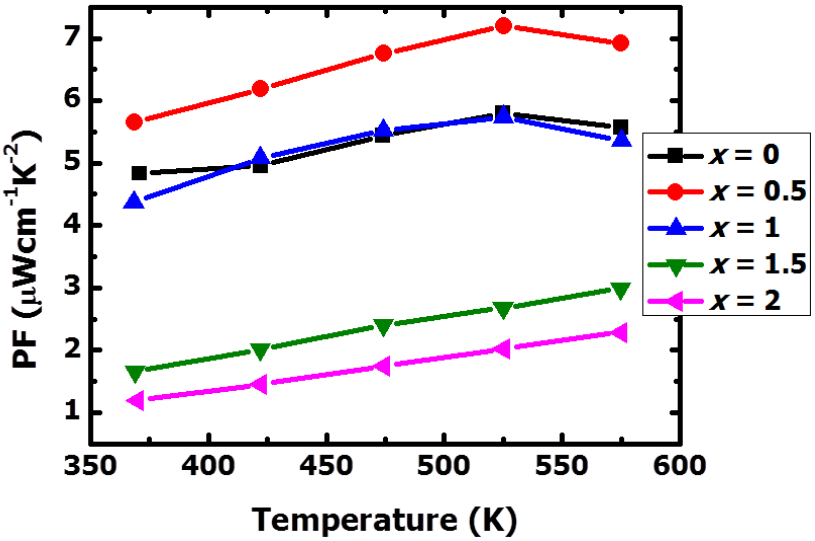

Figure S3.4 Temperature dependence of thermal conductivity (κ) for $Cu_{12-x}Mn_xSb4S_{13}$ ($0 \leq x \leq 2$).

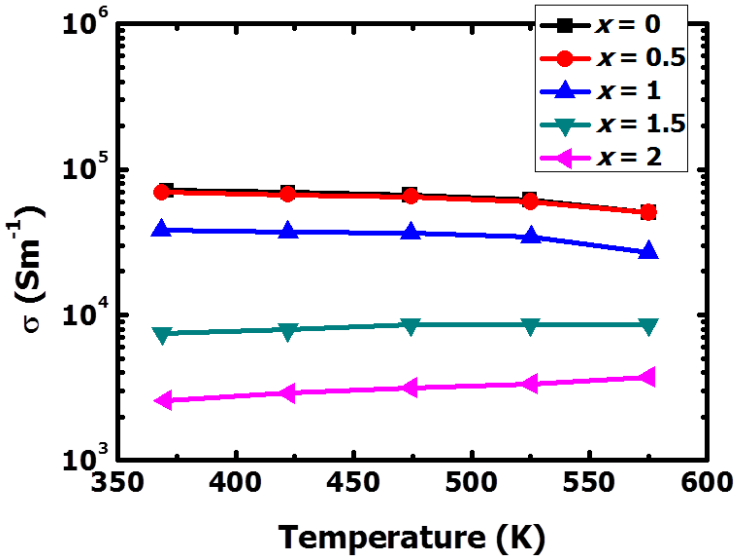

Figure S3.14 Temperature dependence of electrical conductivity (σ) for $Cu_{12-x}Mn_xSb4S_{13}$ ($0 \leq x \leq 2$).

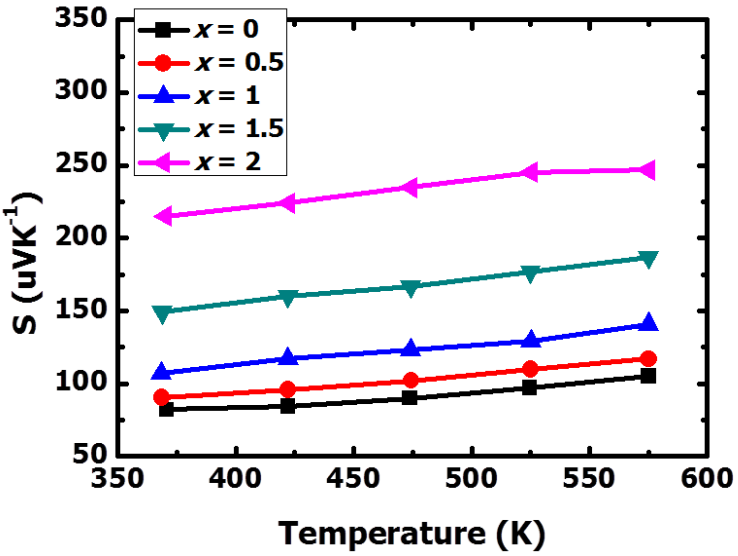

Figure S3.5 Temperature dependence of thermopower (S) for $Cu_{12-x}Mn_xSb4S_{13}$ ($0 \leq x \leq 2$).

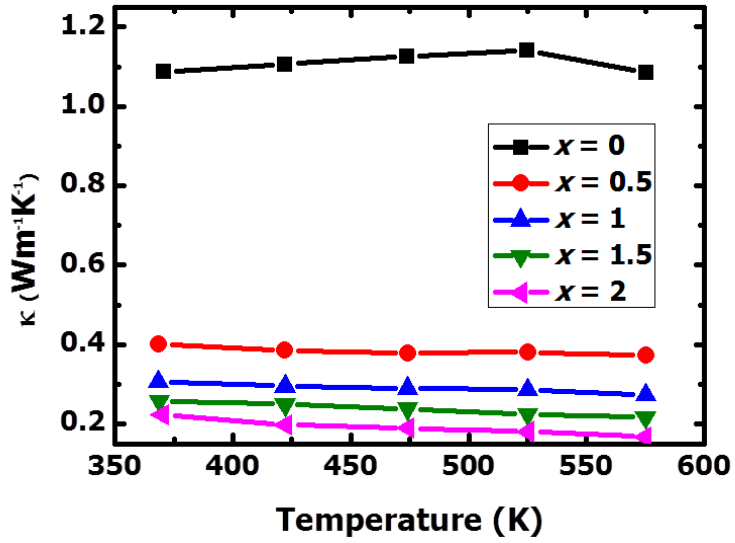

Figure S3.16 Temperature dependence of thermal conductivity (κ) for $Cu_{12-x}Mn_xSb4S_{13}$ ($0 \leq x \leq 2$).

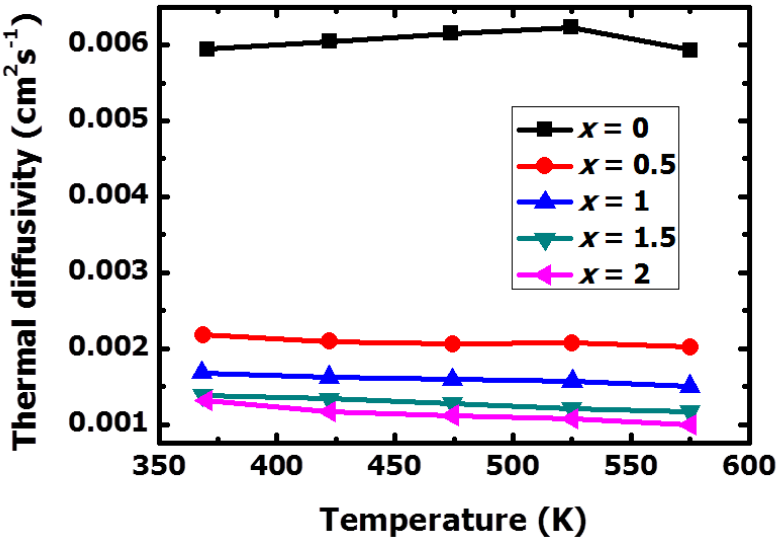

Figure S3.6 Temperature dependence of thermal diffusivity for $Cu_{12-x}Mn_xSb4S_{13}$ ($0 \leq x \leq 2$).

Chapter 4

Optical and Transport Properties of Cu_3-V-VI_4 Earth-Abundant Absorbers

Robert S. Kokenyesi, **Jaeseok Heo**, Vorranutch Jieratum, and Douglas A. Keszler

Department of Chemistry, Oregon State University, Corvallis, Oregon 97331-4003 USA

To be submitted for publication in *Journal of Materials Chemistry C.*

4.1 Introduction

The solar photovoltaic (PV) research community is actively searching for new materials to allow development of high efficiency conversion devices from low cost materials and processes. Current key players are crystalline Si and thin film CdTe and CIGS absorbers. These technologies present roadblocks for bringing PV technology to grid parity. In particular, the necessities for high manufacturing temperatures of Si and use of rare elements in CdTe and CIGS are of concern to name a few. Materials and processing costs can be greatly reduced realizing high absorption materials that are earth-abundant and/or found in concentrated deposits in nature, as well as compatible with low temperature and high-throughput manufacturing. Further gains can be achieved in materials system suitable for tandem solar cells, with maximum efficiencies exceeding the Shockley-Queissar limit[1] for a single-junction.

Recently, rapid onset to high absorption near the fundamental band gap was identified in Cu_3-V-VI_4 (V = P, As, Sb; VI = S, Se) materials[2], hereof referred to as Cu56. Figure 4.1 exhibits the two main crystal structures adopted by the Cu56 materials family. Both structures exhibit similar packing of Cu- and group V tetrahedra, derived from the wurtzite and spharelite structures. The packing order has been related to the volume of the group V tetrahedral.[3] The Cu56 materials exhibit a unique combination of isolated molecular units within a 3D matrix of an inorganic solid. As an example, the structure of Cu_3SbS_4 can be decomposed into a defect 3D chalcopyrite-like framework of copper sulfide and isolated molecular SbS_4 units. Because isolated SbS_4 units do not give rise to significant band dispersion, a high JDOS and strong absorption with rapid onset are observed, leading to the suggestion of an absorber design principle.[2] Superior hole carrier transport is also reported in polycrystalline thin film[2] and bulk pressed pellets form[4] due to the profusion of Cu-polyhedra interconnection. Moreover, photovoltaic conversion

was demonstrated for Cu_3PSe_4 single crystals.[4] Thus, Cu56 presents a rich materials system for application in single- and multi-junction thin film solar cells as absorber layers, composed of earth-abundant and low-cost elements.

In this contribution we report the structural, transport and optical properties of the full Cu56 materials system. We expand on these properties for three new sub-groups of solid solutions, namely $Cu_3P_{1-x}As_xS_4$, $Cu_3P_{1-x}As_xSe_4$ ($0 < x < 1$) and $Cu_3AsS_{4-y}Se_y$ ($0 < y < 4$), as well as partially examined members $Cu_3PS_{4-y}Se_y$[4] and $Cu_3As_{1-x}Sb_xS_4$[3,5].

4.2 Experimental Section

Bulk synthesis was carried out using elemental powders of Cu, P, As, Sb, S and Se supplied by Alfa Aesar of 99.95% purity or higher. The stoichiometric mixtures of appropriate compositions were annealed in evacuated fused silica sealed tubes in the 400 – 500 ℃ temperature range. Slight access of volatile elements such as P, As, S, Se was added to prevent formation of V-element poor secondary phases.

X-ray diffraction (XRD) patterns on powder samples are collected using a Rigaku Ultima IV diffractometer with a 0.02 rad slit and Cu Kα radiation. Scans were made between 10 and 80˚ at a step size of 0.02˚ 2θ and a dwell time of 1 s at each step. The resulting diffractions patterns were compared with ICSD[6] and ICDD-PDF[7] files to extract the unit cell constants using PDXL software suite[8]. For analysis of physical properties, the resulting polycrystalline powders were molded into pellets of ~ 0.25-in diameter and then were sintered at 400 ℃ under 68 MPa pressure to produce sample densities ≥ 85 % of theoretical values. Optical band gaps are estimated from diffuse reflectance measurements on loose powder samples using a W-lamp source and Ocean Optics HR4000 UV-VIS and Near-Infrared spectrometers. Electrical resistivity and ma-

jority carrier transport properties are measured on pressed and annealed pellets in the van der Pauw geometry on a LakeShore 7504 Hall measurement system, applying indium contacts.

4.3 Result and Discussion

Structure. Figure 4.1 summarizes the reported structures of Cu_3PS_4,[9] Cu_3PSe_4,[10] Cu_3AsS_4,[9] as well as some of their solid solutions,[4] adopting the orthorhombic enargite-type structure (space group $Pmn2_1$). Cu_3SbS_4,[11] Cu_3SbSe_4,[11] and Cu_3AsSe_4[12] adopt the tetragonal famatinite-type structure (space group $I42m$). In case of $Cu_3As_{1-x}Sb_xS_4$ system (Figure S4.1a) for $x > 0.1$ a clear structure transformation from orthorhombic to tetragonal is observed and $Cu_3SbS_{4-y}Se_y$ has tetragonal structure. These results agree well with previous study.[5,13] In this section we focus on crystal structure analysis of three unreported solid solutions in the Cu56 system.

The powder X-ray diffraction was performed for three unreported solid solutions in the system, namely the $Cu_3P_xAs_{1-x}S_ySe_{4-y}$ ($0 < x < 1$, $0 \le y \le 4$) compounds (Figure S4.1a – S4.1d). Figure 4.2 exhibits the unit cell constants of these solid solutions extracted from XRD patterns. Based on the apparent similarity of the intermediate as well as the $x = 0$ and 1 compositions in $Cu_3P_xAs_{1-x}S_4$ (Figure 4.2a), we conclude that the wurtzite-related enargite-type structure is assumed by all members of this series. A monotonic unit cell expansion for $0 < x < 1$, following Vegard's law, confirms the uniform incorporation of the larger crystal radius As cation on the smaller P cation site. This result is similar to that reported for $Cu_3PS_{4-y}Se_y$ compounds.[4]

The $Cu_3AsS_ySe_{4-y}$ ($1 \le y \le 4$) and $Cu_3P_{1-x}As_xSe_4$ ($0 \le x \le 0.75$) solid solutions also crystallize in the orthorhombic structure, as shown in Figures S4.1b and S4.1c, respectively. However, a structure transition is expected in these systems as the Cu_3AsSe_4 composition with the tetragonal unit cell is approached. In case of $Cu_3AsS_ySe_{4-y}$ such transition is not observed for $y \ge 1$. A

unique pattern is observed for $Cu_3As_{0.9}P_{0.1}Se_4$. Using a model enargite structure with random distribution of P and As on the respective a-site yields a similar pattern, however an exact match is not obtained. Long range ordering of P/As cations may be present to account for the differences.

In all solid solutions examined the unit cell volume clearly increases with the incorporation of larger cations, e.g., P → As → Sb, or larger anion, e.g., S → Se. The wide range of solid solutions available in this materials system enables fine tuning of the optical and electronic properties over a wide range, relevant to application as absorbers in thin film solar cells.

Optical Properties. The variation of optical band-gaps is illustrated for all solid solutions with the change of the compositions in Figure 4.3a. The band-gaps in the Cu56 system monotonically decrease with the unit cell volume and the ionic radii of Group V and VI from 2.4 eV (eg Cu_3PS_4) to 0.6 eV (eg Cu_3AsSSe_3 and Cu_3SbS_3Se) which fall in the desirable band-gap ranges for solar absorber application in PV cells. Cu_3SbS_4 has the lowest observed optical band-gap of 0.9 eV in the sulfide system that necessitates addition of Se for some tandem cell applications. Cu_3SbSe_4 and Cu_3AsSe_4 have the smallest band-gap, E_G ~ a few meV[12,14] in Cu56 system thus mixed anion solid solutions provide opportunity for fine-tuning the optical band edge. This trend of a band-gap variation with the compositions in a same crystal structure, is commonly observed, i.e., $CuGaS_2$ (E_G = 2.53 eV), $CuInS_2$ (E_G = 1.55 eV), $CuInSe_2$ (E_G = 1.0 eV).[15] However, the related $Cu_3(Vb)Ch_4$ (Vb = V, Nb, Ta) group of materials have the opposite trend of increasing band gap with larger unit cell volume and could be used to further tune optoelectronic properties of Cu_3-V-VI_4 materials [future work reported separately].

The optical band gap modulation can be explained by reported DFT calculations that establish Group V *ns* – VI *np* antibonding character near the conduction band minimum (CBM) and Cu 3*d* – Group VI *np* antibonding character near the valence band maximum (VBM) in the Cu56

system.[2,16] The larger group V cation produces smaller splitting of the boding and antibonding states, lowering the energy position of the CBM. The higher absolute energy level of Se 4*p* states compared to those of S 3*p* states raises the energy of the VBM, while the modest splitting of bonding and antibonding states for the Cu – Se and Group V – Se interactions versus Cu – S and Group V – S interactions, respectively, leads to a lower energy CBM. The net effect is an overall narrowing of the energy gap in the materials with increasing Se concentration. Likewise, following down Group V from P to Sb, the higher energy level of Sb 5*s* and 5*p* states, compared to ns and np orbitals of P and As, could push up VBM and push down CBM, resulting in a narrower band-gap energy. In $Cu_3(As,Sb)S_4$ solid solutions, for example, the more Sb content, the more density of states (DOS) of Sb contribution, and the narrower band-gap obtains.

Interestingly, we note that two lines linearly fit to the plot of the unit cell volume vs. the band-gap; one line fits the data points of $Cu_3P(S,Se)_4$ and $Cu_3(P,As)Se_4$ solid solutions, and the other fits the data points of $Cu_3As(S,Se)_4$, $Cu_3(P,As)S_4$, and $Cu_3(As,Sb)S_4$ solid solutions (Figure S4.2). Two distinguish slopes could be related with the contribution of Cu 3s – Group VI hybridization on CBM. In Cu-P-Se ternary compounds, P 3*s* weakly interact with the anion Se 4*p* states and Cu 4*s* mainly contribute to CBM, while other cations As and Sb has the high energy level enough to interact with both anions S and Se contributing mainly to CBM.

Electrical Properties. Resistivity (ρ), carrier concentration (*p*), and mobility (μ) from Hall effect on pressed pellets are shown in Figure 4.3b - d. Seebeck coefficients are consistent with *p*-type semiconductor behavior (300 – 500 μVK^{-1}). The hole majority carrier type is likely due to the prevalence of Cu vacancies within a matrix of d^{10} Cu^{1+}, similarly to other copper-chalcogenides. Electrical resistivities vary by approximately three orders of magnitude in samples with anion substitution, leading to values $\rho < 0.6$ ohm cm in both Cu_3PSe_4 and Cu_3AsSe_4,while those of cat-

ion substitutions differ by an order (Figure 4.3b). Thus, the electrical transport properties of the Cu56 system can be mainly attributed to the aforementioned change of bonding character with increasing Se content.

The electrical resistivity is mainly determined by two factors: carrier concentration (*p*) and mobility (μ). As seen from comparison of Figure 4.3c and 4.3d, higher carrier concentrations are the main contributors to the electrical resistivity in Se substituted solid solution, $Cu_3P(S,Se)_4$ and $Cu_3As(S,Se)_4$. To consider the origin of the elevated carrier concentration in Se materials, we need to account for the defect formation energy in copper chalcogenides. It is well known that the neutral Cu vacancy in copper chalcogenides has commonly the lowest formation enthalpy, depending on certain chemical potential.[17] With rising Fermi energy in band-gap or decreasing band-gap, the formation energies of these defects will further reduce. Therefore, Se substitution with smaller band-gap has lower defect formation energy, leading to higher carrier concentrations than S-based compounds as in $CuIn(S,Se)_2$[16] and $Cu_2ZnSn(S,Se)_4$.[18]

Figure 4.3d shows the room-temperature Hall mobility as a function of cation and anion concentrations. An increase in carrier mobility is also observed with increasing Se content, producing ~ 70 $Vcm^{-1}s^{-1}$ in $Cu_3P_{0.1}As_{0.9}Se_4$. This increase in mobility is expected for band broadening through higher covalency in Se substituted materials. Interestingly, the order in mobility from lowest to highest comprises the cations Sb ~ As > P, while there is no clear trend of carrier concentrations with cation substitution. This increase in mobility with larger cations is likely associated with the change of additional band characteristics. Transport property values on pressed bulk samples can vary significantly, because of grain-boundary effects of the polycrystalline micro-structure.[19]

4.4 Conclusion

We have explored that the electrical and optical properties of Cu_3-V-VI_4 (V = P, As, Sb; VI = S, Se) materials system. Band gap tuning across the 0.6-2.4 eV photon energy range is possible in quaternary and quinternary solid solutions. High carrier mobilities in bulk pressed pellets indicate electrically benign grain boundaries. The desirable optical and electrical properties are explained based on the crystalline lattice structures adopted by the Cu_3-V-VI_4 compounds.

Reference

[1] W. Shockley, H. J. Queisser, *J. Appl. Phys.* **1961**, *32*, 510.

[2] L. Yu, R. S. Kokenyesi, D. a. Keszler, A. Zunger, *Adv. Energy Mater.* **2013**, *3*, 43.

[3] M. Pósfai, P. R. Buseck, *Am. Mineral.* **1998**, *83*, 373.

[4] V. Itthibenchapong, R. S. Kokenyesi, A. J. Ritenour, L. N. Zakharov, S. W. Boettcher, J. F. Wager, D. A. Keszler, *J. Mater. Chem. C* **2013**, *1*, 657.

[5] A. Pfitzner, T. B. Bernert, *Zeitschrift für Krist. - Cryst. Mater.* **2004**, *219*, 20.

[6] F. H. Allen, G. Bergerhoff, I. Brown, **2013**.

[7] **n.d.**

[8] Rigakuo, **2010**.

[9] A. Pfitzner, S. Reiser, *Zeitschrift für Krist. - Cryst. Mater.* **2002**, *217*, 51.

[10] H. W. Ma, G. C. Guo, G. W. Zhou, M. S. Wang, S. H. Lin, Z. C. Dong, J. S. Huang, *Chinese J. Struct. Chem.* **2002**, *21*, 288.

[11] Y. Kanazawa, *Bull. Geol. Surv. Japan* **1984**, *35*, 13.

[12] O. Madelung, U. Rössler, S. M., *Landolt-Börnstein - Gr. III Condens. Matter* **2000**, *41*, 1.

[13] E. J. Skoug, J. D. Cain, D. T. Morelli, M. Kirkham, P. Majsztrik, E. Lara-Curzio, *J. Appl. Phys.* **2011**, *110*, 023501.

[14] D. Do, S. D. Mahanti, M.-S. Lee, Y. Zhang, C. Wolverton, in *APS March Meet.*, **2012**, p. L17.009.

[15] R. Scheer, H.-W. Schock, *Chalcogenide Photovoltaics: Physics, Technologies, and Thin Film Devices*, Wiley-VCH, Wienheim, **2011**.

[16] D. T. Do, S. D. Mahanti, *J. Phys. Chem. Solids* **2014**, *75*, 477.

[17] S. B. Zhang, S. Wei, A. Zunger, **1998**, *57*, 9642.

[18] E. M. Mkawi, K. Ibrahim, M. K. M. Ali, A. S. Mohamed, *Int. J. Electronchemical Sci.* **2013**, *8*, 359.

[19] A. F. Mayadas, M. Shatzkes, *Phys. Rev. B* **1970**, *1*, 1382.

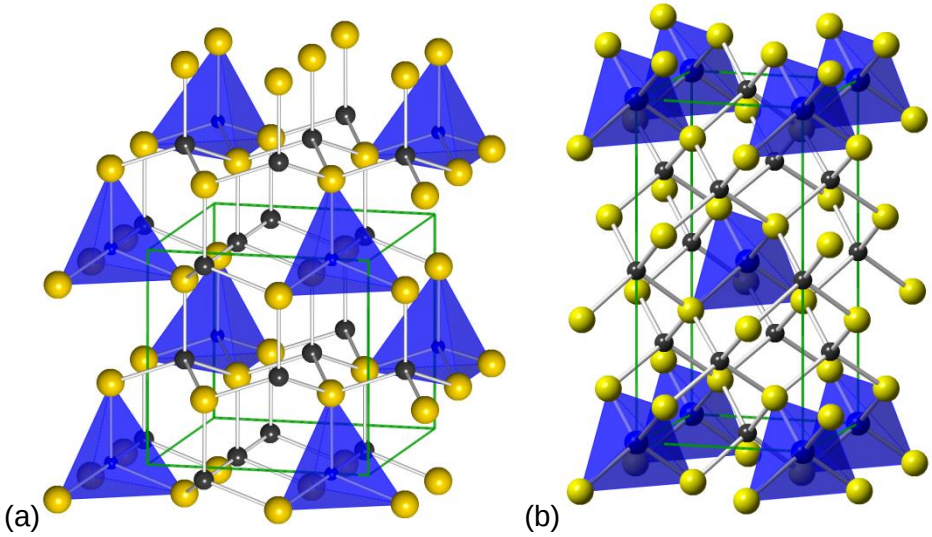

Figure 4.1 Crystal structures adopted by the Cu_3-V-VI_4 materials family. The orthorhombic structure (a) is more common including $Cu_3P(S,Se)_4$ and Cu_3AsS_4. The tetragonal structure (b) is assumed by Cu_3SbS_4 and Cu_3AsSe_4.

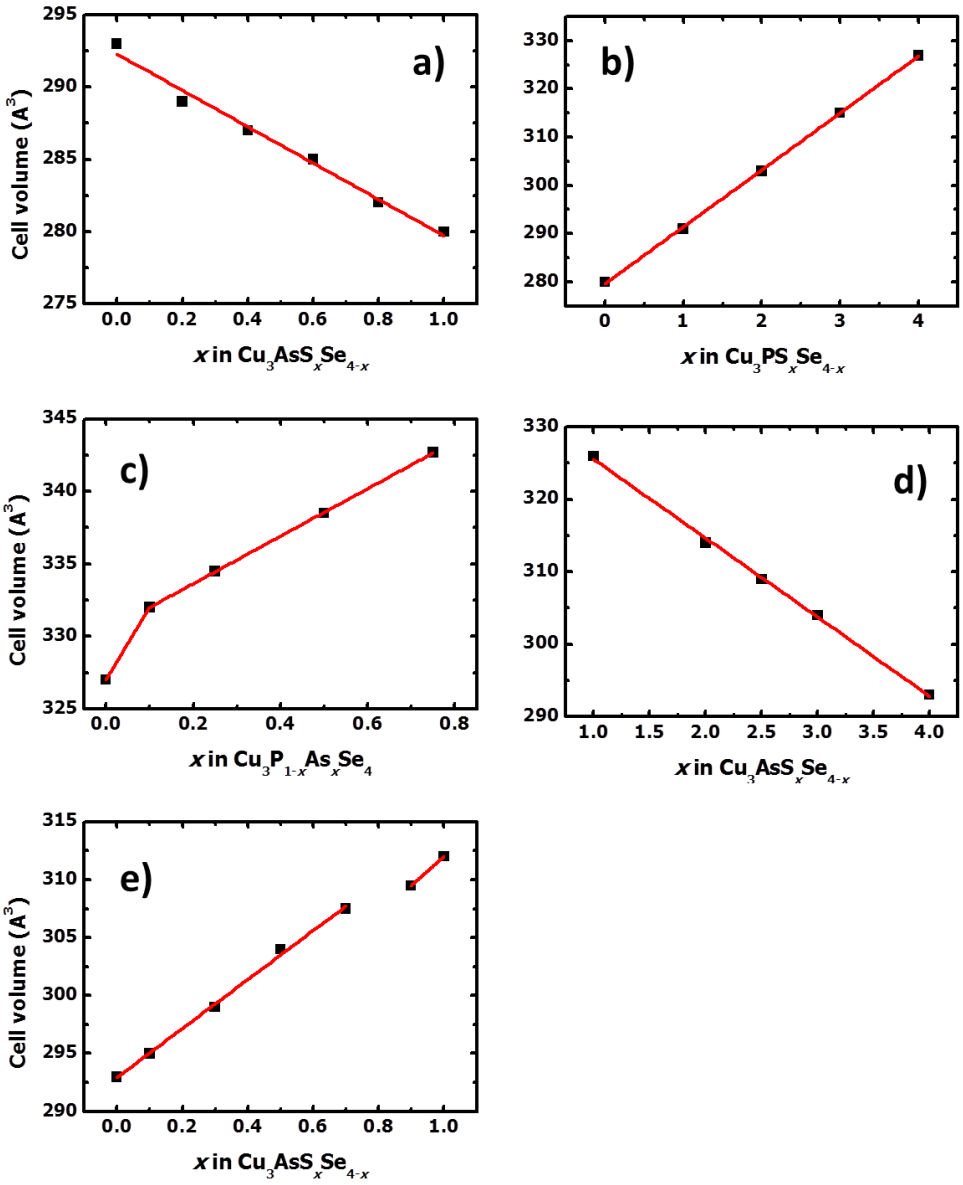

Figure 4.2 Extracted cell parameters from bulk XRD patterns of Cu_3-V-VI_4 materials family.

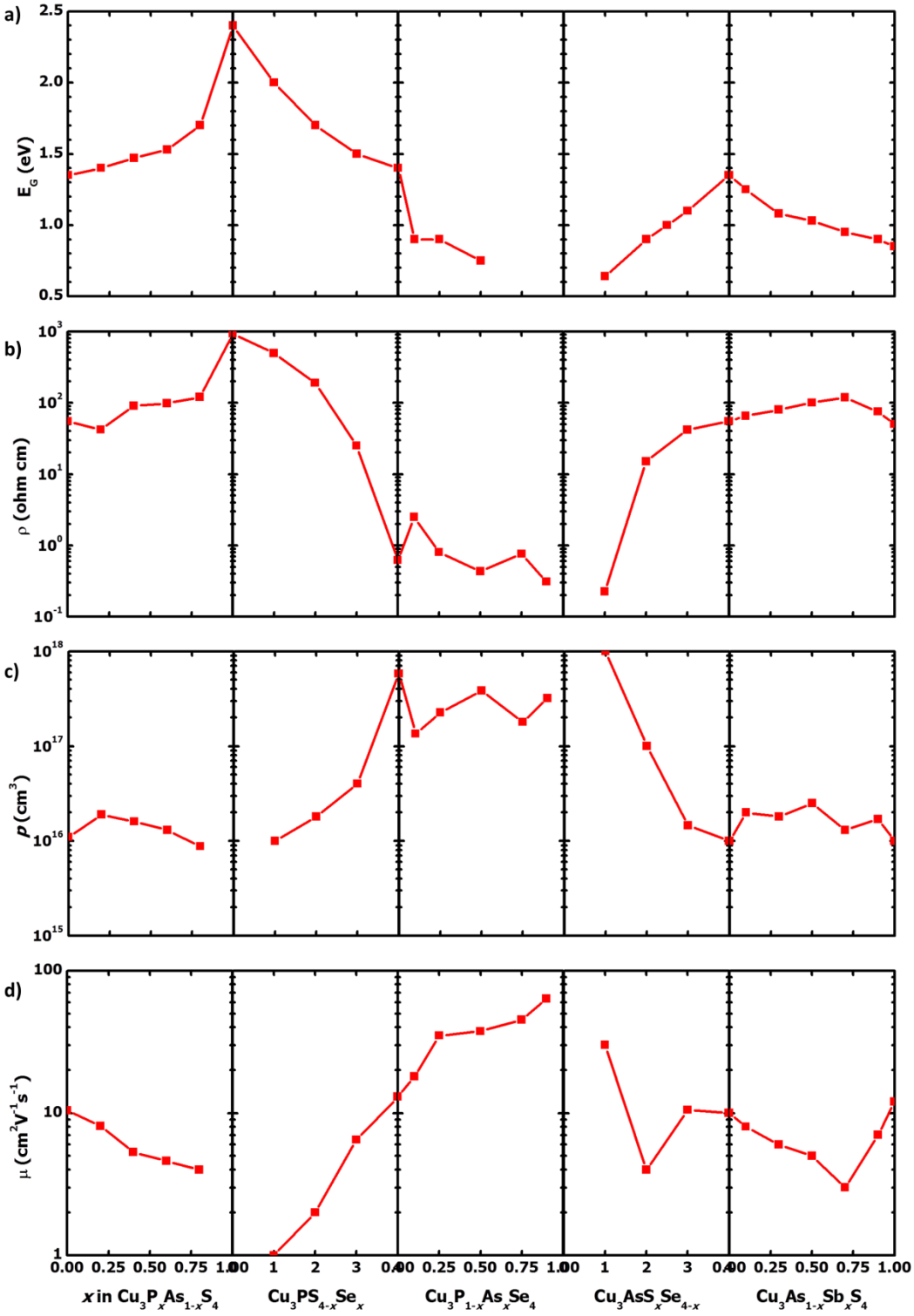

Figure 4.3 (a) optical band-gap, (b) resistivity, (c) carrier concentrations, and (d) Hall mobility of Cu_3-V-VI_4 materials family.

Supporting Information for

Optical and Transport Properties of Cu_3-V-VI_4 Earth-Abundant Absorbers

Robert S. Kokenyesi, **Jaeseok Heo**, Vorranutch Jieratum, and Douglas A. Keszler

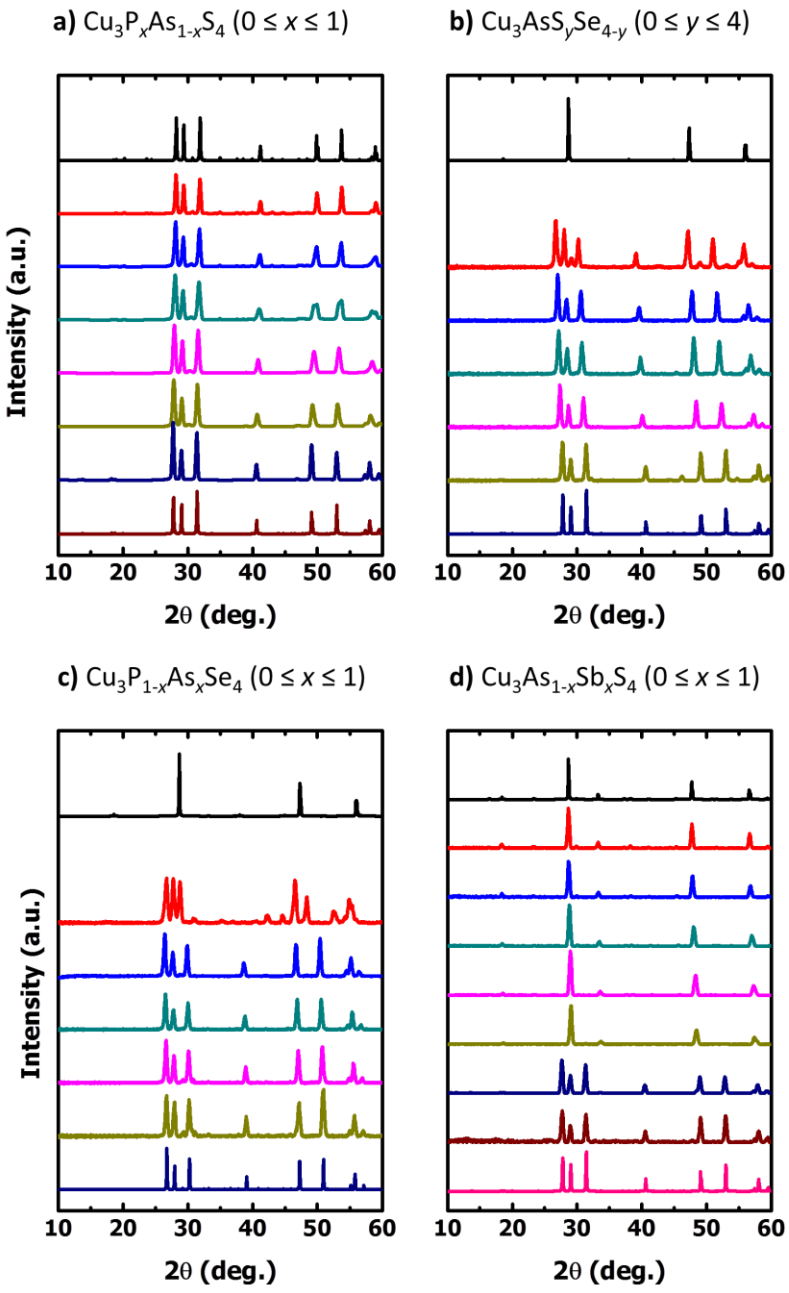

Figure S4.1 X-ray diffraction patterns: (a) $Cu_3P_xAs_{1-x}S_4$ ($0 \le x \le 1$) solid solutions of the orthorhombic enargite structure; (b) $Cu_3AsS_ySe_{4-y}$ ($1 \le y \le 4$) with the enargite structure, converting to tetragonal unit cell at $y < 1$; (c) $Cu_3P_{1-x}As_xSe_4$ ($0 \le x \le 1$) solid solutions; (d) $Cu_3As_xSb_{1-x}S_4$ ($0 \le x \le 1$) solid solutions. Calculated patterns from ICSD for Cu_3PS_4 (#412240), Cu_3PSe_4 (#41906), Cu_3AsS_4 (#413350) and Cu_3AsSe_4 (#610359) are demonstrated for reference.

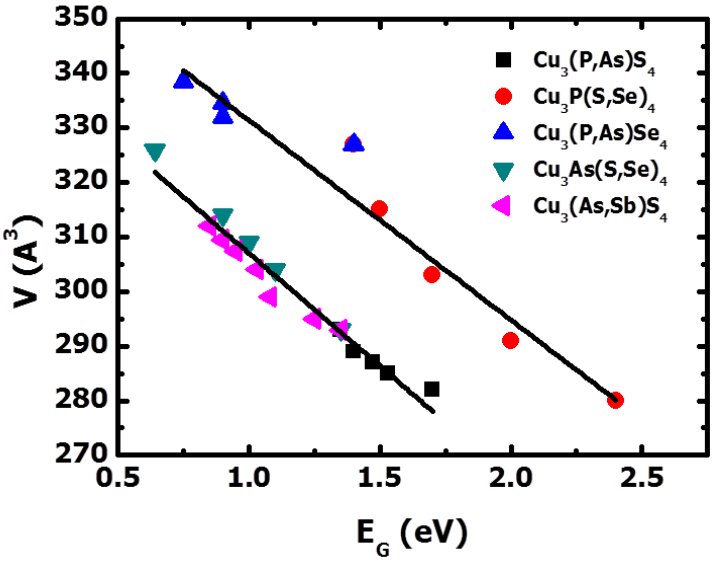

Figure S4.2 Relationship between unit cell volumes and optical band-gaps in Cu_3-V-VI_4 materials system.

Chapter 5

Search for Missing Compound Co_2GeS_4 through $(Fe,Co)_2GeS_4$ and $(Co,Zn)_2GeS_4$ Solid Solutions: A Theoretical and Experimental Approach

Jaeseok Heo[1], Xiuwen Zhang[2], Robert S. Kokenyesi[1], Alex Zunger[3], and Douglas A. Keszler[1]

[1]Department of Chemistry, Oregon State University, Corvallis, Oregon 97331-4003 USA

[2]Department of Physics, Colorado School of Mines, Golden, Colorado, 80401, USA

[3]University of Colorado, Boulder, Colorado 80309, USA

To be submitted for publication in *Journal of Solid State Chemistry.*

5.1 Introduction

A_2BX_4 metal-chalcogenide compounds, with A and B elements being either main group elements or only one of them being a 3d transition metal and X a chalcogen (O, S, Se, Te), constitute a centrally important group of ternary materials with 255 reported compounds that manifests a wide range of physical and chemical properties. Known applications of these include transparent conductors,[1] thin film transistors,[2] thermoelectric,[3] lithium ion batteries,[4] and photovoltaic absorbers.[5] In part, such a diversity of useful properties originates from the variety of adopted crystal structures (currently 32 are known), and a range of cation coordination (4-fold to 7-fold) and valence (II, III, IV) in forming crystal structures.[6] Interestingly, however, current compilations of A_2BX_4 compounds based on the two standard inorganic chemistry databases: the inorganic chemistry structural database (ICSD)[7] and the powder diffraction file (ICDD-PDF),[8] reveal a significant number of materials that are missing out of the possible 656 combinations within the fixed elemental composition space. Although a large number of A_2BX_4 compounds appear to be missing, many of these ternary chalcogenides may be thermodynamically unstable. Hence, experimental synthesis may have been carried out but unsuccessful, and therefore remained unreported.

On similar concerns, one intriguing solution emerged out of A. Zunger's recent paper, in which the authors explicitly report on prediction of several missing A_2BX_4 metal-chalcogenide compounds via first-principles thermodynamics.[9] Among them, we found it quite striking that their calculations converged towards the existence of Co_2GeS_4 with the tetrahedral structure (Figure. 5.1b) due to two important reasons: (i) this is the only unreported M_2GeCh_4 compounds to date in the company of nearby 3d transition metal-chalcogenide compounds, that includes reported M_2GeO_4 (M = Mn, Fe, Co, Ni, Cu, Zn), M_2GeS_4 (M = Mn, Fe, Ni, Cu, Zn), and M_2GeSe_4 (M =Mn, Fe, Co)[7,8]; (ii) this compound has a wide range of theoretically predicted chemical stability (the

green region in Figure 6.2) compared to other missing compounds calculated in Ref. 9, as we will see later. Mathematically, this region represents a set of conditions energetically favoring the formation of the ternary compound, with respect to competing phases. That is, these wider stability ranges allow us more easily to meet thermodynamically stable phase. Therefore, we tried specifically to synthesize the most probable of class, Co_2GeS_4, to complement theoretical predictions. However, Co_2GeS_4 was not obtained. Facing such a contradiction between experiment and theory, we decided to take a closer look at the system in order to add new insight into the intrinsic factors that determine the nature of cobalt in forming a crystalline phase in ternary A_2BX_4 composition. It is believed that such experimental work would help improve theoretical density functional theory (DFT) models such as the local density approximation (LDA) and the generalized gradient approximation (GGA) with the value of the Hubbard U parameters.

Inspired by the previous literatures in which a phase transition of several compounds was demonstrated by a solid solution approach,[10–14] we decided to investigate site preference of the Co^{2+} cation in the crystal structure of the solid solution system with similar compositions. A few studies have so far been made on $(Mn,M)_2GeS_4$ (M = Fe, Co, Ni, Cd) and $(Fe,M)_2GeS_4$ (M = Mg, Mn, Zn) solid solutions.[12,13] H. Haeuseler, et al., found for the $(Mn,Co)_2GeS_4$ system that large regions of solid solutions crystallized in the olivine-type structure.[12] Later on, their other researches showed that Fe and Co have similar preference for the octahedral site occupation in the $(Mn,M)_2GeS_4$ system, which suggested that the solid solutions between Fe and Co could have larger crystallizing regions in the olivine-type structure.[13] Phase investigations of (Co,M)S (M = Mn, Zn,Cd) binary solid solutions have also been carried out in order to verify the site preference of Co^{2+} ions in different crystal structures: rocksalt, sphalerite, and wurtzite type, and the solubility limits came to two principal conclusions: (i) Co^{2+} ions have no pronounced site preference for a

special environment due to crystal field stabilization and (ii) the different solubility of cobalt sulfide could be only understood by the ionic radii.[14] However, these results, unfortunately, cannot explain why Co_2GeS_4 does not exist in either olivine or spinel (O_h occupancy), or tetrahedral (T_d occupancy) structures unlike nearby components with similar radii. Therefore, we studied, for the first time, the details of the $(Fe,Co)_2GeS_4$ and $(Co,Zn)_2GeS_4$ solid solutions structure using X-ray diffraction, and thus elucidate how the Co-substitution influences the structure in order to examine the missing Co_2GeS_4 compound. The focus of this work is to study the cobalt content and temperature dependence of the $(Fe,Co)_2GeS_4$ and $(Co,Zn)_2GeS_4$ phase diagram through the chemical synthesis and structural investigation in order to validate the theoretical calculation and to establish the framework between the theoretical prediction and the experimental results.

5.2 Experimental Section

A two-step approach was used to predict the existence of Co_2GeS_4 compound.[9] First of all, the structure types from ICSD were used to find the lowest-energy crystal structure of an unknown Co_2GeS_4 compound.[15] We compute the total energies of all 32 structure types by relaxing all external (cell shape) and all internal (atomic positions) degrees of freedom. The electronic degrees of freedom are described within DFT by the GGA + U approximation, and the total magnetization is also relaxed to the ground state by using the Perdew-Burke-Ernzerhof (PBE) exchange-correlation functional[16] as implemented in the Vienna ab initio simulation package (VASP), the projector-argumented wave (PAW) pseudopotential[17]. An energy cutoff of 220-520 eV is used. Second, it is to determine whether new predicted structure is stable with respect to decomposition into its competing phases. To address this issue, formation enthalpy energies (ΔH_f) of all decomposition

reactions involving Co_2GeS_4 are calculated. This calculation was done using GGA + U with fitted elemental-phase reference energies" (FERE).[15]

$(Fe,Co)_2GeS_4$ and $(Co,Zn)_2GeS_4$ solid solutions were synthesized by a solid state reaction with iodine as a transport agent. The starting materials were commercial reagent grade Fe, Co, Zn, Ge, and S having purity > 99.99 % from Alfa Aesar. Stoichiometric quantities of reactants with slight Ge and S excess were mixed and heated at 300 ~ 1050 ℃ for 1 week in evacuated sealed fused-silica tubes. Excess Ge and S are used due to volatility of GeS material, which creates a substantial amount of weight loss, as well as a change in the compositional ratio of the constituents in the solid solution. Additional regrinding and reheating was carried to achieve high crystallinity and purity solid solutions, for high resolution X-ray analysis. The phase of $(Fe,Co)_2GeS_4$ and $(Co,Zn)_2GeS_4$ solid solutions was characterized by a Rigaku Ultima IV diffractometer with a 0.02 rad slit and Cu Kα radiation (λ= 1.5418 Å). Data were collected between 10 and 60 ° at a step size of 0.02 ° and a dwell time of 1 s. The obtained powder X-ray diffraction patterns were compared with ICSD and ICDD-PDF files using the PDXL software suite.[18]

5.3 Results and Discussion

Figure 5.1a and 5.1b show experimentally confirmed Fe_2GeS_4[19] and theoretically predicted Co_2GeS_4[9] structures, respectively. Fe_2GeS_4 compound adopts the well-known olivine-type structure (space group *Pnma*), in which the Fe atoms occupy two different octahedral (O_h) sites, 4a (0 0 0) and 4c (x 1/4 z), and the Ge atoms occupy tetrahedral (T_d) sites, 4c (x 1/4 z). The 4a Oh site is smaller and more symmetric than larger and more distorted 4c Oh site. On the other hand, theoretical calculations predicted Co_2GeS_4 to have the deficient zincblen-like Ag_2HgI_4-type structure

(space group *P-42m*, a = 5. 467 Å, c = 4.917 Å), in which Co and Ge atoms both occupy tetrahedral sites 2f (0 1/2 1/2) and 1a (0 0 0), respectively, arranged by S atoms at 4n (x y z) with x = 0.2502 and z = 0.2337. Analog to normal/inverse spinel structures, the simplest inverse Ag_2HgI_4-type structure generated by swapping a pair of Co-Ge atoms in the 7-atom primitive cell was calculated[9] and found to have slightly lower total energy than the normal Ag_2HgI_4-type structure. The energy difference between normal and inverse Ag_2HgI_4-type structures is rather small (less than 1 meV/atom), reflecting that there is neglectable site preference for both Co and Ge on the tetrahedral sites in the deficient zincblend-like structure. Thus at finite temperature Co_2GeS_4 may have Co and Ge atoms randomly distributed on the tetrahedral sites in the zincblend-like structure, resulting in cubic zincblend-like structure with Co/Ge randomly occupied on the cation sites, which is the observed crystal structure of Zn_2GeS_4 compounds.[12]

Figure 5.2 expresses calculated ranges of chemical potentials of the elements in which Co_2GeS_4 is thermodynamically stable. This range of stability is identified excluding the regions of chemical potentials in which competing phases are energetically favored. For the given Co_2GeS_4 compound, in order to be thermodynamically stable, the following set of equality and inequalities needs to be satisfied[15]:

$$2\Delta\mu_{Co} + \Delta\mu_{Ge} + 4\Delta\mu_{S} = \Delta H_f(Co_2GeS_4), \qquad (5.1)$$

$$\Delta\mu_{I} \leq 0, (I = Co, Ge, S), \qquad (5.2)$$

$$n^{(i)}\Delta\mu_{Co} + m^{(i)}\Delta\mu_{Ge} + q^{(i)}\Delta\mu_{S} \leq \Delta H_f\left(Co_{n^{(i)}}Ge_{m^{(i)}}S_{q^{(i)}}\right), (i = 1, \dots, Z) \qquad (5.3)$$

with Z the total number of binary and ternary competing phases with chemical formulae $Co_{n^{(i)}}Ge_{m^{(i)}}S_{q^{(i)}}$ and formation enthalpies $\Delta H_f\left(Co_{n^{(i)}}Ge_{m^{(i)}}S_{q^{(i)}}\right)$. Equation (5.1) represents a plane in the three-dimensional $(\Delta\mu_{Co}, \Delta\mu_{Ge}, \Delta\mu_{S})$ space whose Caresian axes corresponding to the

chemical potentials of the elements and, therefore, leaves the chemical potentials of two of the three species as independent variables. Such a region on the Equation (5.1) is represented in Figure 5.2 via its two-dimensional projection onto the plane of the $\Delta\mu_{Co}$ and $\Delta\mu_{Ge}$ chemical potentials at $\Delta\mu_S = 0$. If there is a violation of at least one of the inequalities (5.3) at any point inside the triangle then the Co_2GeS_4 compound is predicted unstable under the thermodynamic equilibrium conditions, otherwise Co_2GeS_4 is thermodynamically stable in this calculation as illustrated in Figure 5.2. Since $\Delta\mu$ describes the state of the source of pure elements, the region of the triangle within which the examined Co_2GeS_4 forms can be directly translated to the needed growth conditions. In the case of sulfides, the range of $\Delta\mu_S$ for which the Co_2GeS_4 forms can be translated into ranges of sulfur partial pressure and temperature needed for growth. Indeed, the stability plot of Co_2GeS_4 indicates that this compound should form within a wide range of chemical potentials.

Powder X-ray diffraction (XRD) was performed for each of $(Fe,Co)_2GeS_4$ and $(Co,Zn)_2GeS_4$ solid solutions obtained from samples brought to equilibrium with iodine as a transport agent at 550 ℃ and 1050 ℃, respectively (Figure S5.1 and S5.2). Figure 5.3a – 5.3d shows the unit cell constants of $(Fe,Co)_2GeS_4$ solid solutions extracted from these XRD patterns. With increasing molar ratio of cobalt, the unit cell constants a and b of the olivine-type $(Fe,Co)_2GeS_4$ solid solutions decrease up to $x = 0.3$, together with the appearance of broad diffraction peaks. On the other hand, c is almost constant up to $x = 0.8$, where the limit of the olivine-type structure was detected. The slope of the curve obeyed Vegrad's law.[20] Figure 6.3e shows the extracted unit cell volume of $(Co,Zn)_2GeS_4$ solid solutions. The unit cell volume V of the tetrahedral-type $(Co,Zn)_2GeS_4$ solid solutions initially increases up to $x = 0.2$ comparing to initial Zn_2GeS_4 volume and decreases up to $x = 0.5$ with increasing molar ratio of cobalt. Interestingly, it shows the abrupt change of the unit cell volume between $x = 0.2$ and 0.3, which is evident the

compositionally driven structural phase transition. This nonlinear displacement suggests Co^{2+} cations occupy both O_h and T_d sites initially, which makes initial cell volume increase. This work, however, does not mention the possible existence of intermediate olivine or spinel phase. In both of solid solutions, cation substitution makes distortion in the structure even though the distortions of the coordination O_h and T_d in the sulfide-based structure are smaller than in the oxide-based one. Therefore, Co^{2+} cation substitution could make the olivine-type $(Fe,Co)_2GeS_4$ and the tetrahedral-type $(Co,Zn)_2GeS_4$ solid solutions to be unstable due to three important factors: (i) the presence of shared edges or corners shortened to reduce metal-metal repulsion forces, (ii) the ionicity difference of the Co-S bond comparing to the Fe-S and the Zn-S bonds, and (iii) the misfit between Oh and Td sites after the substitution. Considering the structures known binary and ternary cobalt sulfide compounds occupying Oh or Td sites, we may wonder though if an edge-shared Co^{2+} Oh within the olivine-type structure and the corner-shared Co^{2+} Td with the tetrahedral-type structure are stable, none of the binary Co-S compounds exhibit Co^{2+}-Co^{2+} bond lengths comparable to that of Fe^{2+}-Fe^{2+} bond length (~ 3.6 Å) in Fe_2GeS_4 and that of Zn^{2+}-Zn^{2+} bond length (~ 3.9 Å) in Zn_2GeS_4. For comparison, Fe^{2+} and Zn^{2+} cations have similar arrangement in Fe_2S_3 smythite[21] and in ZnS (space group *F4-3m*)[22]. So far, edge-shared Oh sites of nearest neighbor Co are reported only for Co^{2+} in Mo_2CoS_4 (space group *Cc*)[23] and for Co^{3+} in Co_3S_4 (space group *Fd3-mz*)[24] (and spinels thereof) with much shorter Co-Co distances of 3.3 Å. In case of corner-shared Td sites, the distance of nearest neighbor Co is 3.5 Å in Co_9S_8 (space group *Fm3-m*), respectively.[25] Such preference to short Co-Co distances complies with the results on larger contraction of the a and b parameters in $(Fe,Co)_2GeS_4$ solid solutions in order to diminish the average metal-metal distance at shared-edge sites, and may result in large distortions in both the olivine-type

structure of the $(Fe,Co)_2GeS_4$ and the tetrahedral-type structure of the $(Co,Zn)_2GeS_4$ and subsequently lead to its destabilization beyond the their solubility limits.

To address the above issues further, we investigated the temperature dependent phase diagrams of two series of solid solutions plotted in Figure 5.4a and 5.4b. In the system $(Fe,Co)_2GeS_4$, the solubility of Co^{2+} cation increases as decreasing temperature and maximum temperature for synthesis is comparably low, otherwise the solubility limit in $(Co,Zn)_2GeS_4$ increases with temperature and it needs higher temperature to be synthesized. Especially, Figure 5.4b shows that there exists a nonlinear dependence of minimum temperature for synthesis of $(Co,Zn)_2GeS_4$ tetrahedral-type phase, which complies with extracted cell parameters shown in Figure 6.3e. As the content of cobalt increases furthermore beyond their solubility limits, both of unit cell parameters remain fairly unchanged from $x = 0.3$ and 0.5, respectively, and XRD intensities from the parents-type structure decrease, giving rise to a set of binary cobalt sulfides (Co_3S_4 and CoS) with GeS_2 depending on the molar ratio of cobalt as shown in Figure 5.4. The strongest binary phases were also confirmed at trials to directly synthesize Co_2GeS_4 from different temperatures. These binary compounds exactly match competing phases around the ternary formation region in the calculated phase diagram in Figure 5.2, leading to partly agree with theoretical results. This result is of importance as it clearly brings four of experimental evidences: (i) Co^{2+} cation has Oh site preference at high temperature, but Td site preference at low temperature, (ii) the small energy difference (only 0.03 eV/atom) between Co_2GeS_4 and the competing binary phase make us not easily accessible in experiment. In this respect, we could get a chance to meet new Co_2GeS_4 phase outside current synthesis conditions (extremely high and low temperature) experimentally, and other factors not included in this work, such as temperature dependence and entropy term, could give us a

chance to predict correct crystal structures theoretically. The relative weakness of such DFT methods is that they tend to overly delocalize electrons so that they are unable to properly describe the thermodynamics and the electronic properties of the compounds. To counterbalance the discrepancy between theory and experiment, A. Zunger, et al. brought an important correction to GGA models by explicitly considering coulombic correlation effects through FERE,[15] also applied in this work. As FERE has characteristics to be continuously updated through experimental results, this work will provide us the chance to properly find other missing materials through the feed-back of experimental results.

5.4 Conclusion

We have tried to find the missing Co_2GeS_4 compound through $(Fe,Co)_2GeS_4$ and $(Co,Zn)_2GeS_4$ solid solutions by a systematic investigation between theoretical prediction and experimental results. Overall, we bring new insights to the solid solution as well as the behavior of the binary phases as a function of the moral ratio of cobalt and temperature although the compound, Co_2GeS_4, chosen here for a case study of the validation of the theoretical calculation does not exist. Previously, it had only been reported a one-phase solid solution limit or two end-members corresponding to a complete miscibility in the similar solid solution system. Our findings raise several fundamental questions as to the origin of the driving force enabling the Co^{2+} cation to incorporate into the binary or ternary compounds, and furthermore to collaborate with theoretical prediction models used in this work. More generally, this coupled approach creates a practical framework for future design principle based search and discovery of effective materials.

References

[1] S. A. Kelkar, P. A. Shaikh, P. Pachfule, S. B. Ogale, *Energy Environ. Sci.* **2012**, *5*, 5681.

[2] M. Tsaroucha, Y. Aksu, E. Irran, M. Driess, **2011**, *23*, 2428.

[3] G. J. Synder, T. Caillat, J.-P. Fleurial, *Mater. Res. Innov.* **2001**, *5*, 67.

[4] K. Chang, B. Hallstedt, D. Music, *Chem. Mater.* **2012**, *24*, 97.

[5] L. Yu, S. Lany, R. Kykyneshi, V. Jieratum, R. Ravichandran, B. Pelatt, E. Altschul, H. a. S. Platt, J. F. Wager, D. a. Keszler, A. Zunger, *Adv. Energy Mater.* **2011**, *1*, 748.

[6] X. Zhang, A. Zunger, *Adv. Funct. Mater.* **2010**, *20*, 1944.

[7] F. H. Allen, G. Bergerhoff, I. Brown, **2013**.

[8] **n.d.**

[9] X. Zhang, V. Stevanovic, M. D'Avezac, S. Lany, *Phys. Rev. B* **2012**, *014109*, 014109.

[10] C. Delacourt, P. Poizot, J.-M. Tarascon, C. Masquelier, *Nat. Mater.* **2005**, *4*, 254.

[11] L. G. AKselrud, I. A. Ivashchenko, O. F. Zmiy, I. D. OLekseyuk, J. Stepien-Damm, *Chem. Met. Alloy.* **2009**, *2*, 108.

[12] H. Haeuseler, H. J. Stork, *Mater. Res. Bull.* **1992**, *27*, 925.

[13] H. Haeuseler, M. Wagener, J. Zhang, *Neues Jahrb. für Mineral. - Abhandlungen* **2006**, *182*, 285.

[14] W. Becker, H. D. Lutz, *Mater. Res. Bull.* **1978**, *13*, 907.

[15] V. Stevanović, S. Lany, X. Zhang, A. Zunger, *Phys. Rev. B* **2012**, *85*, 115104.

[16] J. Perdew, K. Burke, M. Ernzerhof, *Phys. Rev. Lett.* **1996**, *77*, 3865.

[17] G. Kresse, D. Joubert, *Phys. Rev. B* **1999**, *59*, 11.

[18] Rigakuo, **2010**.

[19] H. Vincent, E. F. Bertaut, W. H. Baur, R. D. Shannon, *Acta Crystallogr. Sect. B Struct. Crystallogr. Cryst. Chem.* **1976**, *32*, 1749.

[20] L. Vegard, *Zeitschrift für Phys.* **1921**, *5*, 17.

[21] M. Eagleson, *Concise Encyclopedia Chemistry*, Waler De Gruyter & Co., Berlin, **1983**.

[22] G. J. McIntyre, G. Moss, Z. Barnea, *Acta Crystallogr. Sect. A* **1980**, *36*, 482.

[23] R. Chevrel, M. Sergent, J. L. Meury, D. T. Quan, Y. Colin, *J. Solid State Chem.* **1974**, *10*, 260.

[24] V. G. Kuznetsov, M. A. Sokolova, K. K. Palkina, Z. V. Popova, *Inorg. Mater.* **1966**, *1*, 617.

[25] O. Knop, C.-H. Huang, K. I. G. Reid, J. S. Carlow, *J. Solid State Chem.* **1976**, *16*, 97.

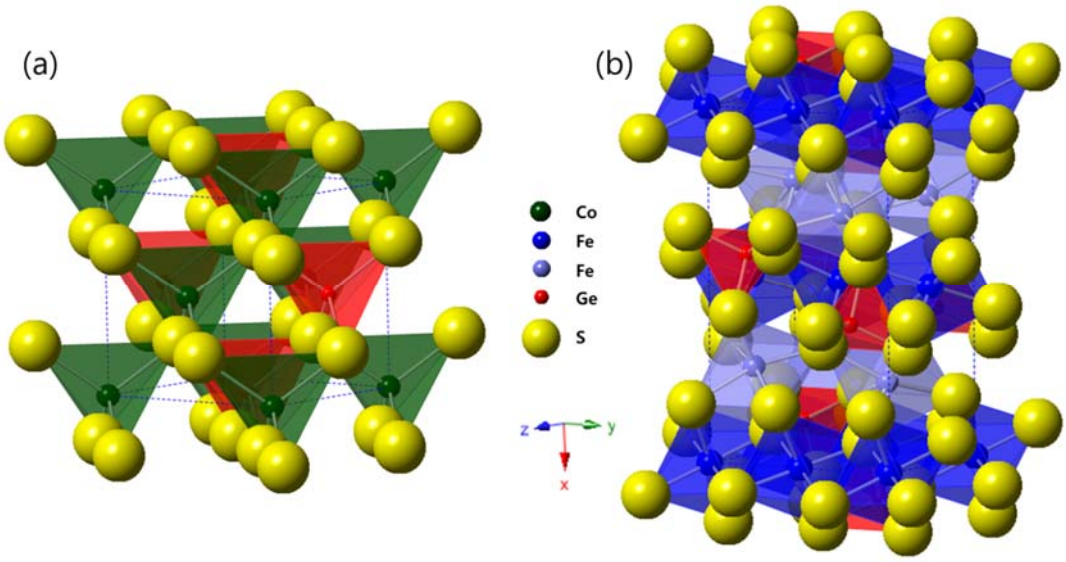

Figure 5.1 The crystal structure of (a) theoretically predicted Co_2GeS_4 (tetrahedral-type) and (b) Fe_2GeS_4 (olivine-type), slightly off (010).

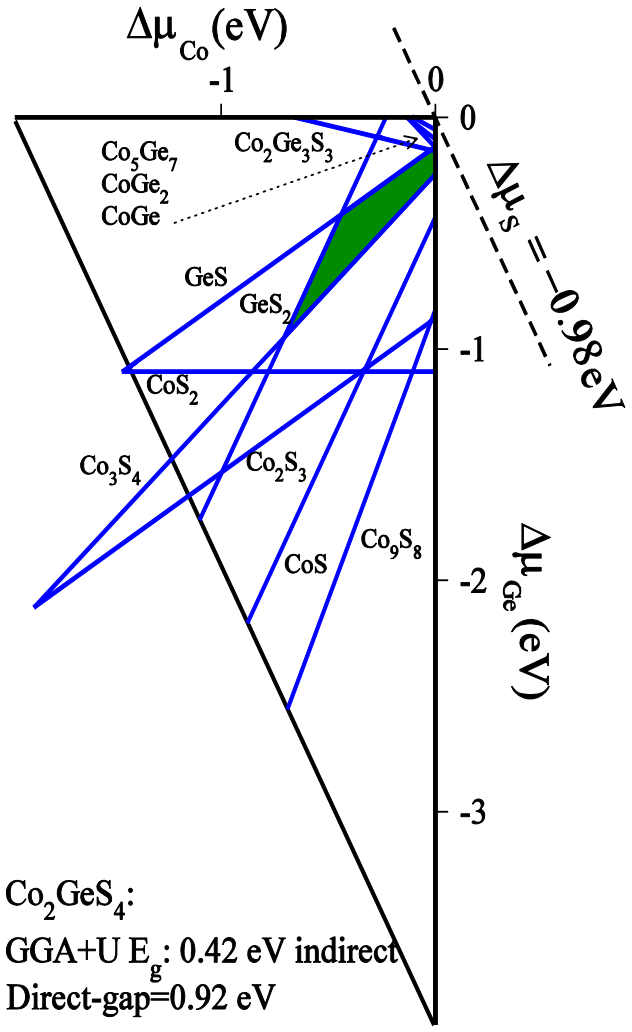

Figure 5.2 Projection of the allowed ranges of chemical potentials onto ($\Delta\boldsymbol{\mu_{Co}}, \Delta\boldsymbol{\mu_{Ge}}$) plane with the green polygon defined by Equation (5.1) representing the region of thermodynamic stability.

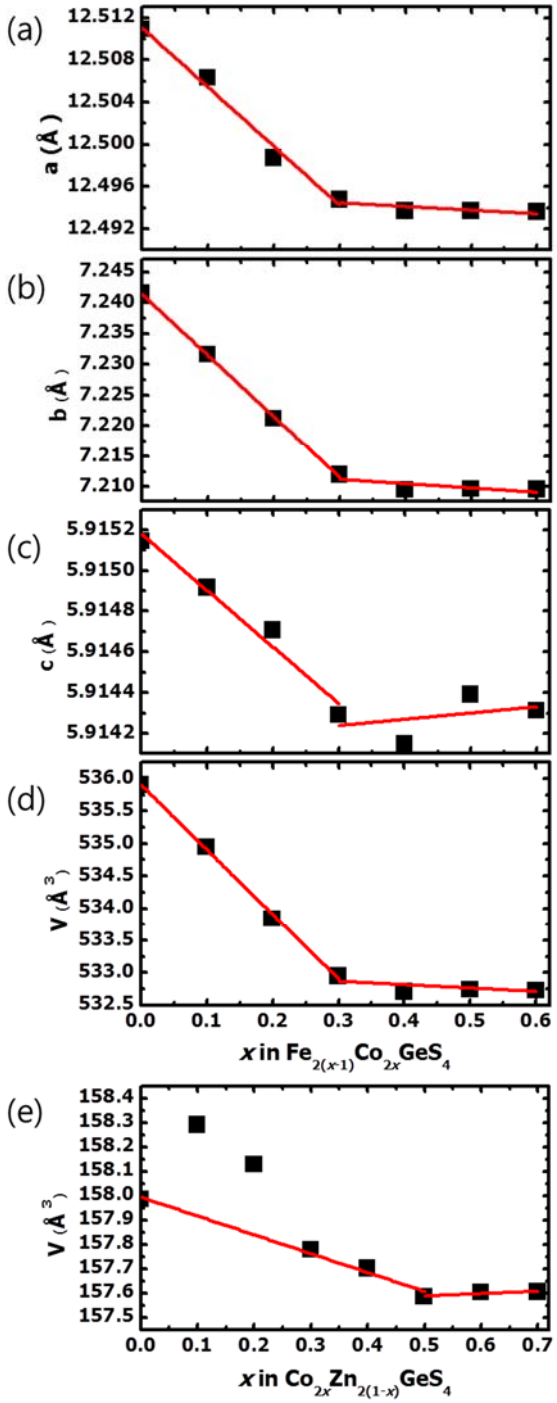

Figure 5.3 Unit cell parameters as a function x in (a) ~ (d) $Fe_{2(x-1)}Co_{2x}GeS_4$ and (e) $Zn_{2(x-1)}Co_{2x}GeS_4$. These values were refined in the *Pnma* and *F4-3m* space groups, respectively.

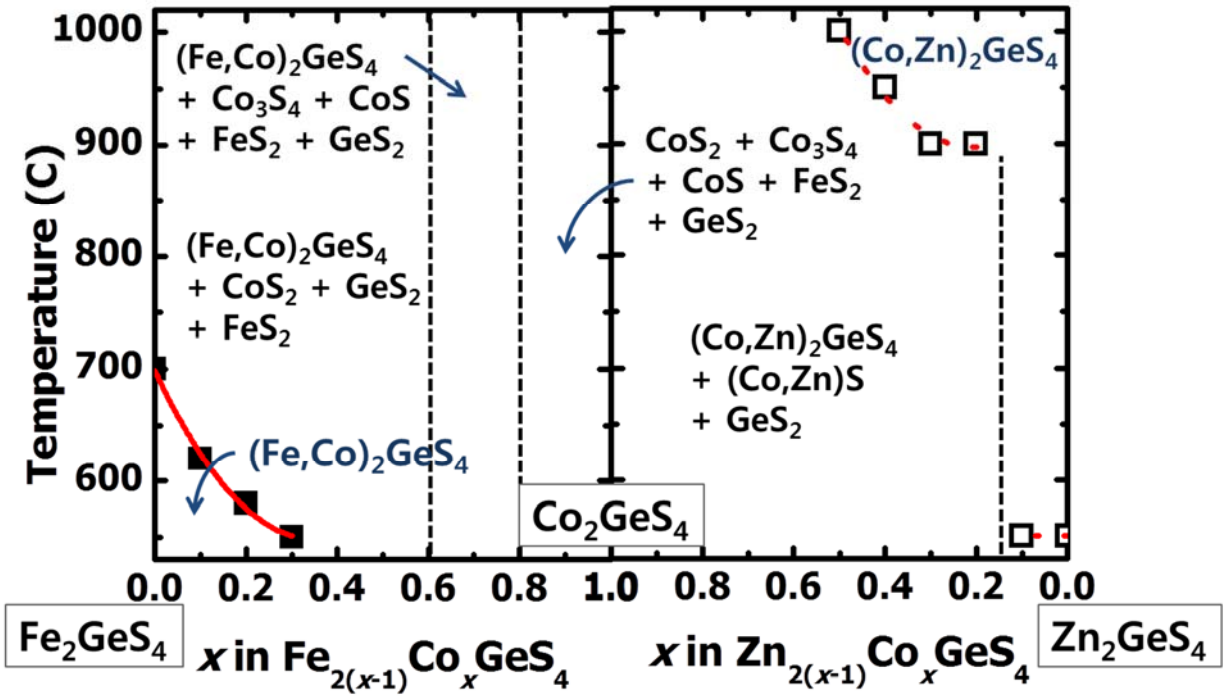

Figure 5.4 Phase distribution diagrams of a function x in (a) $Fe_{2(x-1)}Co_{2x}GeS_4$ and (b) $Zn_{2(x-1)}Co_{2x}GeS_4$ established from XRD data collected from 500 to 1050 ℃. Filled and open symbols are maximum and minimum temperature to be synthesized, respectively.

Supporting Information for

Search for Missing Compound Co_2GeS_4 through $(Fe,Co)_2GeS_4$ and $(Co,Zn)_2GeS_4$ Solid Solutions: A Theoretical and Experimental Approach

Jaeseok Heo[1], Xiuwen Zhang[2], Robert S. Kokenyesi[1], Alex Zunger[3], and Douglas A. Keszler[1]

[1]Department of Chemistry, Oregon State University, Corvallis, Oregon 97331-4003 USA

[2]Department of Physics, Colorado School of Mines, Golden, Colorado, 80401, USA

[3]University of Colorado, Boulder, Colorado 80309, USA

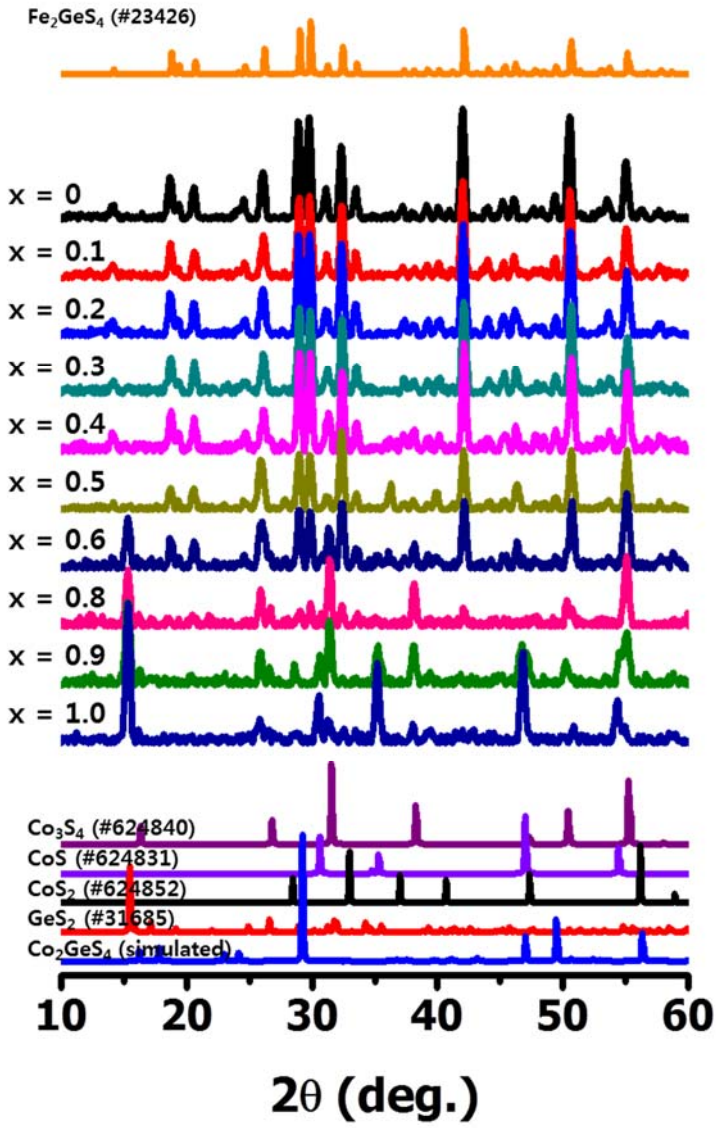

Figure S5.1 X-ray spectra of synthetic $Fe_{2(x-1)}Co_{2x}GeS_4$ solid solutions with $0 \leq x \leq 1$ at 550 ℃. X-ray diffraction (XRD) patterns were compared with inorganic crystal structure database (ICSD).

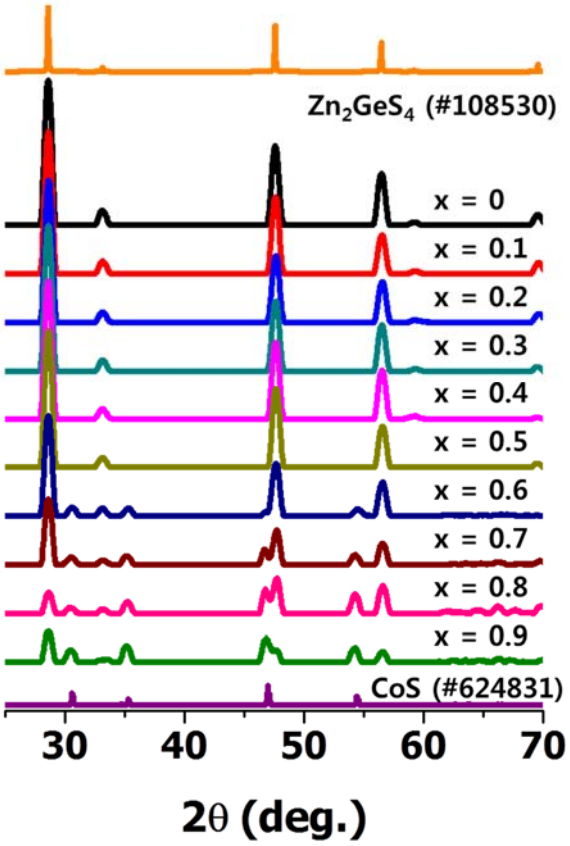

Figure S5.2 X-ray spectra of synthetic $Zn_{2(x-1)}Co_{2x}GeS_4$ solid solutions with $0 \leq x \leq 0.9$ at 1050 ℃. X-ray diffraction (XRD) patterns were compared with inorganic crystal structure database (ICSD).

Chapter 6

Conclusions

Two approaches, photovoltaic and thermoelectric, to meet the needs for renewable energy are discussed in this dissertation. To achieve this ambitious goal, the discovery of new promising materials requires a combination of keen chemical intuition, theoretical guidance, synthetic chemistry expertise, materials processing, and good measurement skills. The work presented in here was performed by this powerful combination to both offer materials design principles and identify promising candidates for photovoltaic and thermoelectric applications.

One of the most research semiconductor materials is the synthetic mineral tetrahedrite, typified by $Cu_{12}Sb_4S_{13}$. Optical, electrical, and thermal properties have been tuned via chemical substitutions, allowing optimization of performance toward the realizations of high-efficiency devices. For example, the strong onset of absorption near $E_G \sim 1.36$ eV in $Cu_{10}Zn_2Sb_4Se_{13}$ along with the absorption coefficient reaching a maximum value of 3×10^5 cm^{-1} at $E_G + 0.6$ eV, suggests that the thickness of the absorber layer can be reduced to < 500 nm without significant loss in performance. This inherent strong absorption property coupled with tunable band gaps and fabrication temperatures less than 300 ℃ makes the tetrahedrite family of materials especially attractive for photovoltaic absorbers. For thermoelectric applications, among tetrahedrite-derivatives, the Mn substituted sample ($Cu_{11}MnSb_4S_{13}$) exhibits the highest ZT, i.e., 1.13 at 575 K, which is primarily derived from an extremely low lattice thermal conductivity ($\kappa_L \leq 0.3$ Wm^{-1} K^{-1}). Additionally, this work demonstrates that this exceptional multi-functionality is related to the unique structural building blocks of these materials. Thus, exploring related materials may provide further opportunities to develop a new generation of PV and TE materials.

In the context of similar structural features, Cu_3-V-VI_4 (V = P, As, Sb; VI = S, Se) has also been discovered as absorber candidates. The band gaps of this family via mixed composition can be tuned between 0.6 and 2.4 eV with attendant hole mobilities up to 70 cm^2 V^{-1} s^{-1}. These prop-

erties coupled with relatively low synthesis temperature (T < 450 ℃) makes members of this family especially attractive as candidates for new polycrystalline thin-film solar cells in a tandem configuration.

Finally, it has been attempted to find the missing Co_2GeS_4 compound through $(Fe,Co)_2GeS_4$ and $(Co,Zn)_2GeS_4$ solid solutions by a systematic investigation between theoretical prediction and experimental results. More generally, this fundamental research creates a practical frame-work for future design principles based search and discovery of effective materials.

Bibliography

A. F. Mayadas, M. Shatzkes, *Phys. Rev. B* **1970**, *1*, 1382.

A. L. Fahrenbruch, R. H. Bube, *Fundamentals of Solar Cells: Photovoltaic Solar Energy Conversion*, Academic, UK, **1983**.

A. Luque, S. Hegedus, *Handbook of Photovoltaic Science and Engineering*, Wiley, Chichester, **2011**.

A. O. Musa, T. Akomolafe, M. J. Carter, *Sol. Energy Mater. Sol. Cells* **1998**, *51*, 305.

A. Pfitzner, M. Evain, V. Petricek, *Acta Crystallogr. B* **1997**, *53*, 337.

A. Pfitzner, S. Reiser, *Zeitschrift für Krist. - Cryst. Mater.* **2002**, *217*, 51.

A. Pfitzner, T. B. Bernert, *Zeitschrift für Krist. - Cryst. Mater.* **2004**, *219*, 20.

A. Shah, P. Torres, R. Rscharner, N. Wyrsch, H. Keppner, *Science* **1999**, *285*, 692.

A. Walsh, D. J. Payne, R. G. Egdell, G. W. Watson, *Chem. Soc. Rev.* **2011**, *40*, 4455.

A.-T. Petit, P.-L. Dulong, *Ann. Chim. Phys.* **1819**, *10*, 395.

B. McCandless, **MRS**, **2001**.

Bernhardt J. Wuensch, *Zeitschrift fur Krist.* **1964**, *119*, 437.

C. B. Vining, *Nat. Mater.* **2009**, *8*, 83.

C. Delacourt, P. Poizot, J.-M. Tarascon, C. Masquelier, *Nat. Mater.* **2005**, *4*, 254.

C. H. L. Goodman, *J. Phys. Chem. Solids* **1958**, *6*, 305.

C. S. Ferekides, D. L. Morel, *Process Development for High Voc CdTe Solar Cells*, NREL **2011**.

C. Wood, *Reports Prog. Phys.* **1988**, *51*, 459.

D. A. Cusano, *Solid State Electron.* **1963**, *6*, 217.

D. Abou-Ras, T. Kirchartz, U. Rau, *Advanced Characterization Techniques for Thin Film Solar Cells*, Wiley-VCH, Germany, **2011**.

D. Do, S. D. Mahanti, M.-S. Lee, Y. Zhang, C. Wolverton, *American Physics Society March Meeting*, **2012**, p. L17.009.

D. J. Griffiths, *Introduction to Quantum Mechanics*, Printice Hall, New Jersey, **1995**.

D. M. Rowe, *CRC Handbook of Thermoelectrics*, CRC Press, **1995**.

D. T. Do, S. D. Mahanti, *J. Phys. Chem. Solids* **2014**, *75*, 477.

D.-Y. Chung, T. Hogan, P. Brazis, M. Rocci-Lane, C. Kannewurf, M. Bastea, C. Uher, M. G. Kanatzidis, *Science* **2000**, *287*, 1024.

E. J. Skoug, D. T. Morelli, *Phys. Rev. Lett.* **2011**, *107*, 235901.

E. J. Skoug, J. D. Cain, D. T. Morelli, M. Kirkham, P. Majsztrik, E. Lara-Curzio, *J. Appl. Phys.* **2011**, *110*, 023501.

E. J. W. Verwey, P. Haayman, *Physica* **1941**, *8*, 979.

E. M. Mkawi, K. Ibrahim, M. K. M. Ali, A. S. Mohamed, *Int. J. Electronchemical Sci.* **2013**, *8*, 359.

E. Mackovicky, K. Forcher, W. Lottermoser, G. Amthauer, *Miner. Pet.* **1990**, *43*, 73.

F. H. Allen, G. Bergerhoff, I. Brown, *Crystallographic Databases*, **2013**.

F. J. Di Salvo, J. A. Wilson, J. V. Waszczak, *Phys. Rev. Lett.* **1976**, *36*, 885.

F. Machatschki, *Nor. Geol. Tidsskr.* **1928**, *10*, 23.

G. J. McIntyre, G. Moss, Z. Barnea, *Acta Crystallogr. A* **1980**, *36*, 482.

G. J. Snyder, E. S. Toberer, *Nat. Mater.* **2008**, *7*, 105.

G. J. Synder, T. Caillat, J.-P. Fleurial, *Mater. Res. Innov.* **2001**, *5*, 67.

G. Kresse, D. Joubert, *Phys. Rev. B* **1999**, *59*, 11.

G. Kresse, J. Furthmüller, *Phys. Rev. B* **1996**, *54*, 11169.

G. Mahan, B. Sales, J. Sharp, *Phys. Today* **1997**, *50*, 42.

G. S. Nolas, J. Poon, M. Kanatzidis, *MRS Bull.* **2006**, *31*, 199.

H. Haeuseler, H. J. Stork, *Mater. Res. Bull.* **1992**, *27*, 925.

H. Haeuseler, M. Wagener, J. Zhang, Neues Jahrb. für Mineral. - Abhandlungen 2006, 182, 285.

H. J. Goldsmid, *Introduction to Thermoelectricity*, Springer, **2010**.

H. Katagiri, *Thin Solid Films* **2005**, *480*, 426.

H. Vincent, E. F. Bertaut, W. H. Baur, R. D. Shannon, *Acta Crystallogr. B* **1976**, *32*, 1749.

H. W. Ma, G. C. Guo, G. W. Zhou, M. S. Wang, S. H. Lin, Z. C. Dong, J. S. Huang, *Chinese J. Struct. Chem.* **2002**, *21*, 288.

H. W. Mayer, I. Mikhail, K. Schubert, *J. Less Common Met.* **1978**, *59*, 43.

H. Yuen, *Conference of Opt. Sol. Energy*, Austin, **2011**.

I. M. Tsidil'kovskiĭ, *Sov. Phys. Uspekhi* **1992**, *35*, 85.

I. Repins, S. Glynn, J. Duenow, T. J. Coutts, W. Metzger, M. A. Contreras, *Proceeding of SPIE Conference*, San Diego, **2009**, p. 7409.

International Centre for Diffraction Data, *Powder Diffraction File*, **2013**.

International Energy Agency, "*Tracking Clean Energy Progress 2013*," http://www.iea.org./etp/tracking/, **2013**.

J. a. Spies, R. Schafer, J. F. Wager, P. Hersh, H. a. S. Platt, D. a. Keszler, G. Schneider, R. Kykyneshi, J. Tate, X. Liu, a. D. Compaan, W. N. Shafarman, *Sol. Energy Mater. Sol. Cells* **2009**, *93*, 1296.

J. Britt, C. Ferekides, *Appl. Phys. Lett.* **1993**, *62*, 2851.

J. Garin, E. Parthé, *Acta Crystallogr. B* **1972**, **28**, 3672.

J. Heo, G. Laurita, S. Muir, M. a. Subramanian, D. A. Keszler, *Chem. Mater.* **2014**, *26*, 2047.

J. Heo, R. Ravichandran, C. F. Reidy, J. Tate, J. F. Wager, D. A. Keszler, *Adv. Energy Mater. Submitted.*

J. P. Heremans, B. Wiendlocha, A. M. Chamoire, *Energy Environ. Sci.* **2012**, *5*, 5510.

J. P. Perdew, J. A. Chevary, S. H. Vosoko, K. A. Jackson, M. R. Pederson, D. J. Singh, F. Carlos, *Phys. Rev. B* **1992**, *46*, 6671.

J. Perdew, K. Burke, M. Ernzerhof, *Phys. Rev. Lett.* **1996**, *77*, 3865.

J. R. Sootsman, D. Y. Chung, M. G. Kanatzidis, *Angew. Chemie Int. Ed.* **2009**, *48*, 8616.

J. Zhao, A. Wang, M. A. Green, F. Ferrazza, *Appl. Phys. Lett.* **1998**, *73*, 1991.

K. Chang, B. Hallstedt, D. Music, *Chem. Mater.* **2012**, *24*, 97.

K. Suekuni, K. Tsuruta, M. Kunii, H. Nishiate, E. Nishibori, S. Maki, M. Ohta, A. Yamamoto, M. Koyano, *J. Appl. Phys.* **2013**, *113*, 043712.

K. Suekuni, K. Tsuruta, T. Ariga, M. Koyano, *Appl. Phys. Express* **2012**, *5*, 051201.

L. G. AKselrud, I. A. Ivashchenko, O. F. Zmiy, I. D. OLekseyuk, J. Stepien-Damm, *Chem. Met. Alloy.* **2009**, *2*, 108.

L. Vegard, *Zeitschrift für Phys.* **1921**, *5*, 17.

L. Yu, A. Zunger, *Phys. Rev. Lett.* **2012**, *108*, 068701.

L. Yu, R. S. Kokenyesi, D. a. Keszler, A. Zunger, *Adv. Energy Mater.* **2013**, *3*, 43.

L. Yu, S. Lany, R. Kykyneshi, V. Jieratum, R. Ravichandran, B. Pelatt, E. Altschul, H. a. S. Platt, J. F. Wager, D. a. Keszler, A. Zunger, *Adv. Energy Mater.* **2011**, *1*, 748.

M. A. Green, K. Emery, Y. Hishikawa, W. Warta, E. D. Dunlop, *Prog. Photovoltaics Res. Appl.* **2012**, *20*, 12.

M. Burgelman, P. Nollet, S. Degrave, *Thin Solid Films* **2000**, *361*, 527.

M. Burgelman, *Thin Film Solar Cells*, Wiley-VCH, Weinheim, **2006**.

M. Cutler, J. F. Leavy, R. L. Fitzpatrick, *Phys. Rev.* **1964**, *133*, A1143.

M. Eagleson, *Concise Encyclopedia Chemistry*, Waler De Gruyter & Co., Berlin, **1983**.

M. F. Razmara, C. M. B. Henderson, R. A. D. Pattrick, J. M. Charnock, *Mineral. Mag.* **1997**, *61*, 79.

M. Fox, *Optical Properties of Solids*, Oxford University Press, New York, **2010**.

M. L. Cohen, T. K. Bergstresser, *Phys. Rev.* **1966**, *141*, 789.

M. Pósfai, P. R. Buseck, *Am. Mineral.* **1998**, *83*, 373.

M. Telkes, *Am. Mineral.* **1950**, *35*, 536.

M. Tsaroucha, Y. Aksu, E. Irran, M. Driess, *Chem. Mater.* **2011**, *23*, 2428.

N. E. Johnson, J. R. Craig, J. D. Rimstidt, *Am. Mineral.* **1988**, *73*, 389.

N. Mott, M. Pepper, S. Pollitt, R. H. Wallis, C. J. Adkins, *Proc. R. Soc. A* **1975**, *345*, 169.

N. P. Blake, S. Latturner, J. D. Bryan, G. D. Stucky, H. Metiu, *J. Chem. Phys.* **2001**, *115*, 8060.

N. W. Ashcroft, N. D. Mermin, *Solid State Physics*, Belmont, **1976**.

NREL, *Research Cell Efficiency Records*, **2013**.

O. Delaire, J. Ma, K. Marty, a F. May, M. a McGuire, M.-H. Du, D. J. Singh, a Podlesnyak, G. Ehlers, M. D. Lumsden, B. C. Sales, *Nat. Mater.* **2011**, *10*, 614.

O. Knop, C.-H. Huang, K. I. G. Reid, J. S. Carlow, *J. Solid State Chem.* **1976**, *16*, 97.

O. Madelung, U. Rössler, *Landolt-Börnstein - Gr. III Condens. Matter* **2000**, *41*, 1.

P. Blaha, K. Schwarz, G. K. H. Madsen, D. Kvasnicka, J. Luitz, *Wien2K*, **2001**.

P. E. Blöchl, *Phys. Rev. B* **1994**, *50*, 17953.

P. F. P. Poudeu, J. D. Angelo, H. Kong, A. Downey, J. L. Short, R. Pcionek, T. P. Hogan, C. Uher, M. G. Kanatzidis, *J. Am. Chem. Soc.* **2006**, *9*, 14347.

P. Jackson, D. Hariskos, E. Lotter, S. Paetel, R. Wuerz, R. Menner, W. Wiltraud, M. Powalla, *Prog. Photovoltaics Res. Appl.* **2011**, *19*, 894.

P. W. Anderson, *Phys. Rev.* **1958**, *109*, 1492.

R. A. D. Pattrick, *Mineral. Mag.* **1983**, *47*, 441.

R. Chevrel, M. Sergent, J. L. Meury, D. T. Quan, Y. Colin, J. Solid State Chem. 1974, 10, 260.

R. N. Hall, *Phys. Rev.* **1952**, *87*, 387.

R. R. Heikes, R. W. Ure, *Thermoelectricity: Science and Engineering, Interscience*, New York, **1961**.

R. Scheer, H.-W. Schock, *Chalcogenide Photovoltaics: Physics, Technologies, and Thin Film Devices*, Wiley-VCH, Wienheim, **2011**.

R. Venkatasubramanian, E. Siivola, T. Colpitts, B. O'Quinn, *Nature* **2001**, *413*, 597.

Rigakuo, 2010.

S. A. Kelkar, P. A. Shaikh, P. Pachfule, S. B. Ogale, Energy Environ. Sci. 2012, 5, 5681.

S. B. Zhang, S. Wei, A. Zunger, *Phys. Rev. B* **1998**, *57*, 9642.

S. M. Sze, K. K. Ng, *Physics of Semiconductor Devices*, Wiley, Chichester, **2007**.

S.-H. Wei, S. B. Zhang, *Phys. Rev. B* **2000**, *62*, 6944.

Solar Energy Industries Association, "*Solar Market Insight Report 2013 Q2*," http://www.seia.org/research-resources/solar-market-insight-report-2013-q2/, **2013**.

T. M. Tritt, M. A. Subramanian, *MRS Bull.* **2006**, *31*, 188.

T. M. Tritt, *Recent Trends in Thermoelectric Materials Research*, Academic, **2001**.

T. Tiedje, E. Yablonovitch, G. D. Cody, B. G. Brooks, *IEEE Trans. Electron Devices* **1984**, *31*, 711.

U. Rau, J. H. Werner, *Appl. Phys. Lett.* **2004**, *84*, 3735.

V. G. Kuznetsov, M. A. Sokolova, K. K. Palkina, Z. V. Popova, *Inorg. Mater.* **1966**, *1*, 617.

V. Itthibenchapong, R. S. Kokenyesi, A. J. Ritenour, L. N. Zakharov, S. W. Boettcher, J. F. Wager, D. A. Keszler, *J. Mater. Chem. C* **2013**, *1*, 657.

V. Kuznetsov, D. Rowe, *J. Alloys Compd.* **2004**, *372*, 103.

V. Stevanović, S. Lany, X. Zhang, A. Zunger, *Phys. Rev. B* **2012**, *85*, 115104.

W. Becker, H. D. Lutz, *Mater. Res. Bull.* **1978**, *13*, 907.

W. Shockley, H. J. Queisser, *J. Appl. Phys.* **1961**, *32*, 510.

W. Shockley, W. T. J. Read, *Phys. Rev.* **1952**, *87*, 835.

X. Lu, D. T. Morelli, Y. Xia, F. Zhou, V. Ozolins, H. Chi, X. Zhou, C. Uher, *Adv. Energy Mater.* **2013**, *3*, 342.

X. Shi, J. Yang, J. R. Salvador, M. Chi, J. Y. Cho, H. Wang, S. Bai, J. Yang, W. Zhang, L. Chen, *J. Am. Chem. Soc.* **2011**, *133*, 7837.

X. Wu, *Sol. Energy* **2004**, *77*, 803.

X. Zhang, A. Zunger, *Adv. Funct. Mater.* **2010**, *20*, 1944.

X. Zhang, V. Stevanovic, M. D'Avezac, S. Lany, *Phys. Rev. B* **2012**, *86*, 014109.

Y. Kanazawa, *Bull. Geol. Surv. Japan* **1984**, *35*, 13.

Y. Pei, H. Wang, G. J. Snyder, *Adv. Mater.* **2012**, *24*, 6125.

Y. Zhang, E. Skoug, J. Cain, V. Ozoliņš, D. Morelli, C. Wolverton, *Phys. Rev. B* **2012**, *85*,